CHARACTERIZATION OF NON-NEWTONIAN FLUIDS and FLUID FLOW THROUGH BIOFILMS IN POROUS MEDIA USING NUCLEAR MAGNETIC RESONANCE

by

Alexis Sanderlin Edden

A thesis submitted in partial fulfillment
of the requirements for the degree

of

Master of Science

in

Chemical Engineering

MONTANA STATE UNIVERSITY
Bozeman, Montana

July 2013

©COPYRIGHT

by

Alexis Sanderlin Edden

2013

All Rights Reserved

APPROVAL

of a thesis submitted by

Alexis Sanderlin Edden

This thesis has been read by each member of the thesis committee and has been found to be satisfactory regarding content, English usage, format, citation, bibliographic style, and consistency and is ready for submission to The Graduate School.

Dr. Jennifer Brown

Approved for the Department of Chemical and Biological Engineering

Dr. Jeffrey Heys

Approved for The Graduate School

Dr. Ronald W. Larsen

STATEMENT OF PERMISSION TO USE

In presenting this thesis in partial fulfillment of the requirements for a master's degree at Montana State University, I agree that the Library shall make it available to borrowers under rules of the Library.

If I have indicated my intention to copyright this thesis by including a copyright notice page, copying is allowable only for scholarly purposes, consistent with "fair use" as prescribed in the U.S. Copyright Law. Requests for permission for extended quotation from or reproduction of this thesis in whole or in parts may be granted only by the copyright holder.

Alexis Sanderlin Edden

July 2013

DEDICATION

This thesis is dedicated to my family for your never-ending love, support and understanding as I made it through graduate school. Though you are no longer physically with me, Mom, I know you would be very proud of my accomplishment. I love and miss you terribly. Dad, you are the math mind and the source of my love for engineering. Thank you for your encouragement, the "math genes", and your love. Shan and Tim (and Ford!), you have been incredible support and so much fun. I know I can count on you for advice in any situation. I love you all very much. William and Bridger, my stepchildren (or stair children, as Bridger once said), I appreciate your accepting my absence as I finished my research and thesis. I am blessed to have two wonderful young men like you in my life. Nana and Papa, you accepted me into the family as if I was your own daughter and always believed in me. I love you both very much! And most importantly, my husband, Bill. You have been an unfaltering source of encouragement and love, no matter what I was working on. In times of what I considered a crisis, you were able to focus my attention on the things that mattered, reminding me that sometimes missteps are okay. You have been so patient in my absence, running the house and taking care of just about everything. It's almost over, Honey, and we should take a vacation! You definitely deserve it. I love you forever.

ACKNOWLEDGEMENTS

I would like to thank my committee members, Drs. Jennifer Brown, Sarah Codd and Abigail Richards, for their enduring patience as I navigated the thesis writing and defense process. I would especially like to thank the directors of the MSU NMR lab, Drs. Brown and Codd and Dr. Joe Seymour, for giving me this opportunity and convincing me to finish my Master's degree. Dr. Brown, as the chair of my committee, you were instrumental in guiding me through the difficult questions I had regarding NMR, as well as leading me to the final day of defending my thesis. Thank you.

I would also like to thank the many friends who have supported and encouraged me to keep plugging away at this endeavor. Victor Armendariz, you've been my rock for decades and I don't know where I would be without you. Lisa Weeks, you've been a wonderful friend and I'm so grateful we met. Your friendship is a treasure that I hope will continue long after we graduate. Elmira Nybo, we started working in the NMR lab at approximately the same time and learning NMR together was great fun. However, I owe you so much more than that. You introduced me to my amazing husband, and for that I am forever indebted to you! Emarit Ranu, without your friendship, I doubt I would have been at MSU. Thank you for your encouragement, wisdom and especially the sanctuary you provided. Dr. Greg Baldwin, thank you for your unwavering support, the fun times we shared and the many humorous phone calls. You remind me every time just how precious life really is. To the many more friends not mentioned by name that deserve my gratitude and I extend you all a giant thank you!

TABLE OF CONTENTS

1. INTRODUCTION TO NUCLEAR MAGNETIC RESONANCE MICROSCOPY 1

NMR Basics 1
Excitation and Relaxation 4
Excitation 5
Relaxation 7
Signal Detection and Processing 11
Gradients 16
Gradient Applications 17
Pulse Sequences 20
Spin Echo Pulse Sequence 21
Stimulated Echo Pulse Sequence 22
Imaging Pulse Sequence 23
CPMG Pulse Sequence 27
Translational Motion 28
Translational Motion Gradients 28
Diffusion 30
Propagators 32
Velocity 34
Multi-Dimensional Experiments 35
Propagator-T_2 35
Velocity Imaging 37

2. INTRODUCTION TO POLYMERS 40

Basics of Polymers 40
Polyacrylamide 42
Alginate 45
Biofilms 47

3. PERMEABILITY OF A GROWING BIOFILM IN A POROUS MEDIA FLUID FLOW ANALYZED BY MAGNETIC RESONANCE DISPLACEMENT-RELAXATION CORRELATIONS 52

Contributions of Authors and Co-Authors 52
Manuscript Information 53
Abstract 54
Introduction 55
Magnetic Resonance 56
Measurement of Molecular Motion Using MR 57
Measurement of Relaxation Using MR 58

TABLE OF CONTENTS - CONTINUED

Materials and Methods 59
Biofilm Growth 59
Displacement-Relaxation Correlation Experiments 61
Results and Discussion 63
Conclusion 69

4. BIOFILM DETECTION IN NATURAL UNCOLSOLIDATED POROUS MEDIA USING A LOW-FIELD MAGNETIC RESONANCE SYSTEM 70

Contributions of Authors and Co-Authors 70
Manuscript Information 71
Abstract 72
Introduction 73
Theory 76
T_2 Relaxation 76
Low-Field Magnetic Resonance 78
Materials and Methods 79
Reactor Design 79
Sand Analysis 81
Alginate Preparation 82
NMR Measurements 83
Results and Conclusions 84
Silica Sand with Biofilm 84
Hanford Sand with Biofilm 86
Alginate Gels and Sand with Alginate Solutions 86

5. RHEO-NMR AND NON-NEWTONIAN FLUIDS 91

Introduction 91
Rheology 91
Rheo-NMR 93
Methods and Materials 95
Rheology 95
Rheo-NMR 95
Rheo-NMR Couette Device 96
Sample Preparation 98
Velocity Imaging 100
Results and Discussion 100
Future Work 106

REFERENCES 112

LIST OF FIGURES

Figure Page

1.1 Illustration of proton precession 2

1.2 Zeeman energy diagram 3

1.3 Illustration of radio frequency pulses 7

1.4 Illustration of T_1 relaxation 8

1.5 Illustration of T_2^* relaxation 10

1.6 Equipment set up 12

1.7 Free Induction Decay (FID) 13

1.8 Fourier transform of NMR signal 15

1.9 Illustration of a linearly varying gradient 17

1.10 Illustration of the application of a long gradient duration 19

1.11 Gradient echo pulse sequence 20

1.12 Spin echo pulse sequence 21

1.13 Stimulated echo pulse sequence 23

1.14 Imaging pulse sequence 26

1.15 CPMG pulse sequence 27

1.16 Gaussian distribution 29

1.17 PGSE and PGStE pulse sequences 30

1.18 Propagator-T_2 [$P(Z, \Delta)$-T_2] pulse sequence 36

1.19 Example of $P(Z, \Delta)$-T_2 data 37

1.20 Velocity imaging pulse sequence 38

LIST OF FIGURES – CONTINUED

Figure		Page
2.1	Acrylamide monomer unit	42
2.2	Alginate monomer units	46
2.3	Illustration of biofilm architecture	49
3.1	$P(Z, \Delta)$-T_2 pulse sequence	62
3.2	$P(Z, \Delta)$-T_2 data as a function of observation time	64
3.3	Biofilm peak intensity as a function of observation time	65
3.4	$P(Z, \Delta)$ and T_2 profiles as a function of biofilm growth	66
3.5	T_2 distributions as a function of growth media concentration	68
4.1	Silica sand column reactors	80
4.2	Biofouled and non-biofouled sand samples	81
4.3	T_2 distribution of silica sand at low field	85
4.4	T_2 distribution of silica sand at high field	85
4.5	T_2 distribution of mixed Hanford sand at low field	86
4.6	T_2 distribution of alginate at low field	87
4.7	T_2 distribution of alginate in silica sand at low field	88
4.8	T_2 distribution of alginate in mixed Hanford sand at low field	89
5.1	Illustration of stress-strain relationship for power-law fluids	93
5.2	Rheo-NMR Couette system	96
5.3	Cross section of Couette device	97

LIST OF FIGURES – CONTINUED

Figure Page

5.4 Velocity imaging pulse sequence 99

5.5 Example of a velocity image and velocity profile 101

5.6 Rheology data for 1 wt% polyacrylamide [PAA] 102

5.7 Normalized velocity profile at 26.7 s^{-1}, glycerol and PAA 103

5.8 Normalized velocity profile at 53.4 s^{-1}, glycerol and PAA 104

5.9 Normalized velocity profiles of PAA at 26.7 s^{-1}, 53.4 s^{-1}, and 160 s^{-1} 105

5.10 Illustration of polymer-particle interactions 107

5.11 Rheology data for PAA and PAA with 1 wt% SiO_2 nanoparticles 108

ABSTRACT

The research presented in this thesis uses nuclear magnetic resonance (NMR) experiments to study biofilm growth in porous media and to characterize the effects of shear forces on a non-Newtonian fluid. An introduction to NMR is given to provide experimental background and an understanding of the data analysis, followed by an overview of polymers and biofilms. The next chapters describe the experiments and results for biofilm growth in two different model porous media. The final chapter provides analysis of shear forces on the non-Newtonian fluid polyacrylamide.

Biofilms are formed when bacterial cells attach to a surface and begin to grow in a phenotypically altered state. Observation of biofilm growth in porous media poses significant challenges due to the heterogeneous nature of the biofilm and the opaque nature of the surfaces on which biofilms form. In the experiments presented, displacement-relaxation experiments were performed while a biofilm grew in a model porous media positioned in the magnet. Separate analysis of the flow characteristics of the biofilm phase and the bulk fluid phase was possible within the same data set. The results indicate that convective flow did not occur through the biofilm and that biofouling of the pore space resulted in faster bulk fluid flow through the channels.

Natural geological matter contains magnetically susceptible materials such as iron-bearing minerals and cannot be analyzed with a high-field NMR system. A benchtop low-field NMR system was used to perform relaxation measurements on highly magnetic natural geological sand samples mixed with sand and biofilm from a sand column reactor. Shorter relaxation times in the biofouled sample indicated the presence of a biofilm, demonstrating that low-field NMR systems can be used in the natural environment to test for the presence of biofouling.

Polyacrylamide is often used in high-shear applications such as enhanced oil recovery and wastewater treatment. These shear forces could affect the structure, and thus the function, of the polymer. Rheo-NMR, a combination of rheology and NMR, was used to study the velocity field for polyacrylamide solutions in a Rheo-NMR Couette device under different shear rates. The data shows that the polymer exhibits shear thinning behavior.

CHAPTER ONE

INTRODUCTION TO NUCLEAR MAGNETIC RESONANCE MICROSCOPY

NMR Basics

Magnetic resonance imaging, or MRI, has gained widespread use in hospitals around the world within the last thirty years as a non-invasive, non-destructive way to image tissues and systems within the body. MRI machines and equipment are built on discoveries and advances in nuclear magnetic resonance (NMR), a topic that physicists and chemists began investigating in the early 1940s [1].

NMR is possible due to an intrinsic property of an elemental nucleus called angular momentum, or spin. The number of protons and neutrons in the nucleus determines the atom's spin number, denoted by I and often referred to as the angular momentum quantum number. If the spins are paired, as they are in atoms that have an even number of both neutrons and protons, then the nucleus has a net spin number of zero and cannot be detected using NMR techniques. If the atom has an odd number of neutrons and an odd number of protons, the spin number is a whole number, such as 1, 2, or 3. Finally, if the sum of the number of protons and neutrons is odd, the spin number is a half integer, such as ½, $^3/_2$, or $^5/_2$. Atoms with whole- and half-integer spin numbers can be detected with NMR. In the research that follows, only the ^{1}H atom with $I = ½$ will be

studied. Spin is a quantized quantity with magnitude S given by

$$S = \hbar[I(I+1)]^{1/2} \qquad 1.1$$

where $\hbar$ is the Planck's constant divided by 2π [1].

In addition to spin angular momentum, nuclei have an associated magnetic dipole moment, μ. The angular momentum is proportional to the magnetic dipole moment with the constant of proportionality called the gyromagnetic ratio γ [2].

$$\mu = \gamma S \qquad 1.2$$

The gyromagnetic ratio is nuclei specific and has a value of 2.675×10^8 rad T^{-1} s^{-1} for the ^1H proton, where Tesla (T) is a measure of the magnetic field strength [2]. For some substances, such as magnets, the magnetic moment is permanent [1]. In other substances, the magnetic moment must be induced by the application of an external magnetic field.

The spin angular momentum of a nucleus is traditionally represented as a vector with both a magnitude and a direction. In the absence of an applied magnetic field, the spins of a given sample will orient in all directions, as seen in Figure 1.1a. However, in the presence of an applied magnetic field B_0, these spins will align either parallel or

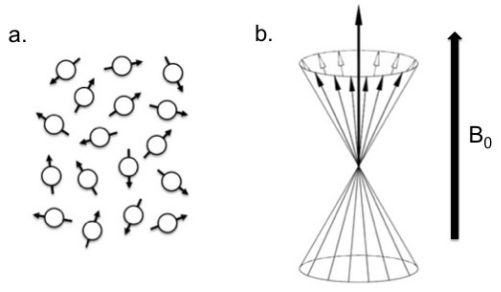

Figure 1.1. Protons in free rotation and within a magnetic field. a.) Random orientation of nuclei in the absence of a magnetic field. b.) Precession of the nuclei around the applied magnetic field B_0. The vector sum of the precessing spins results in a magnitude aligned with the magnetic field.

antiparallel with the field. Due to the presence of the magnetic dipole moment, the ^{1}H nucleus also precesses around B_0 as shown in Figure 1.1b. The vector sum of the precessing nuclei is oriented along B_0.

In addition to the effect of precession, the applied magnetic field B_0 induces differing energy states in the nuclei. The number of probable energy states is given by $(2I + 1)$ and is often referred to as the azimuthal quantum number [1]. These energy levels are denoted as m and can have values ranging from $-I$ to I. For the ^{1}H nucleus with spin-½, there are only two possible states of $m = -½$ or $m = ½$. This split in energy is known as the Zeeman Effect and is depicted in Figure 1.2. The energy associated with these two states "depends on the interaction between the magnetic moment and the magnetic field B_0" [1].

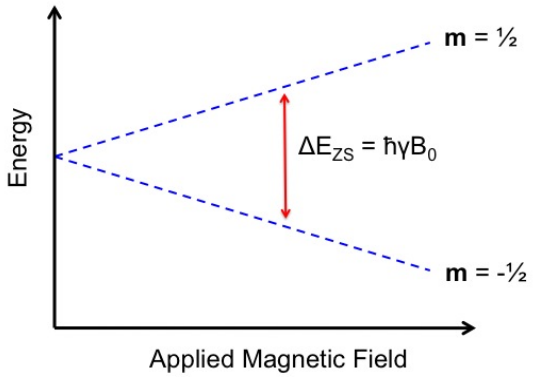

Figure 1.2. Zeeman energy diagram. Increase in the energy difference, known as the Zeeman effect, of the two spin states of the ^{1}H nucleus induced by an applied magnetic field.

In a magnetic field B_0, the magnetic dipole is in the lowest energy state when the nucleus is aligned parallel to B_0. The number of spins in this energy level is generally represented as N_α, while spins that align anti-parallel in the higher energy state are

represented as N_β. There is a slightly greater population of spins in the lower energy state, thus $N_\alpha - N_\beta > 0$. This slight excess of spins gives rise to a bulk magnetization M_0 in the direction of B_0. At thermal equilibrium, the ratio of the populations in these two energy states is given by the Boltzmann factor

$$N = \frac{N_\beta}{N_\alpha} = \exp\left(-\frac{\hbar\gamma B_0}{Tk_B}\right) \qquad 1.3$$

where T is the absolute temperature and k_B is Boltzmann's constant [1].

The energy difference between these two possible energy states of a spin-½ nucleus due to Zeeman interactions as shown in Figure 1.2 is given by

$$E_{ZS} = \hbar\gamma B_0 \qquad 1.4$$

For the protons to jump from one energy level to the other, electromagnetic radiation in the form of a photon must be absorbed or emitted. The energy of a photon is given by [3]

$$E_P = \hbar\omega_0 \qquad 1.5$$

When these two energies are equated, the equation simplifies to

$$\omega_0 = \gamma B_0 \qquad 1.6$$

where ω_0 is called the Larmor frequency. Equations (1.4) through (1.6) illustrate that for a given magnetic field B_0 only one frequency exists that can excite the nuclei and cause a transition between the two energy levels, $m = ½$ and $m = -½$. It is this frequency with which the nuclei precess about their rotational axis. For the ^1H nuclei with $\gamma = 2.675 \times 10^8$ rad s^{-1} T^{-1} in a 7 Tesla (T) magnetic field, the frequency required for the change in energy levels is 300 MHz.

Excitation and Relaxation

Excitation of the spins and subsequent relaxation form the basis for magnetic resonance phenomena. These processes are described here.

Excitation

As mentioned above, there is a slight excess of spins aligned parallel with the magnetic field B_0. Although the total percentage of spins is very small, they still form a bulk magnetization M in the direction of the magnetic field. In order for the nuclei to be detected, they must be excited from thermal equilibrium into the transverse plane, rather than aligned with the magnetic field. Recall that it is only possible for the nuclei to change energy states, or become excited, when the energy is applied at the resonant frequency, ω_0, of the nuclei. This energy is imparted to the system in the form of an on-resonance radio frequency (RF) pulse, as precession of 300 MHz is in the radio frequency range. These pulses are applied perpendicular to B_0 and create a new magnetic field B_1. A torque results between M and B_1 given by [2]

$$\frac{d\mathbf{M}}{dt} = \gamma \mathbf{M} \times \mathbf{B}_1 \qquad 1.7$$

which rotates the magnetization M. The extent of the rotation is determined by the strength and duration of the RF pulse and will be discussed later.

The oscillating magnetic field induced by the RF pulse (B_1) is given by

$$\mathbf{B}_1(t) = B_1 \cos(\omega_0 t)\mathbf{i} - B_1 \sin(\omega_0 t)\mathbf{j} \qquad 1.8$$

where **i** and **j** are the unit vectors along the transverse axes x and y, respectively.

Recalling that $\mathbf{B_0} = B_0\mathbf{k}$, then equation 1.7 becomes

$$\begin{aligned}\frac{dM_x}{dt} &= \gamma[M_y B_0 + M_z B_1 \sin(\omega_0 t)] \\ \frac{dM_y}{dt} &= \gamma[M_z B_1 \cos(\omega_0 t) - M_x B_0] \\ \frac{dM_z}{dt} &= \gamma[-M_x B_1 \sin(\omega_0 t) - M_y B_1 \cos(\omega_0 t)]\end{aligned} \qquad 1.9$$

for each direction in the Cartesian coordinate system, which will now be referred to as the laboratory reference frame [2]. To simplify the mathematics, a shift to the rotating frame is typically employed. Though slightly elementary, the example of a merry-go-round will be used to illustrate this change. To an observer on the playground, the merry-go-round is seen as rotating with some angular velocity. However, if the observer is on the merry-go-round, the apparatus does not appear to be rotating.

For NMR, the rotating reference frame rotates at the Larmor frequency ω_0. In the rotating frame when the initial condition is given by $\mathbf{M}(t) = M_0\mathbf{k}$, the solution to equation 1.9 is

$$\begin{aligned}M_x &= M_0 \sin(\omega_1 t)\sin(\omega_0 t) \\ M_y &= M_0 \sin(\omega_1 t)\cos(\omega_0 t) \\ M_z &= M_0 \cos(\omega_1 t)\end{aligned} \qquad 1.10$$

where $\omega_1 = \gamma B_1$ [2]. These equations imply that with the application of an on-resonance magnetic field, the net magnetization M "simultaneously precesses about the longitudinal field B_0 at ω_0 and about the RF field B_1 at ω_1" [2]. In the rotating frame, B_1 is stationary and only the precession around it is visible.

For the instruments used in the experiments outlined in this thesis, the magnetic field B_0 is oriented in the z direction of the Cartesian coordinate system. When the RF

pulse causes the net magnetization *M* to rotate 90 angular degrees into the x-y (transverse) plane, it is termed a 90° pulse, or a $\frac{\pi}{2}$ pulse. Similarly, an RF pulse that causes a rotation of 180 angular degrees is called a 180° pulse, or π pulse. The pulses are also given a direction or axis around which the pulse is applied. For example, a 90° pulse around the positive x-axis would be given as 90_x. Figure 1.3 illustrates several different pulses. The angle through which the spins rotate is determined by the power and duration of the RF pulse, both of which are programmable with the software used in the experiments conducted for the research described in this thesis.

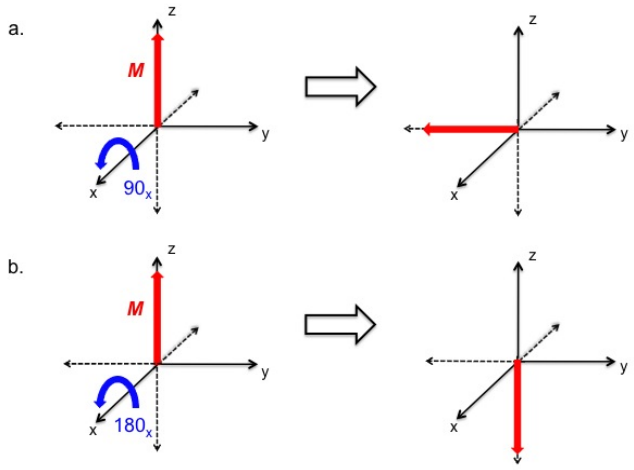

Figure 1.3. Illustration of the effect two different commonly applied radio frequency pulses on the net magnetization, *M*. a.) A 90_x pulse rotates the magnetization into the transverse plane, while (b.) a 180_x pulse rotates the magnetiztion along the –z axis.

Relaxation

When the energy input to the sample ceases, that is to say that the RF pulse switches off, the spins will return to thermal equilibrium by means of two forms of relaxation: longitudinal, or spin-lattice relaxation, and transverse, or spin-spin relaxation.

As the name implies, longitudinal relaxation is the process whereby M reappears in the longitudinal direction of the magnetic field B_0. This type of relaxation is due to the thermal interactions of the sample with its environment, known as the "lattice" [1]. The time it takes for this relaxation to occur is called the T_1, or spin-lattice, relaxation time. The evolution of the z-component of the magnetization with time after an excitation pulse is

$$\frac{dM_z}{dt} = -\frac{M_z - M_0}{T_1} \qquad 1.11$$

where M_0 is the initial state of the magnetization along the longitudinal z-axis. The solution to this equation becomes [2]

$$M_z(t) = M_z(0) + M_0\left(1 - \exp\left[-\frac{t}{T_1}\right]\right) \qquad 1.12$$

If all the magnetization is rotated away from the longitudinal axis at time $t = 0$, then $M_z(0) = 0$ and from equation 1.12 at time $t = T_1$, $M_z(t) = 0.67M_0$. Another way to

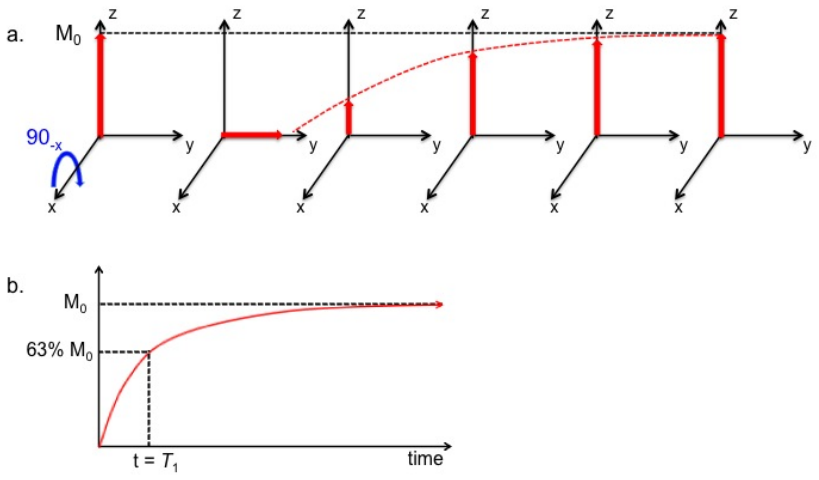

Figure 1.4. T_1 relaxation following a 90_{-x} pulse. a.) T_1 relaxation, also referred to as spin-lattice relaxation, causes the sample to relax back to thermal equilibrium along the z-axis. b.) T_1 relaxation occurs at approximately 63% of the bulk magnetization M_0.

state this is to say that T_1 occurs when approximately 67% of the bulk magnetization M_0 has recovered from the 90_{-x} pulse. This is illustrated in Figure 1.4. T_1 relaxation needs to be considered when setting up NMR experiments, especially the repetition time, T_R, of an experiment. A good approximation is to set T_R to be five times T_1, $T_R = 5T_1$. Typical T_1 times range from milliseconds to seconds, depending on the sample being studied and the temperature. For a pure water sample, $T_1 \approx 2.0$ seconds at 20°C.

Transverse relaxation, represented by T_2 and often referred to as spin-spin relaxation, occurs when the spins come to thermal equilibrium with themselves [4]. This relaxation occurs in the transverse plane and is due to random molecular interactions. The additional presence of fixed magnetic field inhomogeneities and distortions at sample interfaces and surface boundaries also contribute to transverse relaxation and results in dephasing of the spins. Decay due to the inhomogeneities and distortions of the magnetic field can be reversed using a pulse sequence to be described later. However, dephasing due to the random interactions of the spins cannot be corrected. For this reason scientists refer to two types of transverse relaxation times, T_2 and T_2^*. T_2^* incorporates both the random and the fixed sources of relaxation, while T_2 relaxation results from just the random interactions of the molecules. The evolution of the magnetization in the x-y plane after excitation is

$$\frac{dM_{x,y}}{dt} = -\frac{M_{x,y}}{T_2} \qquad 1.13$$

the solution of which is

$$M_{x,y}(t) = M_{x,y}(0)\exp\left(-\frac{t}{T_2}\right) \qquad 1.14$$

T_2 times can range from milliseconds to seconds, similar to T_1. However, T_1 is always greater than or equal to T_2 due to the additional mechanisms of relaxation that affect T_2. Figure 1.5 illustrates T_2 relaxation.

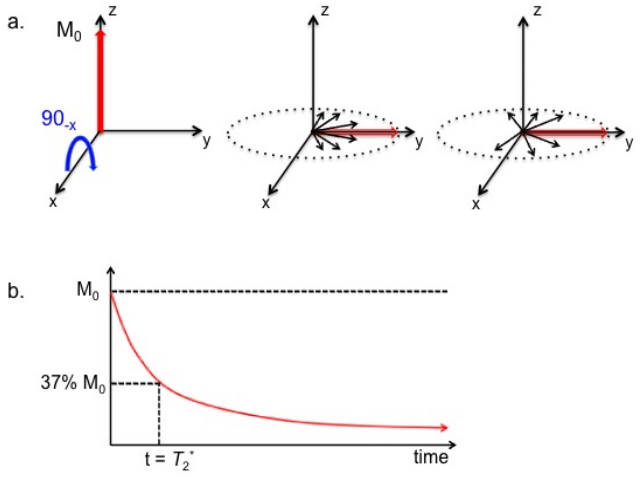

Figure 1.5. T_2^* relaxation following a 90_{-x} pulse. a.) A short time after the 90_{-x} pulse, the spins begin to dephase in the x-y plane due to T_2^* interactions. This dephasing can be caused by random molecular interactions as well as magnetic field inhomogeneities. b. T_2^* relaxation occurs at approximately 37% of the bulk magnetization M_0.

If all the magnetization is in the transverse plane at time $t = 0$ following a 90_x RF pulse, then $M_{x,y}(t)$ is at a maximum and $M_{x,y}(t) = M_0$ at this time $t = 0$. From equation 1.14 one can easily determine that at time $t = T_2^*$, $M_{x,y}(t) = 0.37M_0$. This can also be stated as the time at which 37% of the bulk magnetization M_0 has recovered from a 90_{-x} pulse is the T_2^* relaxation time.

Remaining in the rotating frame of reference and taking into account the additional consideration of relaxation, equation 1.9 becomes what are called the Bloch equations [4]

$$\begin{aligned}\frac{dM_x}{dt} &= \gamma M_y (B_0 - \omega/\gamma) - \frac{M_x}{T_2} \\ \frac{dM_y}{dt} &= \gamma B_1 - \gamma M_x (B_0 - \omega/\gamma) - \frac{M_y}{T_2} \\ \frac{dM_z}{dt} &= -\gamma M_y B_1 - \frac{M_z - M_0}{T_1}\end{aligned} \qquad 1.15$$

Introduced by Felix Bloch in the mid-1940s [1], these equations describe the evolution of the spin magnetization when relaxation is present.

Signal Detection and Processing

Experiments described in this thesis used both a high-field NMR system (Chapters 3 and 5) and a low-field system (Chapter 4). In both systems, the samples were placed in the middle of the magnet bore for analysis, where the magnetic field B_0 is the most homogeneous. For the low-field system, the samples were prepared in a plastic bottle (to be described further in Chapter 4) and the bottle placed in the middle of the device. The high-field system will be the focus of this section.

An RF coil generates the radio frequency pulse and subsequently detects the sample's decaying magnetization. For the high-field NMR equipment, the sample to be tested is inserted into the middle of the RF coil, which is then mounted onto a probe and inserted into the bore of the magnet as seen in Figure 1.6. The probe is designed so that

the RF coil, and therefore the sample, is positioned in the optimal location within the magnetic field.

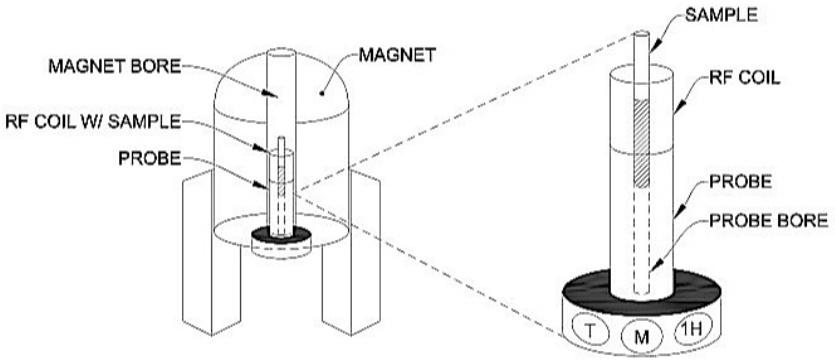

Figure 1.6. Illustration of experimental set up. The radio frequency (RF) coil is attached to the top of the probe and inserted into the magnet bore, effectively locating the sample at the optimal spot within the magnetic field.

Faraday's law of electromagnetic induction is employed in both the generation and detection of the signal in NMR. Faraday's law states that an oscillating magnetic field produces an electric field and vice versa according to the equation [5]

$$\nabla \times E = \frac{-\partial B}{\partial t} \qquad 1.16$$

First, currents are generated in the RF coil to produce a magnetic field oscillating at the Larmor frequency. Recall from the previous section that this energy input to the sample rotates the spins out of alignment with the static magnetic field. Following the pulse generation, the RF coil switches to become a receiver. The spins continue precessing around the z-axis as they relax back to thermal equilibrium. This precession produces an oscillating magnetic field. According to Faraday's law this oscillating magnetic field induces an alternating current in the RF coil, which is measured as a fluctuating voltage. As the spins return to thermal equilibrium, the signal decays exponentially due to T_2^*

relaxation. This exponential decay is called the free induction decay, or FID, and is shown in Figure 1.7.

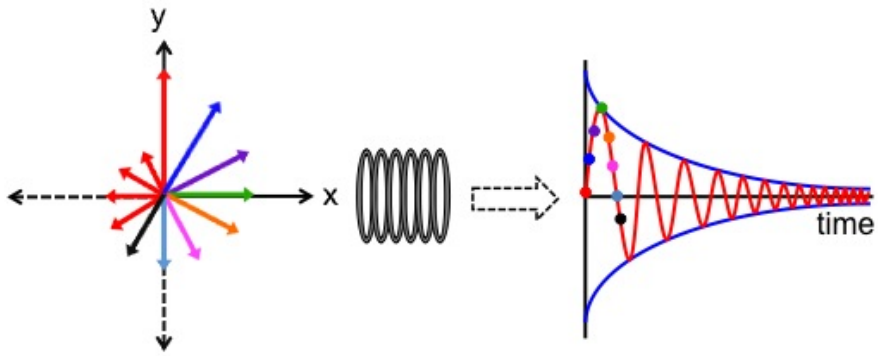

Figure 1.7. Free induction decay, or FID. The first few points of the FID are illustrated by the color-coded decay in the transverse plane and corresponding points that trace the received signal along the x-axis. The decay follows the envelope of the signal and is depicted by the blue line in the right hand picture.

Following acquisition, the signal is amplified and sent to the analog-to-digital converter, or ADC. As the name implies, the function of the ADC is to convert the NMR signal to a digital format. The amplified signal, which has been measured as a voltage, actually oscillates at a rate that is too fast for the converter to handle. Therefore, the signal frequency must be "down-converted" before it is processed [1]. The down conversion is accomplished by combining the detected NMR signal ($\omega = \omega_0$) with two signals produced by the quadrature receiver that are 90° out of phase with each other and oscillating at a frequency of $\omega = \omega_{ref}$. The result is two signals whose frequency oscillates at a relative Larmor frequency $\omega_{REL} = \omega_0 - \omega_{ref}$ [1]. The quadrature receiver then outputs these two signals

$$s_A(t) = \cos(\omega_{REL} t)\exp(-t/T_2)$$
$$s_B(t) = \sin(\omega_{REL} t)\exp(-t/T_2) \qquad 1.17$$

where s_A(t) is the real component and s_B(t) is the imaginary component of the original signal s(t) [1]. The production of two signals, real and imaginary, is important in that it provides for the distinction between signals with $+\omega_{REL}$ and $-\omega_{REL}$. The ADC then samples these signals at a specified time interval called the dwell time. The number of points collected for each FID can be selected by the experimenter and is typically a power of two. The greater the number of points sampled, the longer the signal acquisition time becomes.

Once the signal has been sampled, it is then subjected to a mathematical technique called the Fourier transform (FT). In this elegant process, the complex time-domain signal S(t) is converted to a signal in the frequency domain, $s(\omega)$ or $s(f)$, where ω is measured in radians s^{-1} and f in Hz with the relationship $\omega = f/2\pi$. The Fourier transform pair is given below [4].

$$F\{S(t)\} = s(\omega)$$
$$= \int_{-\infty}^{\infty} S(t)\exp(i\omega t)dt$$
and 1.18
$$F^{-1}\{s(\omega)\} = S(t)$$
$$= \frac{1}{2\pi}\int_{-\infty}^{\infty} s(\omega)\exp(-i\omega t)d\omega$$

One can easily transform a signal from the time domain into the frequency domain, as shown in the first part of equation 1.18, and just as easily get from the frequency domain to the time domain, given in the second part of equation 1.18. Note that the formulas in equation 1.18 are for measuring the frequency of the signal in radians per second. Using

the relationship between ω and f stated above, the Fourier transform pair can be deduced for f.

The Fourier transformation does not provide additional information; it simply makes the information available in the signal more interpretable [1]. Consider the example of a signal with only one frequency component that has been excited by a 90_x pulse. Figure 1.8 illustrates the evolution of the magnetization in both the time and frequency domains.

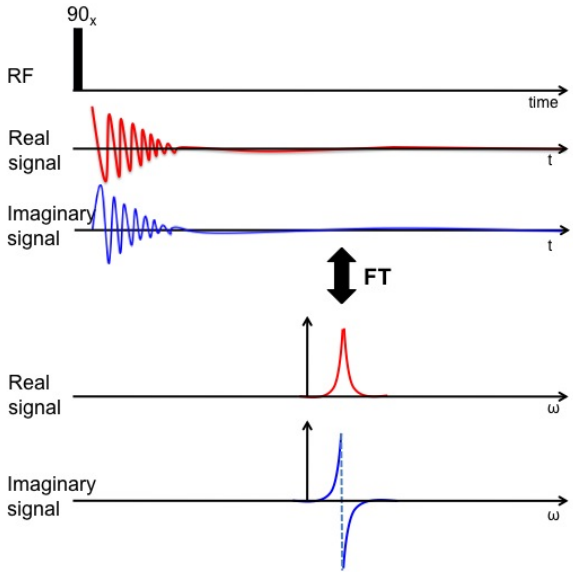

Figure 1.8. The Fourier transform of an NMR signal. The real and imaginary components of the signal $S(t)$ following a 90_x radio frequency (RF) pulse are drawn in the top portion of the figure and the Fourier transform of that signal into the frequency domain, $s(\omega)$ is shown in the bottom portion. As illustrated by the double-headed arrow, $s(\omega)$ can also be easily transformed back into the time domain [4].

The signal pictured in Figure 1.8 above contains only one frequency, ω_{REL}, which is slightly offset from the center frequency ω_0. The shape of the signal in the frequency domain is called a Lorentzian. Recall that both longitudinal and transverse relaxation is

exponential. The FT of an exponential function is the Lorentzian, which is why it is encountered so often in NMR. The real part of the Lorentzian is called the absorption Lorentzian while the imaginary part is the dispersion Lorentzian.

The Fourier Transform is used mainly for obtaining image and translational motion information. When measuring relaxation times, the Laplace Transform is often used, as the integration goes from 0 to ∞, rather than -∞ to ∞ as in the Fourier transform.

$$\begin{aligned} L\{f(R)\} &= S(t) \\ &= \int_0^\infty f(R)\exp(-Rt)dR \\ L^{-1}\{S(t)\} &= f(R) \end{aligned} \qquad 1.19$$

where R can be either T_1^{-1} or T_2^{-1} relaxation. The equation for the inverse Laplace transform is not given because it is an ill-posed problem, a description of which is beyond the scope of this thesis. For a detailed description, refer to [4]. To analyze the relaxation experiments outlined in this thesis, the author used a Matlab program "Inverse Laplace Transform (ILT)" provided by Sir Paul Callaghan and his research group in New Zealand.

A final consideration when processing MR data is that the signal from the spins is relatively small and contains noise. To improve the signal quality, multiple averages are taken in one experiment. The noise is random, so it does not add coherently. However, the signal does add, so having multiple averages improves the signal quality, but not the noise. For an experiment performed with N averages, the signal to noise improves as √N.

Gradients

The application of magnetic field gradients is essential for many experiments in NMR and can provide spatial and dynamic information, including imaging as well as diffusion and velocity measurements. Additionally, gradients can be used to remove unwanted signals in an experiment. These concepts will be explored below.

Gradient Applications

When starting an experiment in NMR, the experimenter takes great care in fine-tuning the magnetic field B_0, making it as homogeneous as possible throughout the entire sample. This is referred to as shimming and ensures that the spins experience the same magnetic field regardless of their location in the sample. With the application of a gradient pulse, however, the magnetic field is changed throughout the sample for the

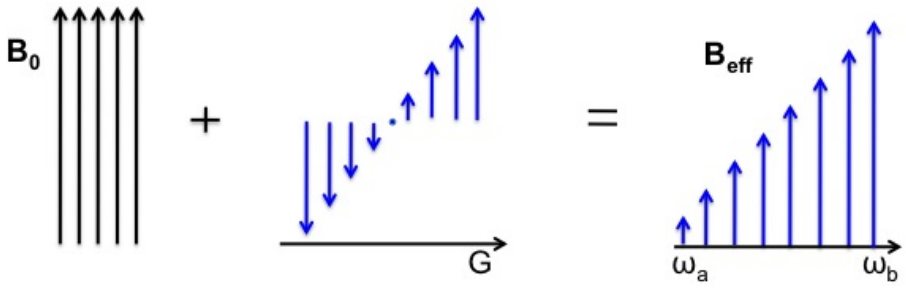

Figure 1.9. Effect of a constant gradient on the magnetic field, and therefore the frequency, across a sample. Note that the intensities of both the B_0 and gradient fields are not drawn to scale for illustrative purposes. The magnitude of B_0 is considerably greater than the magnitude of the gradient. The application of a gradient in either the x- or y-direction creates a varying frequency in these directions. Spins in the "right" side of the sample experience a stronger magnetic field, causing them to have a higher frequency.

duration of the pulses, but in a programmed linear manner. This change in magnetic field across the sample, and subsequently frequency, is given by equation 1.20 and illustrated in Figure 1.9 [4]. As an example, the application of a gradient in the x-direction, as

$$\begin{aligned} B(\vec{r}) &= B_0 + \vec{G} \cdot \vec{r} \\ \omega(\vec{r}) &= \gamma(B_0 + \vec{G} \cdot \vec{r}) \end{aligned} \qquad 1.20$$

shown in Figure 1.9, results in a linearly varying frequency along the x-axis.

$$\omega(x) = \gamma(B_0 + G_x x) \qquad 1.21$$

Also note in Figure 1.9 that the center of the sample is considered to be the zero point of the gradient, so spins above the centerline experience a larger magnetic field and spins below the center experience a smaller field. This means that the protons above the sample center precess faster than those below the centerline. From Figure 1.9 and equation 1.20, one can see that the frequency ω_a is less than ω_b due to this application of a stronger field. Initially following a 90_x pulse, the spins are all "in phase" in the x-y plane, as shown in Figure 1.10. Over time they shift out of phase with each other, causing a "dephasing" of the magnetization and a corresponding decrease in the amplitude of the detected signal. In the case of a linearly varying field or constant gradient, the spins in the sample can be thought of as being wound up like a helix as seen in Figure 1.10. The longer the gradient pulse is applied, the tighter the helix winds.

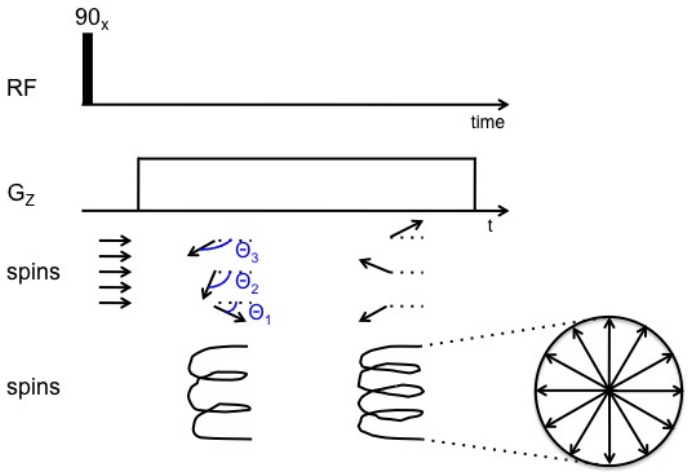

Figure 1.10. Application of a gradient following a 90_x radio frequency pulse. The spins are first all aligned together immediately after the 90_x pulse. However, the gradient begins to dephase the spins and winds them up in a helical shape. The longer the gradient remains on, the tighter the helix gets. If the helix is viewed from the top, it would appear as if all the spins were oriented in an orderly manner around the helix as shown in right-hand side of the figure.

Since the gradient also causes the spins to dephase, the application of a gradient can be used to purposely dephase unwanted signal. This technique is often employed in NMR. When the gradients are used in this manner, they are referred to as crusher gradients, or spoiler pulses. An example of undesirable signal would be following an 180_y pulse when some spins may not experience a perfect 180° flip into the -z axis and therefore end up in the transverse plane, resulting in unwanted signal picked up by the radio frequency coil. A crusher gradient would be applied following the 180_y pulse, dephasing any signal that may have ended up in the x-y plane and diminishing, or crushing it.

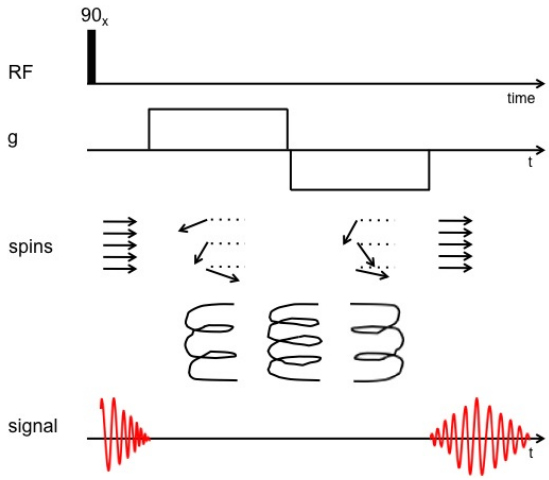

Figure 1.11. Gradient echo. Immediately following the 90_x pulse, all the spins are aligned and form a coherent signal. The first gradient then winds the spins in a helical manner. The application of the second gradient of opposite polarity, but same magnitude and direction as the first, will then unwind the spins. These spins will then realign to form a second coherent signal called an echo. This is called a gradient echo due to the use of gradients to produce it.

In a similar manner, gradients can also be used to rephase, or refocus, the spins to produce a coherent signal in the x-y plane called an echo. This echo will decay again in a similar manner to the FID produced by the 90_x pulse. When gradients are used to produce this coherent signal, it is referred to as a gradient echo and is illustrated in Figure 1.11. As seen in the gradient line, labeled 'g' in the figure, a negative gradient is used to reverse the phase shifts imposed by the positive gradient, producing the gradient echo shown on the line labeled 'signal'.

Pulse Sequences

Multiple different pulse sequences were used to acquire the data presented throughout this thesis. Descriptions and illustrations of the more general sequences are outlined in the following section.

Spin Echo Pulse Sequence

An echo is the refocusing of the spins to form a coherent and detectable signal in the transverse plane. As seen in Figure 1.11, strategic application of gradients will result in a gradient echo. An echo can also be produced using a second 180º RF pulse as shown in Figure 1.12 and is called a spin echo, discovered by Erwin Hahn in 1950 [6].

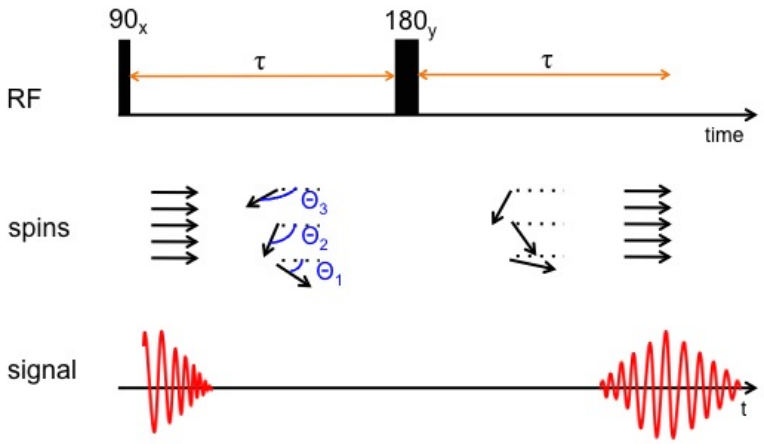

Figure 1.12. Spin echo. The application of a 90_x pulse rotates the magnetization into the transverse plane and for a very short time all the spins are aligned producing a coherent and detectable signal. However, due to magnetic field inhomogeneities and molecular interactions, the spins begin to dephase. Application of a 180_y pulse applied at a time τ after the 90_x excitation pulse will reverse the precession of the spins, resulting in the formation of another coherent and detectable signal, an echo, at time τ following the 180_y pulse. This is termed a spin echo.

In the Hahn spin echo experiment a 90° pulse is applied followed by a 180° pulse a time τ after the 90° pulse, resulting in an echo formation at the same time separation τ after the 180° pulse. Spin echo formation is shown in Figure 1.12. The application of gradients in the spin echo pulse sequence is commonplace in NMR and is used in several other pulse sequences outlined in this section.

Stimulated Echo Pulse Sequence

The pulse sequence shown in Figure 1.13 is called a stimulated echo. This method is used when the T_2 relaxation time is considerably shorter than T_1 or when the magnetization needs to be "stored" and used at a later time, such as in diffusion measurements (discussed in the upcoming section). The first 90_x pulse rotates the magnetization into the transverse plane, where it starts to dephase, as shown in "spins" row of Figure 1.13. At time τ the second 90_x pulse is applied. This RF pulse only acts on the y-component in the transverse plane, rotating it into the longitudinal axis and leaving the x-magnetization in the transverse plane [4]. The magnetization along the longitudinal axis is only subjected to the longer T_1 relaxation, and is thus said to be "stored" along the z-axis. During this storage time, t, a spoiler gradient can be applied to destroy the unwanted magnetization in the transverse plane [4]. This gradient has no effect on the magnetization stored along the z-axis. The third 90_x pulse brings the stored magnetization back into the transverse plane but with reversed precession direction so that a stimulated echo will form after the same time interval τ between the first and second 90_x pulses [7]. As only half of the magnetization that ends up in the transverse plane following the first 90_x pulse can be stored, the magnitude of the stimulated echo will be half of that for a spin echo.

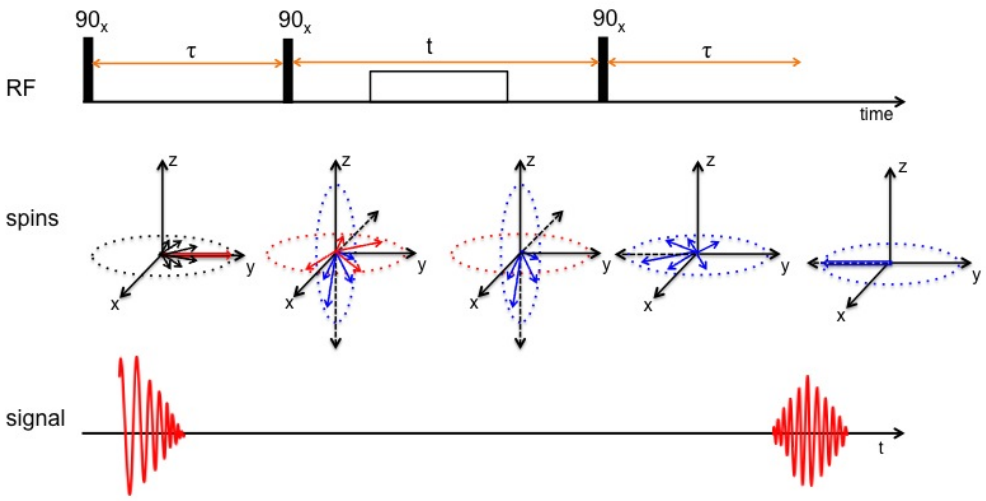

Figure 1.13. Stimulated Echo Pulse Sequence. The first 90_x radio frequency (RF) pulse rotates the magnetization into the transverse plane, where it begins to decay due to T_2 relaxation. At a time τ after the initial excitation pulse, a second 90_x pulse is applied which rotates only the y-magnetization into the longitudinal axis, where it is stored for a time t. Storage along the longitudinal axis protects the signal from fast decay due to T_2 relaxation and subjects the magnetization only to the longer T_1 relaxation. The x-magnetization remains in the transverse plane. Applying a gradient during the storage time t destroys this unwanted x-magnetization. At a time t, a third 90_x pulse is applied, which rotates the stored magnetization back into the transverse plane where it can be detected, but with a reversed precessional direction. This reversal results in an echo formation at time τ, the same time interval between the first two 90_x pulses.

Imaging Pulse Sequence

In the same sense that gradients cause spins to dephase, they impart a position-dependent phase to the spins, which can be visualized in the last line of Figure 1.10. The spins wind up a helix of phase in an orderly manner in the presence of a gradient. The phase shifts are proportional to the position of the spins in the gradient direction, for example the z-direction in Figure 1.10 [4]. When using gradients for imaging purposes, the concept of reciprocal space, or k-space, can be introduced, as well as the reciprocal space vector $\mathbf{k}$ [4],

$$\mathbf{k} = \frac{\gamma \mathbf{G} t}{2\pi} \tag{1.22}$$

where **G** is the amplitude of the gradient, γ is the gyromagentic ratio and t is the amount of time the gradient is applied.

k-space contains the spatial frequency information of the sample [8]. This spatial frequency is transformed into an image using the Fourier transform, introduced in equation 1.18, but modified here to include the concept of *k*-space and spin density in two or three dimensions [4]

$$\begin{aligned} S(\mathbf{k}) &= \int \rho(\mathbf{r}) \exp(i 2\pi \mathbf{k} \cdot \mathbf{r}) d\mathbf{r} \\ \rho(\mathbf{r}) &= \int S(\mathbf{k}) \exp(-i 2\pi \mathbf{k} \cdot \mathbf{r}) d\mathbf{k} \end{aligned} \tag{1.23}$$

where $S(\mathbf{k})$ is the signal and $\rho(\mathbf{r})$ is the spin density. Spin density is the volume of spins throughout the sample and determines the intensity of the signal at a given location. A part of the image with more protons will have a greater spin density and will appear brighter at that location. To successfully reproduce an image, the entirety of *k*-space must be sampled by applying varying magnetic field gradients.

Since signal is collected in the reciprocal space, each point in *k*-space impacts the entire image. The higher spatial frequency components of *k*-space, located in the outer rows of the matrix, contain the details of the image, while the lower frequency components provide the contour information of the image and occupy the inner portion of the matrix [8]. The *k*-space data is collected by the appropriate application of gradients in an imaging pulse sequence as shown in Figure 1.14.

The 90_x RF pulse applied in the imaging sequence of Figure 1.14 is called a soft, or slice selective, pulse and is used to selectively excite a specific range of frequencies in

the sample. The range of frequencies excited in a sample by the RF pulse is inversely related to the length of time the RF pulse is applied. Consequently, a longer RF pulse will excite a smaller range of frequencies in the sample and vice versa. In combination with a gradient, the slice gradient, a specific region of the sample is excited. The 180_y pulse in the middle of the pulse sequence of Figure 1.14 is called a hard pulse. Hard pulses are typically very short and excite all the frequencies in the sample.

The manner in which *k*-space is traversed is determined by the application of the gradients. If, for example, one assumes that the slice direction is along the longitudinal or k_z axis, then the read and phase gradients in Figure 1.14 are applied along the k_x and k_y directions. For an image of 256 by 128 pixels (k_y by k_x, for example), the k_y phase gradient would have 256 steps and the total experiment would finish after all 256 steps were taken. For each step, all 128 pixels would be collected in the k_x direction. For a finer resolution image, experimental time would increase with the number of points collected in the phase direction, k_y in this example. Once all these points are collected in matrix form, the data can then be transformed using the Fourier transform pair given by equation 1.23.

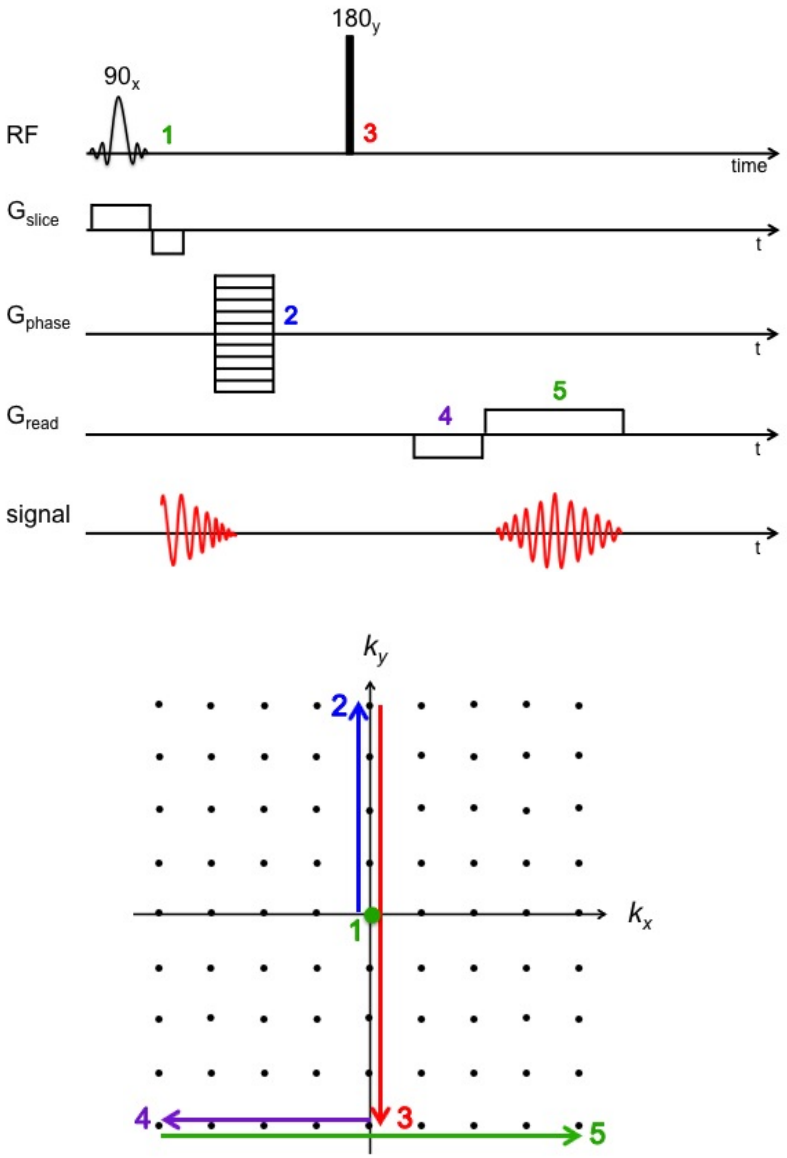

Figure 1.14. Imaging pulse sequence. The application of gradients is used in this pulse sequence to traverse *k*-space. The slice gradient together with the soft 90_x RF pulse is applied to selectively excite a specific slice of the sample, while the negative portion of the slice gradient acts to refocus the spins from this selective excitation. 1) The 90_x pulse puts the starting position in the middle of *k*-space. 2) The phase gradient moves the position in the positive and negative k_y dimension. 3) The 180_y pulse flips the location 180° from its position along the k_y axis. 4) The negative read gradient moves the position back to the left-most k_x position. 5) The positive read gradient steps through k_x collecting the data throughout the echo. This pulse sequence is repeated for all the steps of the phase gradient, thereby collecting all the *k*-space data. With each linear step of the G_{phase} gradient, a new column in the data matrix is created and filled with the data collected by application of the G_{read} gradient.

CPMG Pulse Sequence

The Carr, Purcell, Meiboom and Gill (CPMG) pulse sequence employs the use of the spin echo to obtain T_2 relaxation time(s) of the sample. Recall that T_2^* relaxation incorporates decay due to both fixed magnetic field inhomogeneities and random molecular interactions, while T_2 relaxation is just the relaxation incurred by the random interactions of the molecules. In other words, T_2 relaxation can be accurately measured if the field inhomogeneities of the system can be corrected. While it is impossible to have a perfect magnetic field, Hahn's discovery of the spin echo made it possible to correct for these field inhomogeneities [6]. Carr and Purcell improved upon Hahn's pulse sequence, and several years later Meiboom and Gill improved upon Carr and Purcell's, allowing a true measure of T_2 relaxation [9, 10]. The combined CPMG pulse sequence used to

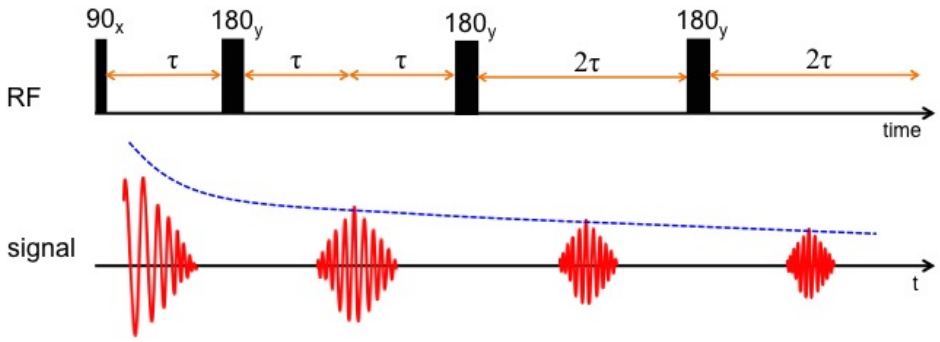

Figure 1.15. CPMG Pulse Sequence. T_2^* relaxation occurs due to inhomogeneities in the magnetic field and molecular interaction. Relaxation due to field inhomogeneities can be reversed using this pulse sequence. Application of sequential 180_y radio frequency (RF) pulses following a 90_x excitation RF pulse will continually refocus the magnetization at a time τ after the 180_y pulse. The exponential decay of the signal collected using this scheme gives T_2 relaxation. This pulse sequence was developed by Carr and Purcell and improved upon by Meiboom and Gill and is aptly named the Carr Purcell Meiboom Gill, or CPMG, pulse sequence. Irreversible relaxation due to molecular interactions cannot be refocused and thus results in decay of the signal.

reverse the effects of the field inhomogeneities is shown in Figure 1.15. The 180_y pulse train can continue until the signal is completely gone and can no longer be refocused. The attenuation of the echoes with each subsequent application of the 180_y pulse is a result of the random molecular interactions that cause irreversible relaxation, or real T_2 relaxation described by equation 1.13.

Translational Motion

Now that several pulse sequences have been introduced, an explanation of how they will be applied to obtain translational motion data will be described. The application of a gradient in the spin echo pulse sequence (Figure 1.12) results in a phase distribution of the spins, as described in the "Gradients" section, which is then reversed by the application of a 180° pulse. Another gradient of the same magnitude and direction is then applied. Assuming that none of the spins have undergone a translational motion, due to either diffusion or flow, in the time between the gradient applications, then a full echo can be expected at time 2τ from the first RF pulse. If they have undergone a uniform motion in the time between gradient pulses, Δ, then the spins will have a residual phase shift. These pulse sequences are often referred to as a pulsed gradient spin echo sequence, or PGSE, and the pulsed gradient stimulated echo sequence, or PGStE and are described below.

Translational Motion Gradients

Diffusion is the random motion of molecules in a fluid and the probability of molecular displacements for the random motion of diffusion is typically a Gaussian

distribution [11]. The bell-shape of the Gaussian distribution (Figure 1.16) is centered on zero displacement, indicating that most of the molecules will not have diffused in the time interval of observation and are still at the same position as the beginning of the experiment at time $t = 0$. Diffusional distances are governed by the geometry of the

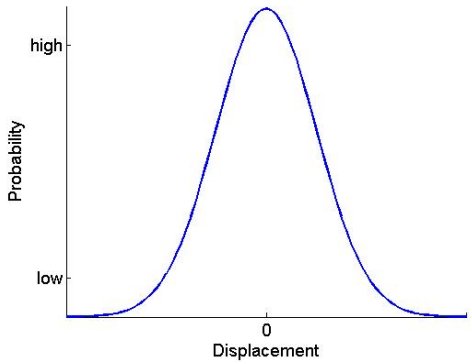

Figure 1.16. Gaussian distribution of displacement for molecular self-diffusion. This distribution shows that the probability is low that a molecule in a liquid will diffuse away from its starting position after a certain observation time. Most molecules will not have diffused, resulting in the high probability of zero displacement.

sample being studied. For the simple case of water in a test tube, the water molecules can diffuse as far as the test tube walls. For water in a porous medium, however, diffusion is limited to the size of the pore spaces in which the molecules are contained.

Analogous to *k*-space discussed earlier, diffusion and velocity are also described using a reciprocal space called *q*-space with the vector **q** defined as [4]

$$\mathbf{q} = \frac{\gamma \mathbf{g} t}{2\pi} \qquad 1.24$$

Though the definitions of the **k** (equation 1.22) and **q** vectors are similar, *k*-space refers to spatial images and uses **G** for the gradient pulse, and *q*-space refers to diffusion or velocity, using a lowercase **g** for the gradient pulse pair.

Diffusion

Molecules in a liquid undergoing self-diffusion will move randomly, attaining a broad distribution of phase shifts and resulting in an attenuation of the echo. Stejskal and

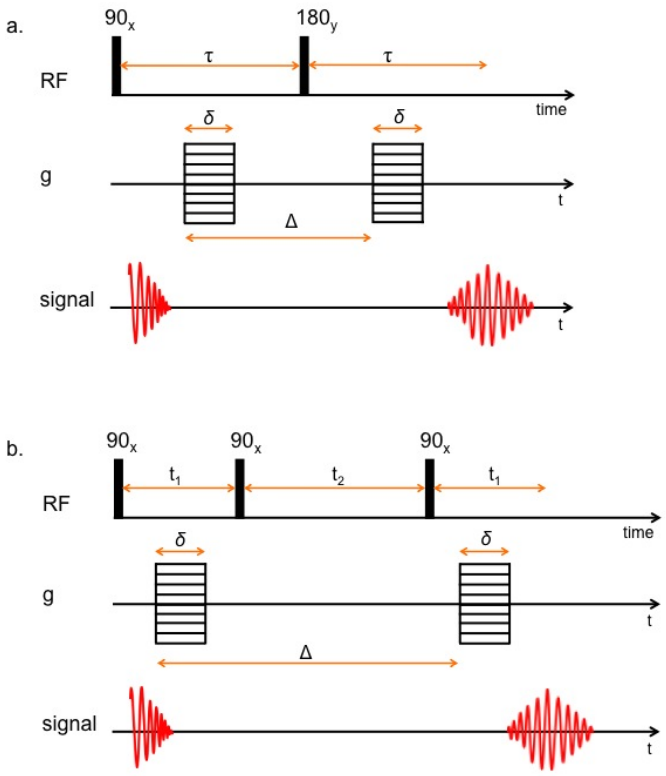

Figure 1.17. PGSE and PGStE pulse sequences. The use of a pulsed, short duration gradient pair in a spin echo or a stimulated echo pulse sequence creates two pulse sequences, the pulsed gradient spin echo (PGSE, shown in (a.)) and the pulsed gradient stimulated echo (PGStE, shown in (b.)) pulse sequences widely used in NMR. The first gradient of magnitude *g* and duration δ will encode the spins for frequency-dependent position. After an observation time Δ passes, a second gradient of the same magnitude and duration, but opposite polarity will decode the spins, elucidating a new position if the spins have moved. These pulse sequences are the basis for measuring system characteristics like diffusion and velocity.

Tanner [12] reported in 1965 that this attenuation can be used to determine the diffusion coefficient of the sample studied, provided that the gradient durations δ are short relative to any characteristic diffusion time as seen in Figure 1.17. They further introduced the pulsed gradient spin echo (PGSE, Figure 17.a.) and the pulsed gradient stimulated echo (PGStE, Figure 17.b.) pulse sequences to measure diffusion.

In their landmark paper Stejskal and Tanner also determined the equation for the calculation of the diffusion coefficient as a function of the signal attenuation

$$\frac{A(2\tau)}{A(0)} = \exp(-\gamma^2 D\delta^2 g^2(\Delta - \delta/3)) \qquad 1.25$$

where $A(2\tau)$ is the amplitude of the center of the echo at time 2τ when it is at a maximum; $A(0)$ the amplitude of the signal immediately following the 90_x pulse when the transverse signal is at a maximum; γ is the gyromagnetic ratio; D the diffusion coefficient; g the magnitude of the gradient; Δ the separation between the gradient pulses, also called the observation time; and δ the duration of the gradient pulse [12]. Plotting the natural log of this equation versus $\gamma^2\delta^2 g^2(\Delta - \delta/3)$ will give a straight line, the slope of which is the diffusion coefficient, D. Alternatively, rather than varying the time as equation 1.25 implies, the gradient amplitude could be varied giving

$$\frac{S(g)}{S(0)} = E(g) = \exp(-\gamma^2 D\delta^2 g^2(\Delta - \delta/3)) \qquad 1.26$$

where $S(g)$ is the echo amplitude acquired for gradient g and $S(0)$ is the echo amplitude acquired with no gradient. Because the signal acquired at the echo center is normalized by the signal acquired with no gradient, the effects of relaxation are essentially removed

and signal attenuation is simply due to diffusional effects. Using this method, diffusion coefficients can accurately be measured to 10^{-14} m^2 s^{-1} [4].

Propagators

The PGSE and PGStE sequences of Figure 1.17 are used to measure propagators, where the propagator is the probability density of a molecule having moved from a starting position **r** at time *t* to another position **r'** at time *t'*. It is essentially a probability of displacement of spins for a given observation time.

In the context of a PGSE or PGStE experiment (Figure 1.17) and discussed previously, the application of the first gradient imparts a position-dependent phase shift of $\gamma\delta\mathbf{g}\cdot\mathbf{r}$ to the molecule located at position **r** at time *t*. This phase shift is reversed by the 180° pulse and the application of the second gradient. If the position of the molecule following the second gradient is given as **r'** at time *t'*, then the net phase shift is $\gamma\delta\mathbf{g}\cdot(\mathbf{r'}-\mathbf{r})$ in the time interval $t' - t$ [4]. For a molecule that has not undergone any translation motion, this net phase shift will be 0.

For a propagator, this net phase term is weighted by the probability that a spin will have these starting and ending locations, given by $\rho(\mathbf{r})P(\mathbf{r}|\mathbf{r'},t)$ [4]. Recall from the "Imaging Pulse Sequence" section that the spin density $\rho(\mathbf{r})$ is essentially the amount of spins at a specific location in the sample. $P(\mathbf{r}|\mathbf{r'},t)$ is a conditional probability and is understood as the probability that the molecule moved to a position **r'** in time *t* given that it was initially located at **r**, the condition specified by the spin density $\rho(\mathbf{r})$. This conditional probability takes into account the fact that the starting time is irrelevant, just

that an amount of time t has elapsed. With these descriptions the relationship between the MR signal collected in a PGSE sequence and the propagator can be given as [4]

$$E(\mathbf{g},\Delta) = \int \rho(\mathbf{r}) \int P(\mathbf{r} \mid \mathbf{r}', \Delta) \exp(i\gamma\delta\mathbf{g} \cdot [\mathbf{r} - \mathbf{r}'])d\mathbf{r}'d\mathbf{r} \qquad 1.27$$

where $E(\mathbf{g},\Delta)$ is the amplitude of the center of the echo, the same designation as in equations 1.26, and $\Delta = t' - t$ is the observation time for **r** to translate to **r'**. If the definition of the vector **q** (equation 1.24) is substituted into equation 1.27, then

$$E(\mathbf{q},\Delta) = \int \rho(\mathbf{r}) \int P(\mathbf{r} \mid \mathbf{r}', t) \exp(i2\pi\mathbf{q} \cdot [\mathbf{r}' - \mathbf{r}])d\mathbf{r}'d\mathbf{r} \qquad 1.28$$

Two steps are taken to further simplify this equation, the first is a substitution of $\mathbf{R} = \mathbf{r}' - \mathbf{r}$, where **R** is the dynamic displacement space [4]. Recognizing that the spins can have any relative starting position **r** and move a distance **R** over a time interval of t, the concept of an average propagator is introduced, which is a sum over all these starting positions

$$\overline{P}(\mathbf{R},t) = \int \rho(\mathbf{r}) P(\mathbf{r} \mid \mathbf{r} + \mathbf{R}, t)d\mathbf{r} \qquad 1.29$$

Substituting these simplifications into equation 1.28 gives

$$E(\mathbf{q},\Delta) = \int \overline{P}(\mathbf{R},\Delta) \exp(i2\pi\mathbf{q} \cdot \mathbf{R})d\mathbf{R} \qquad 1.30$$

This equation has a similar form to the equations for the signal acquired in k-space and the associated spin density (equation 1.22), illustrating that this is another Fourier relationship. In this instance however, the signal acquired in q-space gives an image of the average propagator $\overline{P}(\mathbf{R},t)$ while the signal acquired in k-space gives an image of the spin density $\rho(\mathbf{r})$. If the propagator for molecular self-diffusion is given by

$$P(\mathbf{R},\Delta) = \left(4\pi D\Delta\right)^{-3/2} \exp\left[\frac{-\mathbf{R}^2}{4D\Delta}\right] \qquad 1.31$$

then the solution to equation 1.30, following a Fourier transform, becomes [4]

$$E(q,\Delta) = \exp(-(2\pi)^2 q^2 D\Delta) \qquad 1.32$$

Revisiting the equation for diffusion given by Stejskal and Tanner (equation 1.25) and substituting in the definition of $\mathbf{q} = (2\pi)^{-1}\gamma\mathbf{g}t$ (recognizing that t is the gradient duration δ), the same result is obtained for diffusion as that derived above using the propagator, but without the correction Stejskal and Tanner added to account for finite gradient times.

Velocity

The propagator concept is further used to analyze a system in which velocity is present. In the simplest case, a one-dimensional propagator, in the x-direction for example, could be collected for a given observation time Δ. A conversion from displacement (the propagator) to velocity would be as simple as dividing the propagator data by Δ, resulting in a distribution of velocities. This approach was taken for some experiments outlined in this thesis.

A second approach was taken for the final experiments described in chapter 5. Recall that the distribution of molecular self-diffusion is modeled by a Gaussian (Figure 1.13). Plotting equation 1.31 for the simple case of self-diffusion results in a Gaussian distribution centered on 0 displacement. For a system that includes a single constant velocity, the Gaussian distribution would be shifted and centered on that velocity, indicating that velocity imparts a phase shift to the whole system, $\Phi = i\gamma\delta\mathbf{g}\bullet\mathbf{v}\Delta$. Both

velocity and diffusion need to be accounted for in the computation of the echo amplitude and in terms of **q**, this is given by

$$E(q,\Delta) = \exp(i2\pi qv\Delta)\exp(-(2\pi)^2 q^2 D\Delta) \qquad 1.33$$

Since velocity is a coherent motion it can easily be factored out of the equation, leaving only diffusive attenuation of the signal.

Equation 1.33 demonstrates that diffusion affects the amplitude of the echo, while velocity affects the phase. This is advantageous when analyzing the data from a propagator experiment. If diffusion is desired, the magnitude of the signal is considered, which disregards the phase. For a velocity measurement, the phase shift of the signal is analyzed.

Multi-Dimensional Experiments

Additional experiments were performed for the research presented in this thesis that involved a combination of experimental techniques already described. These multi-dimensional experiments allowed the author to gather data for a combination of parameters at the same experimental time, which was important for the dynamic systems studied in chapters 3 and 5.

Propagator – T_2 Experiments

The PGSE and PGStE experiments used to obtain propagator data can be combined with other pulse sequences to also collect additional information within the same experiment. Figure 1.18 shows that a PGStE experiment can be combined with a CPMG pulse sequence to obtain a propagator-T_2 correlation experiment. Diffusion or

displacement is encoded in the first dimension by the PGStE and T_2 relaxation in the second dimension with the CPMG pulse train following the PGStE. The pulsed gradient g is increased linearly, and for each step in g the relaxation data is collected. Recall that the CPMG is a series of 180_y pulse followed by a time period 2τ with an echo collected at every time τ.

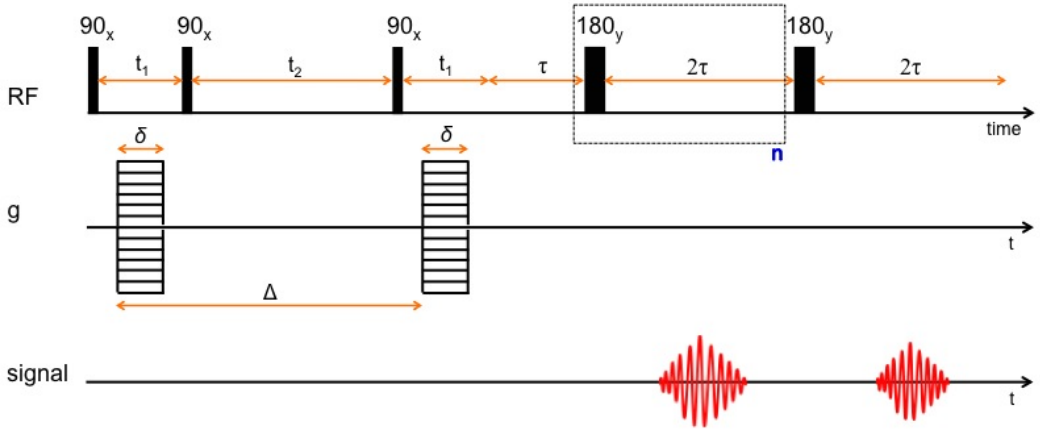

Figure 1.18. Propagator – T_2 pulse sequence. The first portion of the experiment is a PGStE experiment that encodes the spins for displacement. A CPMG pulse train is implemented in the second portion of the experiment to determine the T_2 relaxation time. For every gradient step in the PGStE experiment, n echoes are collected from the CPMG experiment, resulting in a two dimensional matrix, (number of gradient steps) × (n echoes collected).

To analyze the two-dimensional data, a Fourier transform is performed in the propagator dimension and a Laplace transform in the relaxation dimension. An example of the data obtained from this type of experiment is given below, where the notation $P(Z, \Delta)$ is used to indicate that the propagator information was obtained in the Z, or longitudinal, direction for a given observation time Δ. From Figure 1.19 it is easy to see that displacement information can be effortlessly correlated with relaxation time from a single two-dimensional experiment. This data would have been more difficult to ascertain from

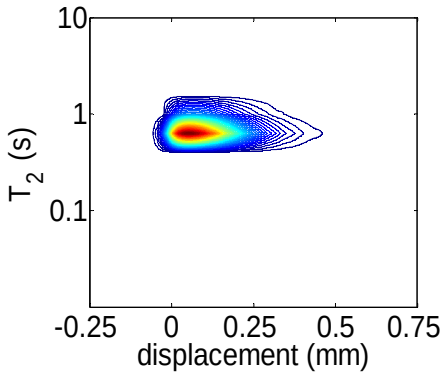

Figure 1.19. Example of $P(Z, \Delta) - T_2$ data. Correlation between displacement and relaxation can easily be seen in this example.

multiple one-dimensional experiments, especially if the system is dynamic such as the case for a growing biofilm.

Velocity Imaging

Measuring velocity in a system with a one-dimensional propagator experiment yields a distribution of velocities, but not the location of each velocity within the sample. To obtain that information, a velocity imaging experiment must be performed. A PGSE experiment can be combined with an imaging sequence to obtain a velocity image. For the velocity imaging experiments in this thesis, two points were collected in q-space, the first a reference q-point where $q = 0$ and the second a finite point in q-space, q_1. The phase shift is determined by comparing the finite point in q-space to the reference point of $q = 0$ such that

$$\frac{E(q_1,\Delta,\mathbf{r})}{E(0,\Delta,\mathbf{r})} = A\exp(i2\pi qv\Delta) \qquad 1.34$$

where A is the amplitude of the signal, and due to diffusion, can be considered to be less than one. The phase of the right hand side of equation 1.34 can easily be determined,

knowing that the exponential function can be broken down in to real and imaginary components (cosine and sine, respectively). Generally, more points are taken in *q*-space for a diffusion experiment than for the method described here for a velocity imaging experiment, but at the cost of total experiment time. To improve the signal to noise ratio for the velocity experiments with only two *q*-points, more averages were taken.

An imaging sequence pulse sequence is combined with the two-*q*-point PGSE experiment just described to generate the velocity imaging pulse sequence shown in Figure 1.20. In this pulse sequence, both *k*-space and *q*-space are sampled.

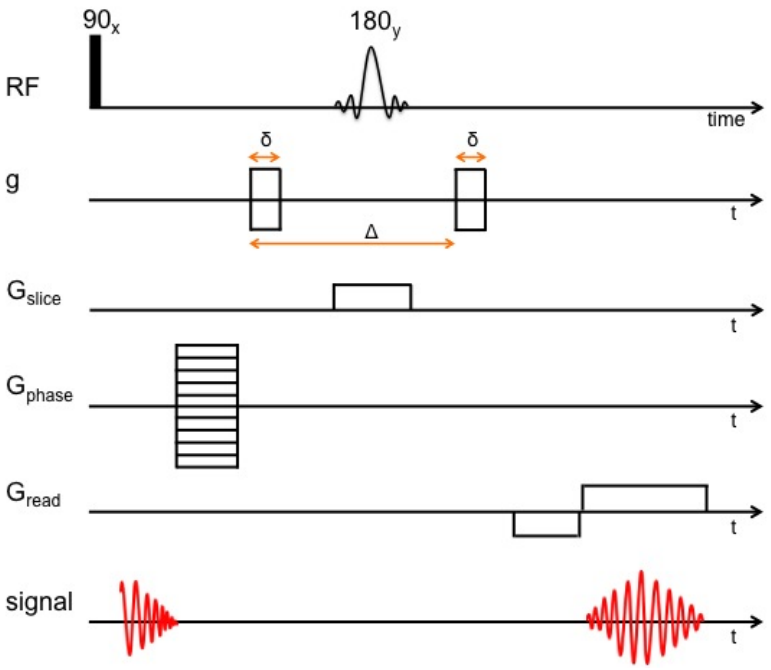

Figure 1.20. Velocity image pulse sequence. A hard 90_x pulse is used to excite all the spins in the sample before encoding for position and velocity. A soft 180_y pulse is used to selectively excite a slice of the sample for imaging. The imaging gradients are applied such that *k*-space can be traversed and the propagator gradients are applied to collect *q*-space velocity information.

Velocity images are three-dimensional experiments with one dimension encoding for velocity and the other two for the image itself. Velocity can be measured in any of the three standard directions by simply changing the axis along which the velocity encoding gradient is applied, just as the image can be taken in any two directions in *k*-space by adjusting the imaging gradients. Similar to the $P(Z, \Delta)$-T_2 analysis, a three-dimensional transform will be made to obtain an image with the velocity information contained in each pixel. Velocity images give a multitude of information on system characteristics including hydrodynamic instabilities, obstructed flow in porous media and blood flow in the human body.

CHAPTER TWO

INTRODUCTION TO POLYMERS

Basics of Polymers

Polymers are ubiquitous in everyday life. One cannot go through a day in this era without coming into contact with a polymer, either through wearing a synthetic [13] or natural polymer or using a product manufactured from natural and synthetic polymers. DNA, proteins and polysaccharides that compose the human body and bacterial colonies are all forms of polymers.

Polymers are a very broad classification that includes natural materials, such as silk, wool, and proteins, as well as manufactured compounds like plastics derived from petroleum. In general, a polymer is a compound composed of repeating single monomer units that are chemically bound together. Polymers have a range of molecular weights and chemical properties and can easily be manipulated into different shapes and sizes. They are used in practically every industry in one form or another from the food we eat [14-18] to medical devices that save our lives [19-23], and are also constituents of algal and bacterial cells and colonies [15, 24-31].

The ubiquity of polymers is easily seen in the numerous industries that rely on polymer compounds, as well as the drive to discover better polymers. In electronics, polymers are used in the manufacturing of photovoltaics and photodiodes [32, 33]. For rechargeable lithium-ion batteries, solid polymer compounds are considered to be one of the best candidates for the electrolyte due to their higher energy density and safety

compared to corrosive or explosive liquids currently in use [34]. Advances in polymer chemistry have led to yet another class of polymers called supramolecular polymers, monomers that are held together by directional and reversible secondary interactions like hydrogen bonds, the self-assembly of which is thermodynamically favorable [35, 36]. Polyhydroxyalkanoates (PHA) are a class of natural plastic-like polymers made intracellularly by a multitude of gram-positive and gram-negative bacteria [37, 38]. Another class of natural polymers, polylactic acids (PLA), in use in the medical industry for decades [39, 40], have also garnered attention as an alternative to petrochemical plasics [41, 42].

Polymer compounds could be considered the miracle components of the medical industry. Polymers seeded with nerve cells have been used to regenerate peripheral nerves in animal models [19]. Skin graft scaffolds made of a polymer compound are used for wound healing in burn victims [43, 44]. Hutmacher describes polymer compounds used as scaffolds for cartilage and bone reconstruction [23].

In the pharmaceutical industry, polymers are used as binding and delivery agents as well as the drugs themselves. Polymer-drug conjugates have been investigated as an effective means of delivering drugs and imaging materials to target cells [20, 21]. Control of the molecular weight and biomimetic capabilities of each compound considered for drug delivery can be achieved through polymer chemistry [22].

Due to the universality of polymers, examples of products, both natural and synthetic, as well as the myriad uses for these compounds could continue indefinitely. However, the focus of the last chapters in this thesis will be on the polymer

polyacrylamide, used in flocculation and enhanced oil recovery, and the biopolymer alginate, used a thickening agent and a major constituent of biofilms.

Polyacrylamide

Polyacrylamide is a polymer formed by the bonding of acrylamide monomers in either long-chain or cross-linked formation [45-47]. For many decades polyacrylamide, abbreviated PAA, has been used as an agent in DNA fingerprinting [48-52], as a flocculant in waste water treatment [45, 47, 53, 54], in the recovery of minerals [55] and oil [56-60], and more recently as a soil stabilizer [61]. Like the other polymers described in this chapter, PAA has many applications.

With a double bond and amine group (see Figure 2.1), acrylamide has been termed a "polyfunctional molecule" due to its susceptibility to a wide range of chemical reactions at these two sites that can alter its characteristics [54]. Though typically charge-neutral, polyacrylamide can be transformed into both cationic and anionic forms through nucleophilic addition reactions and free radical substitution reactions [54].

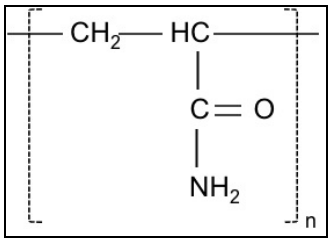

Figure 2.1. Acrylamide monomer unit.

As a cross-linked gel, PAA has been used extensively as an aid in separating DNA in a process called polyacrylamide gel electrophoresis, or PAGE [48-52]. The

amount of polyacrylamide and stabilizing agent used in the preparation of the gel determines the pore size of the gel, which can be adjusted according to the size of the proteins being separated [48]. Having the characteristic of hydrophilicity as well as high water solubility, PAA has been used to separate minerals from the slurry in a solid-liquid separation process, absorbing the water in the slurry and leaving the minerals behind [55].

In furrow irrigation, runoff and drainage losses are greater than with other forms of irrigation like sprinkler irrigation. In addition to soil erosion and an inconsistent distribution of nutrients to the crops, furrow irrigating poses a threat to the surrounding environment as pesticides and contaminants like phosphorus and nitrogen enter the local water table [61]. In a study conducted on an Idaho farm, adding PAA at a low concentration (10 mg L^{-1}) during the inflow stage of furrow irrigating resulted in a 94% reduction in soil loss, as well as over 90% reduction in contaminant runoff [61].

For enhanced oil recovery, polymers, especially PAA and PAA derivatives, are used as components of drilling fluids [56], as stabilizers for water-sensitive shales [57], and as fracturing fluids [59]. These polymers need to be viscous, compatible with corrodible materials [57], and stable at elevated temperatures, as most recovery procedures are performed at high temperatures and pressures [57, 60]. When flooded into a reservoir, the polymer solution experiences high shear forces [60]. Shear thinning fluids are preferred for this application as the fluid viscosity reduces under these high shear conditions, allowing for easier flow into the reservoir. Additionally, the presence of high levels of dissolved salts in the briny waters of oil fields can cause the polymers to

gel, reducing their hydrodynamic volume [56]. Finding a polymer compound that has all the characteristics – shear resistance, temperature stability and brine compatability [60] – has been a challenge for the oil industry. Polymer compounds and specifically derivatives of polyacrylamide, are being developed to encompass all of the desired attributes. Philippova et al. [59] described two "smart" polymers, one a PAA copolymer, developed for the purpose of blocking water influx into the oil reservoir and for hydraulic fracturing.

In the treatment of waste-water systems, the water soluble nature and polyionic versatility of PAA has made it an ideal candidate as a flocculating agent. Molecular weight and charge density are important characteristics of the flocculant, where a high molecular weight is generally preferred [45, 47]. The molecular weight of PAA polymers can range from a few thousand up to tens of millions [45, 47]. The ionic attributes of the polymer and of the solution in which it is mixed can cause the polymer to coil or expand, depending on the charge density of polymer segments [45, 47]. Charge neutralization and polymer bridging are two mechanisms by which these polymers clear waste. For polyelectrolytic PAA, the linear polymer can adsorb onto the surface of an oppositely charged particulate, creating a rather strong bond. Anionic polyacrylamide can also bind to negatively charged particles through the linking of a divalent cation such as Ca^{2+} [45, 47], similar to the egg-box formation of alginate in the presence of Ca^{2+}. In polymer bridging, the long chain polymers, which have characteristic lengths much greater than the diameter of the particulate matter, can have "tails" that extend into

solution following adsorption onto the surface of a particulate. These dangling polymer segments can attach to other particles, creating a "bridge" between them [45].

Understanding how these polymers function in shear stress conditions is imperative for the manufacture of better polymer compounds. Under shear conditions, the linear polymer chains extend resulting in ruptured bonds and subsequently reduced molecular weight, seriously impairing the function of the polymer in the oil reserve flooding, furrow irrigation and water treatment indications [45]. The final chapter in this thesis presents data on the behavior of polyacrylamide under different shear conditions.

Alginate

Alginate, a natural biopolymer derived from brown algae and several species of bacteria, has found widespread importance in numerous industries. Applications in the food industry include use as a thickening agent [15, 16] and as an appetite suppressant in weight management products [18]. Because of its ability to bind divalent cations, alginate has also been developed for the biosorption of heavy metals from the environment [24, 62]. More recently, alginate has been explored as a binding agent in the manufacturing of lithium-ion battery anodes [25]. Alginate has also been used as a cell immobilizer, encapsulating bacteria, vaccines, and other drugs for targeted delivery in sensitive environments [14, 17, 26, 27, 63, 64]. Scaffolds manufactured from alginate compounds have become commonplace in the tissue engineering community [65, 66], where it is frequently employed as a skin graft dressing [43, 44] and as the mechanical support for the regeneration of cardiac tissue [67].

Alginate has been isolated from the cell wall and intercellular components of several species of brown algae including *Laminaria hyperborean*, *Ascophyllum nodosum*, and *Macrocystis pyrifera*, as well as the bacterium *Azotobacter vinelandii* and several *Pseudomonas* species, mostly in the form of sodium alginate [24, 26]. A linear polysaccharide, alginate is composed two monomers, β-(1,4)-□-mannuronic acid monomers and α-(1,4)-□-guluronic acid monomers, from here on referred to as M and G units, respectively, and shown in Figure 2.2 [15, 24-26]. These monomers do not bond in a predictable or consistent manner. In fact, the conditions in which the algae grow determine the amount of the alginate produced within the algae, as well as the composition and arrangement of the M and G units [24, 25, 27]. Bacterial alginates differ from their algal counterparts in that the M units are acetylated [68]. Alginate can therefore be considered a heterogeneous and variable polymer.

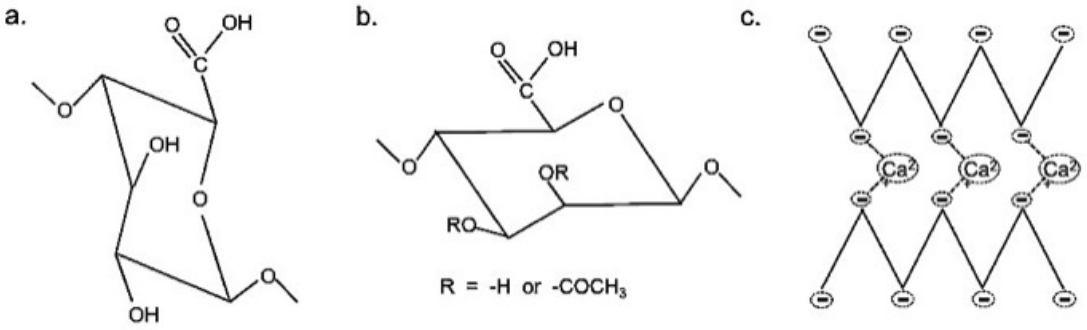

Figure 2.2. Alginate monomers and egg box configuration. The monomers α-(1,4)-□-guluronic acid (a.), G units, and β-(1,4)-□-mannuronic acid (b), M units, compose the biopolymer alginate. When exposed to a divalent cation such as Ca^{2+}, the alginate forms a gel (c.) with an egg-box structure.

When exposed to a divalent cation, specifically Ca^{2+}, alginate rapidly forms a gel. Mg^{2+} and monovalent cations do not cause gelation of alginate [26]. Multiple G units linearly bonded together, polyguluronic groups, play an important role in the gelation process. In the presence of Ca^{2+} or other divalent cations of similar size, these polyguluronic groups exchange sodium ions for the divalent cations, forming a cross-linked configuration referred to as an egg-box structure, shown in Figure 2.2 [24, 26]. These gels are quite strong and comparable to solids in that they retain their shape under stress [26]. It is this immediate gelation characteristic of alginate that has led to its use as an immobilizing or encapsulation agent [24, 26, 27].

As mentioned earlier, alginate is produced by the bacteria *P. aeruginosa* and is a component of the slime associated with a biofilm [28, 29, 68-73]. In the research presented in chapter 4, NMR characteristics of alginate before and after gelation in different sand compositions are compared to bacterial biofilm formation in these sands. The alginate used in these experiments was from a single source and was therefore consistent from one experiment to the next.

Biofilms

In planktonic form, bacteria are freely suspended in solution. When these free floating bacteria land on a surface, they begin a process of adherence that leads to biofilm formation. The biofilm development includes the production of an extracellular matrix composed of polymers including polysaccharides, proteins and nucleic acids [74]. Biofilms consist of up to 80% of this extracellular polymer matrix [28], and will be classified as a polymeric gel in the research presented in this thesis.

While in the planktonic stage, bacteria are suspended in a fluid such as seawater, synovial fluid, blood, or growth medium in the laboratory setting. Bacteria were thought to survive in this form, living in homogeneous suspended populations [74]. As such, this form of bacteria was traditionally the focus of early microbiology and a target for antimicrobials. It was not until the last few decades that scientists began to universally recognize that bacteria live in sessile heterogeneous communities in a multitude of moist environments from the hulls of ships, to industrial heat exchangers, to implanted and extracorporeal medical devices [28-30, 69-74].

The process of biofilm formation occurs in several steps. In the first step, the bacterium approaches a surface, by processes like Brownian motion, gravity or surface attracting charges, slowing motility [28, 72, 74]. It then forms a transient adherence to the surface while it searches for a suitable location, using either flagella or pilli to move around the surface [30, 72, 73]. Once the bacterium finds a suitable location, it "settles" on the surface and begins a process of permanent attachment. This is characterized by the excretion of extracellular polymeric substances (EPS), which not only helps irrreversibly secure the cell to the surface, but also protects the bacterium from biocides and host immune responses [28-30, 70-74].

Some planktonic bacterial cells tend to settle together and move across the surface towards each other to form clusters, or microcolonies, on the surface [72, 73], the second stage of biofilm development [74]. These microcolonies are the basic organizational units of the biofilm and are heterogeneous in nature. The architecture is one similar to a major urban area with large towering buildings. The microcolonies grow upwards in

towers and mushroom-shaped structures protected by the polymer matrix [29, 69]. Most biofilms found in natural ecosystems contain multiple species of bacteria living in a symbiotic community [28, 30, 69, 72, 75, 76]. However, biofilms found on medical implants are typically composed of one species. Fluid channels also permeate the biofilm structure, allowing for convective transport of nutrients, oxygen and even antimicrobial agents to and from the microcolonies [28-30, 75].

As the biofilm develops and matures, the third stage of development, these microcolonies – and the microenvironments within – also change. Cells at the substratum of a thick biofilm exhibit reduced metabolic rates due to a decrease in available substrate, resulting in a stratification of cell densities within the microcolonies [29, 70, 74]. Measure of oxygen and pH levels at the substratum are also lower than at the outer regions of the biofilm [72]. An example illustration of the architecture of a biofilm is illustrated in Figure 2.3 below.

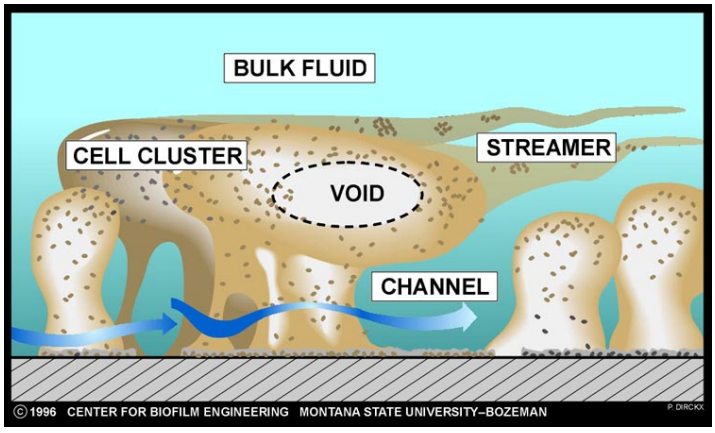

Figure 2.3. Illustration of the heterogeneous nature of biofilms. Image from the Center for Biofilm Engineering, Montana State University.

Metabolic and structural changes take place in the bacteria living in the sessile state. Following adherence to the surface, the planktonic bacteria undergo phenotypic changes, up- and down-regulating different genes, with a more than 50% difference in the proteins expressed from the sessile versus planktonic cells of the same species [28, 71-74]. For example, *Pseudomonas aeruginosa* up-regulates genes associated with EPS formation and down-regulate genes associated with flagellar synthesis after attaching to a surface [28, 72, 73].

These changes and subsequent development of the biofilm and microcolonies occur through cell-to-cell signaling within the biofilm [28, 69, 72, 73, 77]. Quorum sensing, as this cell communication is called, occurs by the diffusion of these "pheromones" through the polymer matrx [72, 78]. Peptides, fatty acids, genetic materials and other proteins excreted by the cell could function as quorum sensing molecules [72, 78].

Quorum sensing plays a role in the detachment of biofilm cells, the final stage of biofilm development. Shedding of daughter cells, removal of small portions of the biofilm due to shear forces or detachment due to quorum sensing results in dispersion of the biofilm [28]. In the case of quorum sensing, a critical concentration of the "pheromone" molecule accumulates in the biofilm, signaling that the bacterial population density has reached a critical point and stimulating a change in the bacterial behavior [78]. Reduction in available nutrients and changes in microenvironmental pH could also be a potential cause of the detachment [69, 78]. Detachment of the biofilm provides a potential mechanism for recolonization in a different location [69].

Antibiotics, vaccines and biocides have proved successful in suppressing infection and contamination of modern devices. However, these agents were effective against the planktonic variants of bacteria, not the biofilm-associated bacteria. Resistance to antimicrobial agents, industrial biocides and host immune defenses has led many to postulate that the EPS is a protective polymer matrix that limits diffusion within the biofilm [28, 30, 69-71, 74]. A second hypothesis is that cells within the biofilm microcolonies residing in substrate-limited conditions have reduced metabolic and growth rates [29, 30, 69, 71, 74]. These slowed rates result in less susceptibility. The transport of biocides and antibiotics into the biofilm is still a question that needs to be answered in order to more effectively eradicate destructive biofilms or support beneficial ones.

This life cycle of the biofilm was observed in experiments described in Chapter 3. Additionally, the topic of convection in the biofilm was also examined in Chapter 3. In chapter 4 a biofilm was grown in a sand column and a low-field NMR system was used to determine if biofilm detection was possible.

CHAPTER THREE

PERMEABILITY OF A GROWING BIOFILM IN A POROUS MEDIA FLUID FLOW ANALYZED BY MAGNETIC RESONANCE DISPLACEMENT-RELAXATION CORRELATIONS

Contribution of Authors and Co-Authors

Manuscripts in Chapters 3 and 4

Author: Sarah J. Vogt

Contributions: Helped conceive and implement the study design. Helped collect and analyze data. Wrote manuscript.

Co-Author: Alexis B. Sanderlin

Contributions: Helped implement the study design. Helped collect and analyze data. Provided feedback and comments on the manuscript.

Co-Author: Joseph D. Seymour

Contributions: Helped conceive and implement the study design. Provided feedback and comments on the manuscript.

Co-Author: Sarah L. Codd

Contributions: Helped conceive and implement the study design. Provided feedback and comments on the manuscript.

Manuscript Information Page

Sarah J. Vogt, Alexis B. Sanderlin, Joseph D. Seymour, Sarah L. Codd
Biotechnology and Bioengineering
Status of Manuscript: (Put an x in one of the options below)
____ Prepared for submission to a peer-reviewed journal
____ Officially submitted to a peer-review journal
____ Accepted by a peer-reviewed journal
_X_ Published in a peer-reviewed journal

Wiley-Blackwell
Vol. 110, No. 5, Pages 1366-1375, May 2013

PERMEABILITY OF A GROWING BIOFILM IN A POROUS MEDIA FLUID FLOW ANALYZED BY MAGNETIC RESONANCE DISPLACEMENT-RELAXATION CORRELATIONS

Abstract

The study of biofilm growth in porous media poses significant difficulty due to the heterogeneous nature of the biofilm as well as the opaqueness of the environments in which the biofilms form. In this study nuclear magnetic resonance was used to non-invasively observe biofilm growth in a model porous media under different growth conditions by varying the strengths of growth media. Displacement-relaxation correlation experiments were performed by applying a PGSE experiment in one dimension to encode for displacement and a CPMG experiment in the second dimension to ascertain the relaxation characteristics. By correlating the relaxation time with the flow dynamics within the same experiments, we were able to differentiate between the bulk fluid phase and the biofilm phase while simultaneously perceiving how the biofilm growth affected the hydrodynamics. Consistent with current literature, no convective flow was observed within the biofilm.

Introduction

Biofilm growth on moist surfaces has many implications in today's society, from dangerous chronic infections of implanted medical devices to use as a biobarrier against toxic waste seepage into the environment and local water sources. Biofilms are formed when bacterial cells attach to a surface and begin to grow in a phenotypically altered state [28, 30, 68-72, 74]. Adherence to the surface is achieved by the bacterial excretion of a biopolymer called the extracellular polymeric substance (EPS), which consists of proteins, polysaccharides and DNA [28, 30, 68-72, 74]. Fluid channels are formed throughout the biofilm as a means of nutrient and waste exchange by means of diffusion into and out of the biofilm. Not only does the EPS enable the bacteria to stick to a surface, but it also provides protection from biocides and antimicrobials through this limited diffusive process. As such, biofilms are difficult to eradicate.

Observation of biofilm growth in porous media is challenging due to the heterogeneous nature of the biofilm, the cloudy quality of most growth media needed to support biofilm survival and the opaque nature of the surfaces on which biofilms form. Therefore, researchers have developed models to simulate biofilm growth, varying parameters such as growth rates and geometries [79] and more recently incorporating key biofilm processes such as quorum sensing and permeability [77, 80]. Biofilm permeability is an important feature for the models to adequately describe biofilm behavior, as it provides the basis for quantifying the transport of nutrients (and biocides) into the biofilm. Accurate models of biofilm growth would allow for better control of these biofilms in real situations.

Permeability of the nutrients and biocides is directly related to the transport of these to the biofilm. It has been well documented that biofilm architecture is composed of cell clusters, or microcolonies, surrounded by interstitial voids or channels [28-30, 75]. These channels provide a means of convective transport of nutrients (as well as antimicrobial agents) to the biofilm and of waste from the biofilm. DeBeer et al. [76] provided evidence for convection around cell clusters in a living biofilm using confocal microscopy. In these experiments, fluorescent latex spheres were imaged as they flowed through the channels of the biofilm, but not through the cell clusters. The authors concluded that both convection and diffusion contribute to mass transport in the interstitial voids but diffusion was the only mechanism for mass transport within the microcolonies.

The amount of convective flow through a biofilm in biofouled porous media is still being debated. Due to the heterogeneous nature of the biofilm and limited tools for quantifying nutrient uptake *in situ*, realistic permeability and convection data is difficult to obtain. The work presented in this article offers a relatively novel approach to studying biofilm development and lends credence to the model that convection does not occur through the biofilm.

Magnetic Resonance

The use of magnetic resonance (MR) has gained attention as a non-invasive manner in which to observe biofilms. Analysis of components of the polymer matrix [81], relaxation experiments [31, 82, 83] and dynamic measurements [84, 85] using nuclear magnetic resonance (NMR) have supported the details regarding the

heterogeneity of biofilms, as well as demonstrated that biofilms create secondary flows even in low Reynolds number conditions. In these experiments, the researchers performed relaxation and dynamic measurement experiments separately and then compared the results. MR imaging experiments were also coupled with relaxation measurements when monitoring a biofilm growing in a capillary system [86, 87]. In recent experiments, dynamic MR experiments were used to study transport through a biofouled porous system as a whole, but could not distinguish between the biofilm phase and the bulk fluid [84, 85]. The displacement-relaxation correlation experiments performed for this research relate the relaxation information to the molecular motion using a single experiment [4]. Acquisition of the relaxation data in concert with the dynamic data also allowed for distinction between the biomass and the bulk solution.

Measurement of Molecular Motion Using MR: To measure molecular motion using MR, two pulse sequences are typically utilized, a pulsed gradient spin echo (PGSE) pulse sequence, or a variation used in the experiments conducted in this research called the pulsed gradient stimulated echo (PGStE). In both of these experiments, the application of linearly varying gradients and different radio frequency (RF) pulses encode the hydrogen nuclei (^{1}H), or protons, for position [2, 4, 12]. After a time of Δ passes, which allows the spins to move randomly due to diffusion or coherently due to flow, a new position is encoded by applying the same gradient of opposite polarity. The propagator of motion, $P(\mathbf{z} \mid \mathbf{z'}, \Delta)$, gives the probability that a molecule at position z at time $t = 0$ will move to a new position z' at time $t = \Delta$. When the displacement is defined as $Z = z' - z$ and $q = (2\pi)^{-1}\gamma\delta g$ as its Fourier conjugate, the signal acquired is given by:

$$E(q) = \int P(Z,\Delta)\exp(i2\pi qZ)dZ \qquad 3.1$$

where $E(q)$ is the measured MR signal. From the form of equaion 3.1, one can easily see that a Fourier relationship exists between the signal $E(q)$ and the propagator $P(Z, \Delta)$ [2, 4]. For a system with a molecular self-diffusion of D and a coherent velocity v in the z direction, the propagator is a Gaussian function given by:

$$P(Z,\Delta) = \frac{1}{\sqrt{4\pi D\Delta}}\exp\left[\frac{-(Z-\bar{v}\Delta)^2}{4D\Delta}\right] \qquad 3.2$$

When this is plugged into equation 3.1, the Fourier transform of the signal is then:

$$E(q) = \exp(-4\pi^2 q^2 D\Delta + i2\pi q\bar{v}\Delta) \qquad 3.3$$

The random molecular motion of diffusion will cause an attenuation in the measured signal [12] and the coherent velocity will manifest as a change in phase [2, 4]. Additionally, the displacement experiment allows for both slow velocities, which may be present in the biofilm, and fast velocities representative of the bulk fluid flowing through the open channels in the porous media.

Measurement of Relaxation Using MR: Following the application of an excitation pulse, the hydrogen molecules will relax back to equilibrium on two different time scales. The first, spin-lattice or T_1 relaxation, is due to an exchange of energy with the surroundings (lattice) and relaxation occurs along the longitudinal axis [1, 2, 4]. The second form of relaxation is spin-spin relaxation, or T_2 relaxation, and occurs in the transverse plane due to molecular interactions [1, 2, 4]. T_2 relaxation depends on the rotational mobility of the protons and will be shorter for protons located in a pore or attached to a polymer chain. For example, T_2 for a proton with limited rotational

mobility could be of the order of microseconds to hundreds of milliseconds, compared to free hydrogens in a water sample, which have a T_2 on the order of seconds. Similarly, hydrogen exchange between restricted hydrogens and free hydrogens can also reduce the measured T_2 [88]. For instance, hydrogen present in water within the biofilm can exchange with the hydrogen on the biopolymer resulting in a shortened T_2, from approximately 2s in pure water to a reduced T_2 on the order of ms [31, 83, 84]. The correlation between both the dynamics and relaxation characteristics enabled the analysis of both the biofilm and bulk fluid phases separately but within the same experiment.

Materials and Methods

Biofilm Growth

Bacillus mojavensis was chosen for these experiments due to the ease with which it produces a relatively thick biofilm and its environmental importance [89]. Brain Heart Infusion (BHI, Becton, Dickenson and Company, Sparks, MD) was chosen as the growth media for the bacteria and prepared according to the recipe given by Mitchell et al [40 g L^{-1} NaCl, 3 g L^{-1} $NaNO_3$, 0.75 g L^{-1} NH_4Cl (Fisher, Pittsburgh, PA) and 36 g L^{-1} of BHI for 100% strength BHI] [89]. The recipe was reduced for each salt component and BHI to achieve strengths of 65%, 50%, 25% and 12.5% solution before being autoclaved. Following preparation and cooling of the media, 1 mL of a frozen stock culture of *Bacillus mojavensis* was warmed to room temperature and added to 100 mL of 100% strength BHI. This culture was incubated in a 250 mL media bottle (Kimax, Vineland, NJ) at room temperature on a horizontal shaker for 24 hours.

A model porous media was constructed with a 8.76 mm inner diameter chromatography column (Omnifit) that was packed with 240 μm diameter monodispersed polystyrene spheres (Duke Scientific). The flow loop was constructed using PTFE tubing and HPLC fittings (GE Scientific). The bead pack was saturated with distilled water and was monitored to ensure that there were no leaks or bubbles in the system before being loaded into the MR magnet. Once in the magnet, baseline experiments were performed with water before the fluid was switched to BHI. Additional baseline experiments were performed with BHI before the column was inoculated with *B. mojavensis*. All fluids were pumped at a rate of 50 mL/hr with an HPLC pump (Pharmacia P-500) to both create the proper pH and osmotic conditions for the bacterium *B. mojavensis* within the column.

After the bacteria grew sufficiently in the 250 mL media bottle on the shaker, 5 mL of this inoculum was injected into the bead pack and incubated without nutrient flow for four hours to allow for bacterial attachment to the beads. The flow of the growth media (BHI) was then re-started and continuously pumped up through the column at 50 mL hr^{-1} for the duration of the experiments. For the measured initial porosity of ϕ = 0.43, this flow rate gives an interstitial velocity $\langle v_0 \rangle$ = 0.53 mm/s. If the pore length is given by $l = \frac{d_p \phi}{1-\phi} = 180 \mu m$, where d_p = 240 μm is the diameter of the bead particles, then the Reynolds number for water in these experiments was $\mathrm{Re} = \frac{\langle v_0 \rangle l \rho}{\mu} = 9.6 \cdot 10^{-5}$. The Peclet number, the ratio of convective to diffusive transport, for this system is then

$\mathrm{Pe} = \frac{\langle v_0 \rangle l}{D_0} = 48$, which is greater than 1, indicating that convective transport is most likely a more significant mode of transport than diffusion [90].

The strength of the growth media provided for the bacteria affected the rate at which the biofilm grew. In four separate experiments, strengths of 65%, 50%, 25% and 12.5% BHI were administered. For the two strongest formulations of BHI (65% and 50%), the biofilm grew quickly, plugging the system and ultimately resulting in leaks after only 24 hours of data was obtained. The majority of the data presented here is for the 12.5% and 25% BHI solutions, where the biofilm was monitored without incident for 2 to 3 days.

Displacement-Relaxation Correlation Experiments

Two dimensional $P(Z, \Delta) - T_2$ displacement-relaxation correlation experiments were conducted as the biofilm was grown within the model porous media positioned in a 300 MHz Bruker super-wide bore superconducting magnet networked to an AVANCE III spectrometer. A Micro2.5 micro-imaging probe allowed for maximum gradients of 1.482 T m^{-1} in all three directions. The two dimensional $P(Z, \Delta) - T_2$ experiment begins with a PGStE sequence [2, 4] in the first dimension to encode the spins for displacement followed by a CPMG [9, 10] pulse train in the second dimension to measure the T_2 relaxation time. This pulse sequence is shown in Figure 3.1. To minimize the effects of exchange during the T_2 measurement [88], a τ value of 200 μs was used.

Initiation of most MR experiments begins with a 90□ excitation pulse that rotates the magnetization into the transverse plane where it can be detected. In the PGStE,

following the excitation pulse the first gradient of magnitude g is applied for duration of δ, encoding the protons for position. During the observation time Δ, when the protons relocate due to diffusion and flow, the magnetization is stored along the –z axis using a second 90□ pulse. This preserves the magnetization by minimizing the effects of transverse relaxation [2, 4]. After waiting for time t_2 a third 90□ RF pulse is applied, bringing the magnetization back into the transverse plane where it can be detected. The effect of the third RF pulse reverses the precession direction of the spins as it brings them

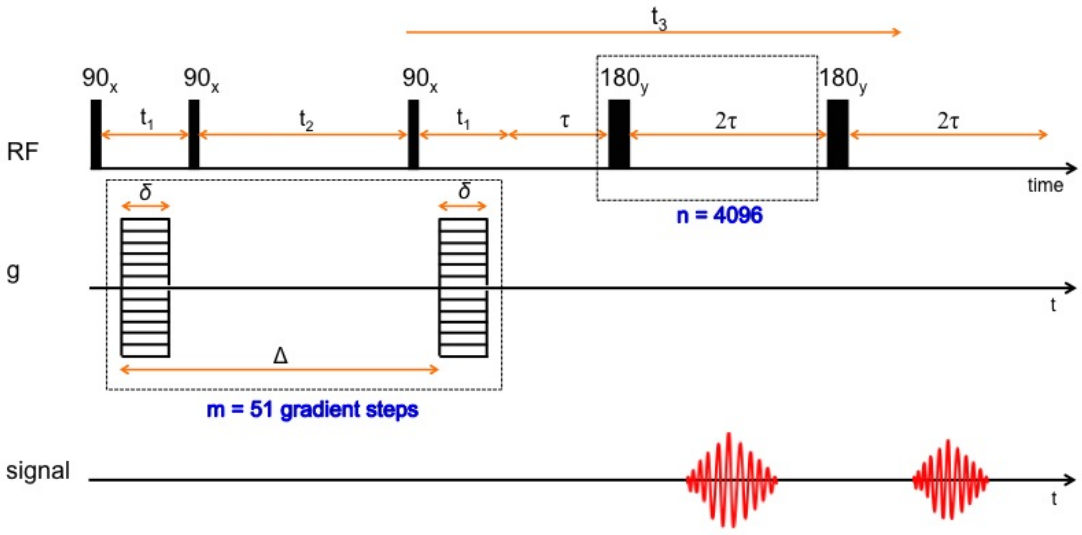

Figure 3.1. $P(Z, \Delta)$-T_2 displacement-relaxation correlation pulse sequence. A PGStE sequence encoded the spins for displacement followed by a CPMG sequence to measure T_2 relaxation. Important experimental parameters for the PGStE portion of the pulse sequence are: δ = 1 ms; Δ = 500 ms, 250 ms, or 50 ms; 51 linearly spaced gradient increments from -0.2964 T/m to 0.2964 T/m for Δ = 500 ms, -0.5928 T/m to 0.5928 T/m for Δ = 250 ms, and -1.482 T/m to 1.482 T/m for Δ = 50 ms; and for the CPMG portion of the pulse sequence: t_3 = from 0 to 1.64 s; τ = 200 μs and n = 4096 echoes collected.

back into the x-y plane, so that when the second gradient (of the same magnitude and duration as the first) is applied, it "decodes" the displacement of the protons. The

experimental details are given in the caption to Figure 3.1. The resulting 2D data set from each experiment included 51 gradient steps in the propagator dimension and 4096 echoes in the relaxation dimension. The data in the PGStE direction was Fourier transformed after zero filling to 64 points to obtain a propagator of motion for each echo that was collected. An inverse Laplace transform (ILT) was then performed for each propagator in the relaxation dimension to obtain the correlated T_2 time. Each experiment took 3 hours to complete in order to allow for signal averaging. As the biofilm grew within the magnet, experiments with observation times of Δ = 500 ms, 250 ms, and 50 ms were performed sequentially in that order, giving a total time of 9 hours to complete the set of propagator-relaxation experiments. Two dimensional relaxation-relaxation experiments were also performed in the set of experiments (not shown) bringing the total time for the entire suite of experiments to 12 hours. Biofilm growth was monitored from one to three days, depending on the strength of the growth media used and the corresponding extent of biofouling in the system.

Results and Discussion

Most of the data presented in this section was obtained from the biofilm grown at 12.5% strength BHI as it allowed for growth for three days without clogging the system or causing leaks. However, this data is representative of all the data collected. In Figure 3.2 results of the propagator – T_2 data are presented for observation times of Δ = 500 ms and Δ = 250 ms. The first column shows the baseline data collected for the growth medium BHI flowing through the system prior to inoculation with the bacteria. There is a slight shift to a lower T_2 of ~700 ms in the BHI compared to that of the baseline water

sample (not shown) which had a T_2 of ~1.2 ms. This is due to the presence of salts and hydrocarbon chains in the BHI. All of the BHI data exhibited this same trend with a consistent T_2 relaxation time of ~700 ms.

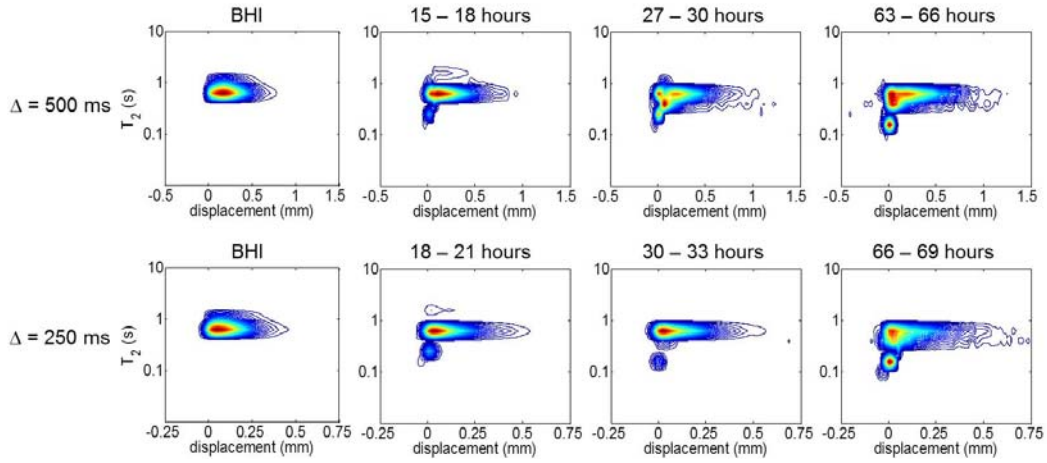

Figure 3.2. 2D $P(Z, \Delta) - T_2$ data for 12.5% BHI at two different observation times of Δ = 500 ms and Δ = 250 ms through the course of biofilm development from pre-inoculation (BHI) to approximately 3 days of growth. At 15 – 18 hours in the Δ = 500 ms data set and 18-21 hours in the Δ = 250 ms, a new population appears at a lower T_2 time of ~150 ms corresponding to biofilm growth. The peak occurs at a displacement of 0 mm and shows no convective flow. The population associated with the bulk fluid exhibits longer displacements as the biofilm grows, indicating that the biofilm is clogging pore space resulting in channeling and an increase in the velocity through these channels to maintain a constant volumetric flow rate.

At 15-18 hours in the Δ = 500 ms data set and 18-21 hours in the Δ = 250 ms data of Figure 3.2, a new population appears at a lower T_2 of ~150 ms and increases in intensity as time proceeds, corresponding to growth of the biofilm. This peak is centered on Z = 0 mm displacement and does not show any convective flow. The peak associated with the bulk fluid exhibits long displacements due to channeling that occurred as a result of biofilm growth. As the biofilm grew and plugged the pore space, velocity in the

channels had to increase to maintain the conservation of mass at the constant volumetric flow rate of 50 mL hr^{-1} of growth media, illustrated by the longer displacements.

In the Δ = 500 ms data, an intermittent third population appears in the 27-30 hour data set. This was likely due to a sloughing, or detachment event that occurred some time around 30 hours after inoculation, with the middle peak associated with the dislodged biofilm. Additional evidence for this can be drawn from the bulk fluid displacement information from this data set. After the sloughing event, the displacements are slightly shorter compared to those in columns two and four of the figure indicating that some pore space had cleared and the velocity through these channels was not as fast.

Sloughing events can also be seen in Figure 3.3. In this figure the integral of the intensity of the biofilm peak (displacement = 0 mm, $T_2 \sim$ 150 ms) for the two observation

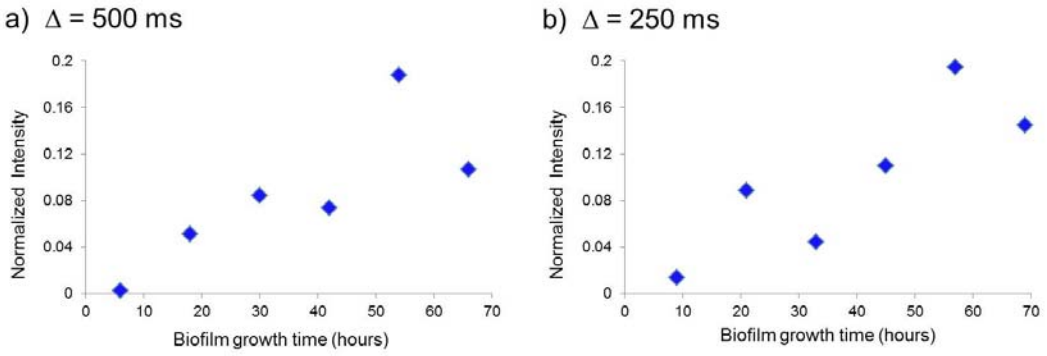

Figure 3.3. Integral of the intensity of the biofilm peak at a displacement of 0 mm and a T_2 of ~150 ms for a) an observation time of Δ = 500 ms and b) an observation time of Δ = 250 ms. The peak was integrated over the same area of each $P(Z, \Delta) - T_2$ plot and then normalized to the total signal intensity of each experiment. For both observation times, a decrease in signal occurred around 30 hours, indicating that a sloughing event most likely occurred. The biofilm signal intensity increases again following that event, indicating that the biofilm continued to grow until a second event occurred at about 60 hours. Each experiment took 3 hours to complete, and the Δ = 250 ms data was collected after the Δ = 500 ms. Therefore, the points for Δ = 250 ms data occur 3 hours after similar points for the Δ = 500 ms data.

times is displayed as the biofilm developed over the course of three days. Between 30 and 40 hours the intensity of the biofilm peak decreased, before increasing again until about 60 hours, when another event potentially occurred. This loss of signal corresponds

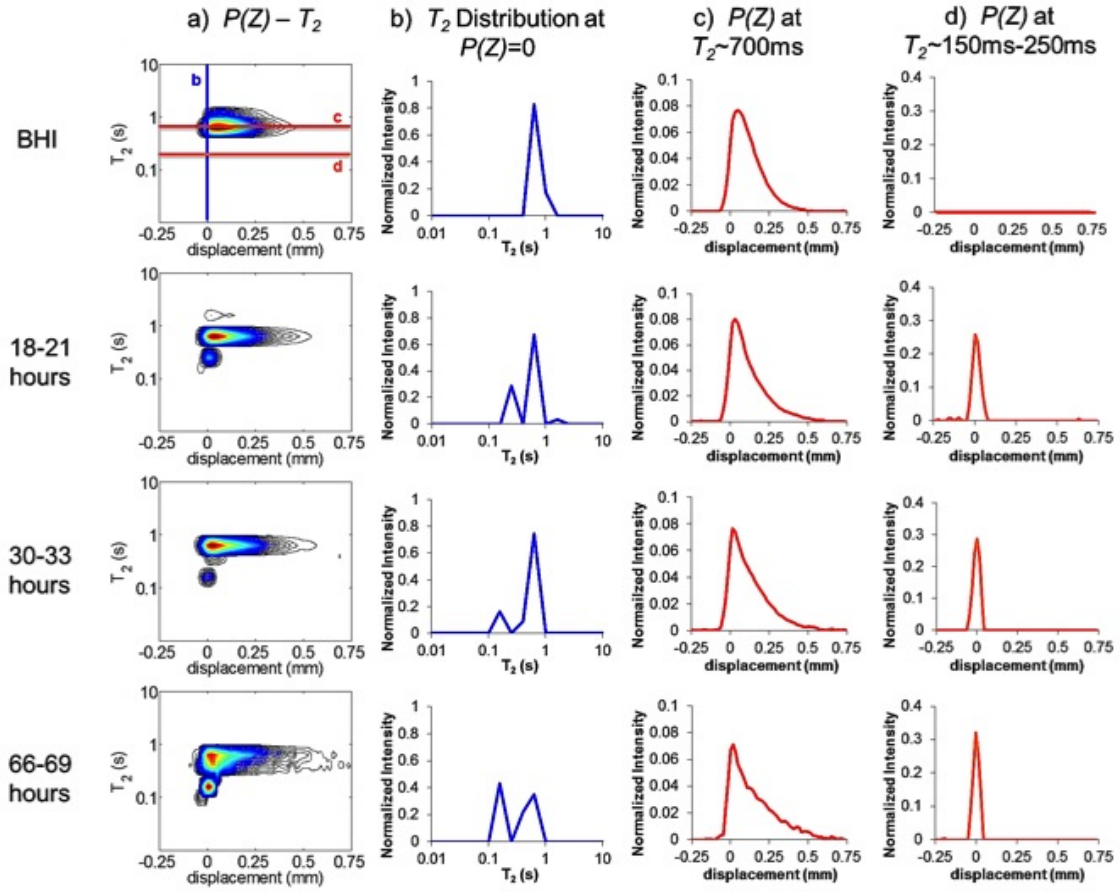

Figure 3.4. $P(Z, \Delta)$ and T_2 profiles analyzed at specific times during biofilm development for an observation time of $\Delta = 250$ ms. All data was normalized by the total signal acquired for each profile. a) $P(Z, \Delta) - T_2$ plots collected at four different times of biofilm growth. BHI data was collected before the bacteria was introduced into the model porous media. b) T_2 profile at zero displacement ($Z = 0$ mm) shows biofilm (the left peak) growth and decay over time. c) $P(Z, \Delta)$ profile for the bulk fluid at T_2 ~700 ms, illustrating that the bulk fluid shows longer displacement times to compensate for the clogging of pore space due to biofilm growth. d) $P(Z, \Delta)$ profile for the biomass peak at T_2 ~150ms showing that there is no convective flow through the biomass.

to a reduction in the amount of biomass at this displacement ($Z = 0$ mm) and relaxation time (T_2 ~150 ms). While the experiment times were too long to accurately determine exactly when the sloughing events occurred, there was clearly a transition at approximately 30 and 60 hours. Other events could have taken place between these times as well, but was not captured in the data we acquired.

Figure 3.4 shows a more detailed analysis of the dynamics occurring at zero displacement ($Z = 0$ mm) by observing the change in the T_2 distribution, as well as displaying the displacement data for the bulk fluid at a T_2 of ~700 ms and the biomass at a T_2 of ~150 ms. Figure 3.4 b) presents the T_2 profile for a displacement of $Z = 0$ mm. The emergence of the left peak corresponds to biofilm growth. Similar to Figures 3.2 and 3.3 the sloughing event that occurred around the 30-hour time frame is seen in this figure by a slight decrease in the left peak from the T_2 profile at 18-21 hours compared to that at 30-33 hours. This peak then grows again with an approximately equal amount of signal from the biofilm and bulk fluid at 66-69 hours.

In columns c) and d) of Figure 3.4 the propagator profile is displayed for the bulk fluid and the biofilm, respectively. For the bulk fluid a distribution of displacements is seen in all four profiles consistent with convective fluid flow. However, a larger distribution is seen after the growth of biofilm in the bead pack (the last three plots in the third column of the figure). This is indicative of channeling, where the bulk fluid cannot flow through bioclogged pores and must flow faster through the interstitial space to maintain the constant flow rate. In contrast to this, the propagator profile for the biofilm peak shows no distribution of displacements and is centered on $Z = 0$ mm. This clearly

indicates that there is no convective flow through the biofilm within the displacement resolution of the experiments, +/- 15.6 μm over Δ = 250 ms, which corresponds to a velocity of +/- 62 μm s^{-1}.

Figure 3.5 presents the T_2 distributions for $P(Z, \Delta) = 0$ at an observation time of Δ = 250 ms for the four different concentrations of BHI collected after 21 hours of biofilm growth. Again, the intensity of each plot was normalized by the total intensity for each

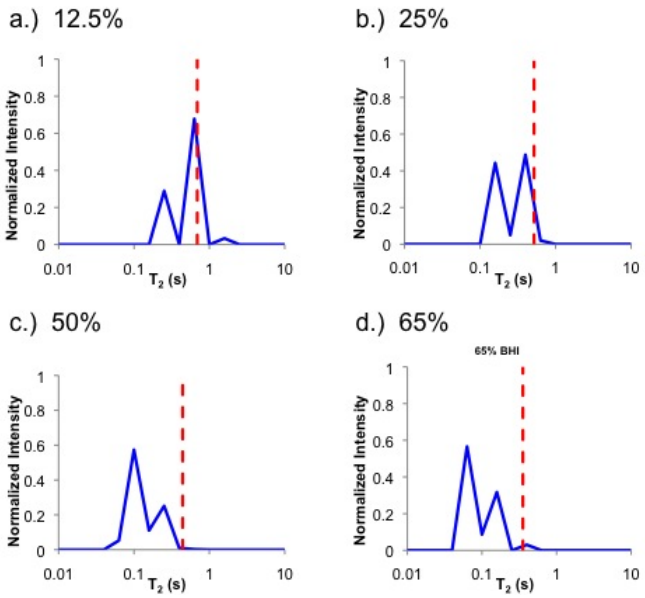

Figure 3.5. T_2 distributions at $P(Z, \Delta) = 0$ for Δ = 250 ms following 21 hours of growth for four different strengths of BHI, the growth media. The dotted line in each plot indicates the T_2 relaxation time of the BHI before the bacteria was introduced into the bead pack. a) At a concentration of 12.5% BHI, the initial value of T_2 for BHI was 690 ms. b) The 25% solution of BHI had a T_2 of 520 ms. c) For the 50% concentration BHI the initial T_2 was 440 ms. d) The T_2 of the 65% solution was 350 ms. This trend to a shorter T_2 with increasing concentration is due to a higher concentration of salts and carbon sources in the BHI.

data set. The dotted line in each plot corresponds to the T_2 of the BHI growth media before any bacteria was introduced into the bead pack, with T_2 = 690, 520, 440 and 350

ms for 12.5%, 25%, 50% and 65% solution of BHI, respectively. The trend of shorter T_2 relaxation times for increasing BHI strengths is due to greater concentrations of salts and carbon sources in the higher strengths of BHI. Like Figure 3.4 b), the left peak in these plots coincides with biofilm growth. From the increase in the intensity of the biofilm peak coupled with a decrease in the bulk fluid peak for increasing strengths of BHI, it is clear that a greater supply of nutrients causes the bacteria within the biofilm to grow at an elevated rate. The shift to shorter T_2 times for the biofilm peak with increased growth also indicates that the bacteria are producing a thicker polymer matrix. This thicker EPS leads to greater hydrogen exchange between the water protons present in the biofilm and the protons on the biopolymer and thus shorter T_2 relaxation, a marker for the extent of biofouling.

Conclusion

In the research presented here, the use of two-dimensional MR displacement-relaxation correlation experiments enabled the analysis of the displacement dynamics and relaxation characteristics of both the biofilm and bulk fluid phases within the same experiment. Much information can be gleaned from the same experimental data set, including biofilm growth, the analysis of fluid flow in the separate phases, and potentially the degree of biofouling. These experiments supported evidence that there is no convective flow through the biomass, but that convection is present in the channels and interstitial spaces surrounding the biomass. Evidence of biofilm detachment events was also presented in this work.

CHAPTER FOUR

BIOFILM DETECTION IN NATURAL UNCONSOLIDATED POROUS MEDIA USING A LOW-FIELD MAGNETIC RESONANCE SYSTEM

Contribution of Authors and Co-Authors

Manuscripts in Chapters 3 and 4

Author: Alexis Sanderlin

Contributions: Helped conceive and implement the study design. Helped collect and analyze data. Wrote manuscript.

Co-Author: Sarah J. Vogt

Contributions: Helped conceive and implement the study design. Helped collect and analyze data. Provided feedback and comments on the manuscript.

Co-Author: Elliot Grunewald

Contributions: Helped conceive the study design. Provided feedback and comments on the manuscript.

Co-Author: Bridget A. Bergin

Contributions: Helped implement the study design. Provided feedback and comments on the manuscript.

Co-Author: Sarah L. Codd

Contributions: Helped conceive and implement the study design. Provided feedback and comments on the manuscript.

Manuscript Information Page

Alexis B. Sanderlin, Sarah J. Vogt, Elliot Grunewald, Bridget A. Bergin, Sarah L. Codd
Environmental Science & Technology
Status of Manuscript: (Put an x in one of the options below)
____ Prepared for submission to a peer-reviewed journal
____ Officially submitted to a peer-review journal
____ Accepted by a peer-reviewed journal
_X_ Published in a peer-reviewed journal

American Chemical Society
Vol. 47, No. 2, Pages 987-992, January 2013

BIOFILM DETECTION IN NATURAL UNCONSOLIDATED POROUS MEDIA USING A LOW-FIELD MAGNETIC RESONANCE SYSTEM

Abstract

The extent to which T_2 relaxation measurements can be used to determine biofouling in several natural geological sand media using a low-field (275 kHz, 6.5 mT) NMR system has been demonstrated. It has been previously shown that at high laboratory strength fields (300 MHz, 7 T), T_2 techniques can be used as a bioassay to confirm the growth of biofilm inside opaque porous media with low magnetic susceptibilities such as borosilicate or soda lime glass beads. Additionally decreases in T_2 can be associated with intact biofilm as opposed to degraded biofilm material. However, in natural geological media, the strong susceptibility gradients generated at high fields dominated the T_2 relaxation time distributions and biofilm growth could not be reliably detected. Samples studied included *Bacillus mojavensis* biofilm in several sand types, as well as alginate solution and alginate gel in several sand types. One of the sand types was highly magnetic. Data was collected with a low-field (275kHz, 6.5 mT) benchtop NMR system using a CPMG sequence with an echo time of 1.25 ms, providing the ability to detect signals with T_2 greater than 1 ms. Data presented here clearly demonstrate that biofilm can be reliably detected and monitored in highly magnetically susceptible geological samples using a low-field NMR spectrometer, indicating that low-field NMR could be viable as a biofilm sensor at bioremedation sites.

Introduction

Bioremediation, the use of bacteria to remove or contain pollutants and waste in the subsurface, is being used as a means to control contaminants in the environment [91-95]. However, the monitoring of bacterial growth comes with several challenges. Direct sampling, the method most often used to determine the efficacy of the bioremediation process, provides little spatial information, can be quite costly and potentially alters the environment it is intended to measure. Additionally, the samples collected from contaminated sites pose significant safety, regulatory and cost issues. Nuclear magnetic resonance, NMR, has been proposed as an effective means to non-destructively monitor biofouling on-site in the subsurface [31, 84].

Hydrodynamics and mass transport inside biofouled porous media has long been of interest due to its broad importance not only in bioremediation, but also in nature, industry, and medicine [96]. Since the early 1990s, researchers have used a variety of porous systems in the lab (e.g. sand, glass bead packs, rocks and flat plate channel reactors) to measure how the extracellular polymeric substance (EPS) production from bacterial cells changes a system's hydraulic conductivity, mass transport, and dynamic flow patterns [84, 92, 97]. Some of these lab techniques have also been applied in large bioremediation field scale studies to determine biofilm impact and presence [98]. Using high magnetic field NMR to study how biofouling affects transport in porous media is a relatively new application [31, 84, 85, 99-101]. High-field NMR imaging has been used to spatially resolve biofouled porous systems, monitor flow changes in biofouled bead packs and detect the extent of biofouling in bead packs [84, 100, 102, 103]. However, no

previous studies have successfully applied NMR to study biofilms in natural porous media, even in the lab.

This paper presents the first use of low-field NMR to study biofilms in porous media and indicates it may be a viable technique for monitoring biofilm growth at bioremediation sites. It has been previously shown that laboratory high-field NMR measurements can clearly be used as a bioassy to confirm the presence of biofouling in model porous media and obtain complementary and unique information about biofilms, but so far the challenge of dealing with high magnetic susceptibility gradients has limited the application in natural porous media [31]. Specifically, the extent of biofouling in natural geological materials cannot be determined using high-field NMR due to the strong susceptibility gradients produced by the magnetic materials present in geological samples [31]. These susceptibilities dominate the T_2 distributions, hindering the detection of biofouling. These magnetic field gradients in natural sediments and rocks are due to the presence of magnetically susceptible minerals (such as iron-bearing minerals) within the grains or on the grain surfaces. The presence of magnetic minerals causes local variations of magnetic flux in an otherwise uniform static magnetic field, and generates spatial gradients in the static field on a very small scale. These gradients cause an irreversible loss of coherence of the NMR signal, and hence a more rapid decay of the detected signal due to diffusion (random movement) of water molecules in the gradient fields [104]. In natural rocks and sediments, these effects associated with magnetic gradients dominate the relaxation response, overwhelming the biofilm signature. To enable the sensitivity of the NMR measurement to the biofouling processes of interest, it

is therefore critical to reduce the effect of magnetic susceptibility. The magnitude of magnetic susceptibility gradients generally scales linearly with the intensity of the applied static field [2]. Although lowering the static magnetic field is the easiest way to reduce susceptibility gradients, the measured NMR signal also decreases with static magnetic field strength. Nonetheless, the measurements presented here indicate low-field NMR techniques can reliably detect biofouling in porous materials even with strong magnetic components, establishing the method as a potential *in situ* subsurface biosensor.

A low-field (6.5mT, 275 kHz) benchtop NMR system with an open bore was used in this study to ascertain the extent to which T_2 relaxation measurements can be used to measure biofouling in several natural geological sand media. This low-field spectrometer is approximately 3 orders of magnitude lower than the 2-7 Tesla (85-300 MHz) NMR spectrometers that have typically been used to characterize NMR properties of biofilms in porous media [31, 84, 85, 100, 101]. In this study a *Bacillus mojavensis* biofilm was grown in a large silica sand column. A range of samples intended to determine the ability of low-field NMR to sense biofilms were then constructed using biofilm, alginate solution and alginate gels in model and natural sands (natural unconsolidated porous media). Data presented here clearly demonstrate that biofilm can be reliably detected and monitored in high magnetic content geological samples using a low-field NMR spectrometer. Such samples cannot even be safely placed in a high magnetic field due to the forces on the material. This result is significant in that it paves the way for NMR biofilm sensors using low-field systems to be extended to the field scale.

Theory

Biofilm Formation

Biofilms form when bacterial cells adhere to a surface and begin to excrete biopolymers such as proteins, DNA and carbohydrates that form a protective matrix collectively referred to as extracellular polymeric substance (EPS), an often slimy appearing layer encasing the bacterial cells [30, 68]. Variation in the nature of the EPS layer leads to biofilm thicknesses that vary from a few to several hundred microns, depending on the microbial composition [105]. Biofilms are predominant in a range of settings such as the surfaces of teeth, the walls of water treatment equipment, industrial pipes, ship hulls, and human implant surfaces [106]. They are also found in the subsurface where complex ecosystems of microbial species co-exist and can help or hinder processes such as oil recovery and bioremediation [89, 93]. Biological activity can interact with the geochemistry precipitation of contaminants, whilst the presence of EPS can impact the flow dynamics of subsurface liquids [107]. The recovery of oil from or the remediation of contaminants within porous earth formations can be strongly impacted by bioactivity, as the subsurface porous media is in essence a large packed bed bioreactor [93, 95, 108].

T_2 Relaxation

When a sample containing nuclei that are detectible using magnetic resonance (^{1}H, ^{13}C, ^{31}P for example) is placed in an external magnetic field B_0, the spins will align either parallel or anti-parallel with this applied field. A slightly greater population of spins aligning parallel with the field results in a bulk magnetization M_0 along the same

direction as the applied field. Magnetization parallel to the applied field cannot be detected and must be disturbed from this position. Energy in the form of a radio frequency pulse (RF) is applied at the Larmor frequency, $\omega_0 = \gamma B_0$, where γ is the nuclei-dependent gyromagnetic ratio. The signal will then relax back to equilibrium on two different time scales, T_1 or spin-lattice relaxation and T_2 or spin-spin relaxation. T_2 relaxation, which was measured in the experiments presented here, is due to molecular interactions.

Factors such as inhomogeneous magnetic fields, diffusion, and surface interactions that occur on a time scale longer than hundreds of microseconds cause inhomogeneous dephasing of the spins, and hence shorter T_2 relaxation. Rephasing, or refocusing, the spins can correct for some of these effects on T_2 relaxation. Applying a 180-degree pulse at a time τ after the initial 90-degree excitation pulse will result in a refocused, or rephased signal called a spin echo occurring at a time 2τ, the echo time, from the 90-degree pulse. Molecular interactions occurring on a time scale shorter than the echo time, such as surface interactions, cannot be refocused resulting in an irreversible loss of signal and a shortened T_2 relaxation time. Repetition of n 180 degree pulses spaced every 2τ results in the amplitude of the echoes $M(2n\tau)$ decaying as:

$$M(2n\tau) = \sum_{T_2} M_0(T_2) \exp\left(\frac{-2n\tau}{T_2}\right) \qquad 4.1$$

where $M_0(T_2)$ is the distribution of the T_2 relaxation times due to the physical and chemical environment of the spins in the sample with each T_2 relaxation value. This series of 180 degree pulses is known as the Carr, Purcell, Meiboom and Gill (CPMG)

sequence [9]. By then applying an inverse Laplace transform to the detected signal, the T_2 relaxation time distribution of spins $M_0(T_2)$ within the sample is obtained [109].

Spin-spin T_2 magnetic relaxation provides information on the rotational mobility of the protons on water molecules. In regions where exchangeable protons are present, such as those on the -OH groups of biopolymers, fast proton-proton exchange between the protons on water molecules and the protons on the biopolymers can reduce the measured T_2 relative to a measurement made in pure water. Specifically, in regions where biofouling is present, proton-proton exchange between the protons on water molecules and the protons on the cross linked biopolymers in the EPS results in a reduced T_2 time relative to a measurement made when the water is only in the presence of the freely diffusing molecules in the growth media [110].

Low-Field Magnetic Resonance

Advances in laboratory NMR spectrometers and the associated measurement techniques have typically exploited the fact that NMR signal increases as the magnetic field is made stronger and more homogeneous. Hence, many chemistry and physics laboratories house spectrometers which operate at 300-700 MHz due to the stable superconducting magnets that produce fields of 7-17 T. However, these strong magnetic fields are not suitable for samples that are extremely heterogeneous and/or made of materials with significant magnetic susceptibility, including common geologic media containing magnetic minerals. For this reason, oil companies' down-the-borehole spectrometers that use NMR in the subsurface operate at 2 MHz (50 mT). These down-the-borehole spectrometers use "inside out" electronics relative to laboratory NMR. The

electronics are on the inside of a cylindrical 5-inch diameter tool, and the NMR measurement is obtained from the region of the subsurface surrounding the tool.

Vista Clara, Inc. (Mukilteo, WA, USA), has developed a down-the-borehole tool that is designed to operate in the smaller 2-inch diameter, cased wells that are commonly used for groundwater monitoring [111]. The tool operates at a lower frequency of ~275 kHz (6.5 mT) in order to detect signal from a larger surrounding region of the subsurface. The results presented here provide benchmarking data to demonstrate that a down-the-borehole tool operating at these low frequencies can potentially detect and monitor changes in the extent of biofouling in the subsurface with NMR relaxation measurements.

Materials and Methods

Reactor Design

The reactor was constructed of schedule 40 clear polyvinyl chloride (PVC) piping having an inside diameter of 5.08 cm and 38.1 cm length. Two column reactors are shown in Figure 4.1. To prepare the reactor for the experiments, the column was wet-packed with silica sand (Unimin Corp 4095) and disinfected.

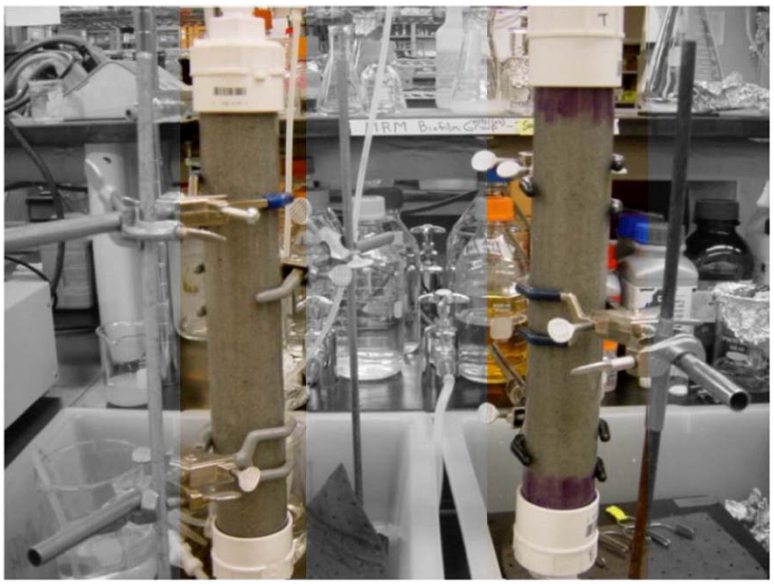

Figure 4.1. Silica sand column reactors used to grow biofilm. The purple color on the column on the right is glue used to seal the outside of the reactor.

Bacillus mojavensis, which forms a thick biofilm, was chosen due to its importance in bioremediation [89]. Brain Heart Infusion [Becton, Dickinson and Company], or BHI, the broth used as the bacterial growth medium, was prepared according to the recipe of Mitchell et al [89]. After inoculation with *B. mojavensis*, BHI was pumped upwards through the reactor in a flow-through system at 500 mL hr^{-1} in approximately 2 to 8 hour pulses for 10 days. The volumetric flow rate of 500 mL hr^{-1} corresponded to a maximum velocity of approximately 0.17 mm s^{-1} through the reactor, assuming a porosity of 0.4 for the sand. Throughout the growth process, a pressure gauge located at the entrance of the reactor was monitored. After observing a large pressure increase at the reactor inlet, the flow system was disassembled and the samples prepared for NMR analysis. Sand samples were collected from both the bottom (column entrance) and top (column exit) of the reactor. It was evident that biofouling primarily occurred at

the entrance to the reactor, see Figure 4.2. The sample from the entrance of the reactor where the BHI was being pumped into the reactor was completely biofouled, exhibiting a gelatinous consistency and cloudy color (Figure 4.2a.). In contrast, the sample from the exit of the reactor showed no signs of biofouling and the sand displayed characteristics similar to wet beach sand (Figure 4.2b.).

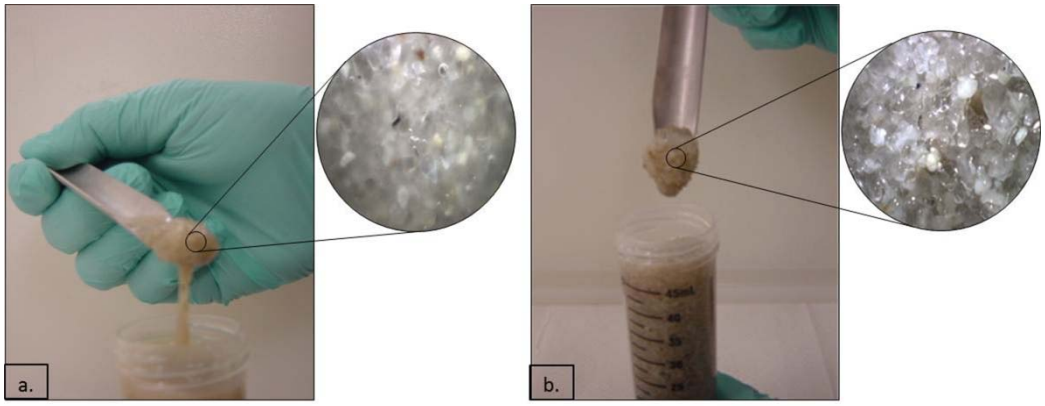

Figure 4.2. Sand samples from (a) the entrance (biofouled) of the reactor and (b) from the exit (not biofouled) of the reactor. The biofouling clearly occurred at the entrance of the reactor.

In addition to the biofilm growth in the silica sand column, biofilm mixed with samples of sand taken from the Hanford Buried Waste Test Facility in Richland, Washington were also analyzed. The Hanford site sand was less homogeneous in size than the silica sand and contained significant iron impurities. The silica sand and Hanford sand represented the two extremes of geological media with regard to magnetic content.

Sand Analysis

The silica sand used in the column reactor had the following grain size distribution: 28.5% > 840 um diameter, 38.1% between 595 um and 840 um, 32.2% between 354 um and 595 um, 1.2% < 354 um diameter. A neodymiun magnet was not able to move any of the silica sand. Mixing the silica sand with HCl did not produce any bubbles indicating there were no calcium ions present.

The Hanford sand had the following grain size distribution: 11.8% > 840 um diameter, 13.4% between 595 um and 840 um, 42.3% between 354 um and 595 um, 17.2% between 177 um and 354 um, 9.0% between 100 um and 177 um diameter, 5.3% between 50 um and 100 um diameter, 1% < 50 um diameter. A neodymium magnet was able to pick up and move 65% of the sand, demonstrating how strongly magnetic this sand was. Mixing the Hanford sand with a 0.1 M HCl solution did not produce any bubbles; however mixing with a 1.0 M HCl solution did, indicating the presence of calcium ions.

Alginate Preparation

Biofilms are primarily composed of a matrix of bacterially produced polymers and proteins known as the extracellular polymeric substance (EPS) [30]. Alginate is a biopolymer isolated from both brown algae and from certain types of bacterial biofilms [112, 113]. Alginate solutions and gels are often used as model systems for biofilms [114], so they were also analyzed to study the contribution to the T_2 relaxation caused by the mobility of the alginate biopolymer molecules in the solution or gel phase [115].

Algal alginate [Acros Organic] solutions were prepared at 2wt%, 1wt% and 0.5wt% alginate in distilled water in 5.7 cm diameter, clear plastic bottles. The solutions were then gelled using a diffusion reaction mechanism by adding a solution of 0.5M $CaCl_2$ on top of the alginate solution. After gelation, the water around the gel was drained and replaced by fresh alginate solution. This procedure was followed in order to analyze the difference between solution and gel at the same solution concentration of polymer. Mixtures of 1wt% alginate solution and the two different types of sand, silica and Hanford, were also prepared and then gelled using the same procedure.

Prior to mixing the Hanford sample with alginate, the sample bottle was wet-packed with an appropriate amount of Hanford sand to completely fill the bottle. The sand was removed from the bottle and mixed with the alginate solution. After combining the sand and alginate solution, only 74% of the original mass of sand could be re-packed in the bottle due to partial gelation of alginate and related increased viscosity, resulting in a less densely packed sample compared to the clean Hanford sand. The presence of the calcium ions and the 1% of particles less than 50 μm contributed to this observed partial gelation.

NMR Measurements

NMR measurements for all samples were acquired using the portable benchtop Corona system [Vista Clara, Inc.], with an operating frequency of ~275 kHz. For all experiments the ^1H nuclei were excited. The geometry of the magnets produced a field that was uniform over a spheroidal volume that had an average dimension of 5 cm. Each sample was placed in the same location in the instrument for accurate and comparable

measurements. Placement was checked by the reproducibility of the measurement for a standard water sample. A CPMG measurement sequence was used to assess the T_2 relaxation behavior of the samples. For each experiment, a repetition time of 10 seconds, excitation pulse length of 100 μs, echo spacing of 1.25 ms, 800 echoes, and 300 averages was selected.

For comparison of data from a high-field magnetic system, some of the same samples were also analyzed in a Bruker Avance 300 MHz vertical magnet spectrometer. The Hanford sand samples contained materials that were highly magnetic and therefore could not be placed in the strong magnetic field. The silica sand and alginate solutions and gels were measured using the same NMR parameters as were used on the low-field system, but with 64 averages. All of the data was processed using inverse Laplace transform ILT software developed in Matlab (MathWorks, Inc.).

Results and Conclusions

Silica Sand with Biofilm

In Figure 4.3, we show T_2 relaxation-time distributions for the low-field NMR measurements on the sand column reactor. The biofouled silica sand exhibited a T_2 time of approximately half that of the non-biofouled sand, 450 ms versus 900 ms. We attributed the shorter relaxation time of the biofouled sand to proton-proton exchange with the biopolymers present in the biofilm EPS.

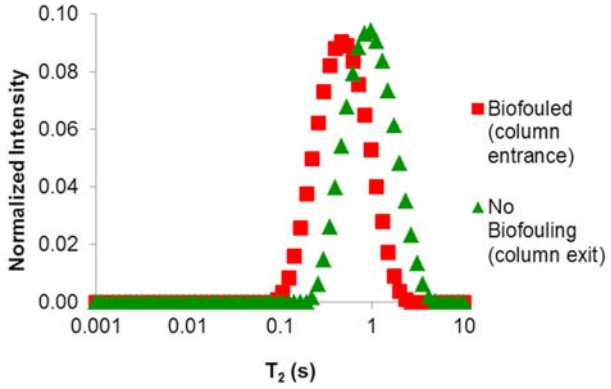

Figure 4.3. **Silica Sand, Low Field.** T_2 relaxation time distributions from the low-field NMR system showing a clear distinction between the biofouled and non-biofouled sand.

Both sand samples were also tested in the high-field (300 MHz) NMR system, producing analogous results as with the low-field system. Figure 4.4 shows that the biofouled silica sand sample had a lower T_2 relaxation time than the non-biofouled sample, similar to the findings in Figure 4.3. The relaxation time in Figure 4.4 was lower for both samples due to the increased impacts of magnetic field susceptibility at high

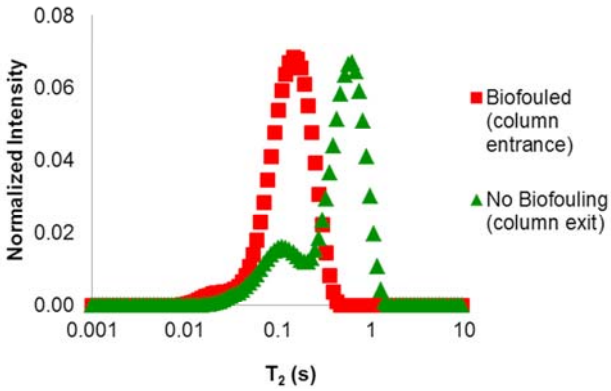

Figure 4.4. **Silica Sand, High Field.** T_2 relaxation time distributions from the high-field NMR system showing a similar distinction between the biofouled and non-biofouled sand as seen above in Figure 4.3. The appearance of a second shorter T_2 was due to the magnetic field gradients induced at the edges of the pores in the high-field.

magnetic fields. The silica sand had low enough magnetic susceptibility that biofouling could be measured by NMR at high magnetic fields, as seen in Figure 4.4.

Hanford Sand with Biofilm

Biofouled silica sand was mixed with Hanford site sand in a 50:50 ratio to prepare samples that had biofilm and a high magnetic susceptibility material. Figure 4.5 shows that even in the presence of very high magnetic susceptibility sand, the changes in T_f due to the biofilm polymer were significant and easily detectable at 275 kHz.

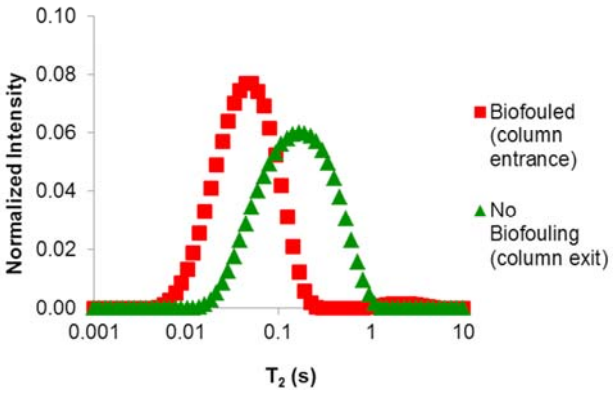

Figure 4.5. **Silica Sand mixed with Hanford Sand, Low Field**. T_2 relaxation time distributions from the low-field NMR system showing a difference between the biofouled and non-biofouled silica and Hanford site mixed sand samples.

Alginate Gels and Sand with Alginate Solutions

The T_2 relaxation time distributions for alginate gel and the surrounding alginate solution for two different concentrations of alginate are shown in Figure 4.6. As the calcium ions formed a physical gel, the proton-proton exchange between the water molecules and the more rigid polymers of the gel resulted in the lower T_2 relaxation time. The samples contained both gelled alginate and alginate solution, which exhibited distinct

T_2 times. The T_2 of the ungelled alginate solution was approximately 1 s in both samples (compared to a T_2 of 2 s for distilled water). After gelation, however, both concentrations showed the gel having a T_2 below 100 ms, with the 2wt% alginate gel exhibiting a shorter T_2 than 0.5wt% alginate gel. A higher percentage of alginate produced a stiffer gel and provided additional proton exchange sites on the more rigid alginate polymers, resulting in a lower T_2.

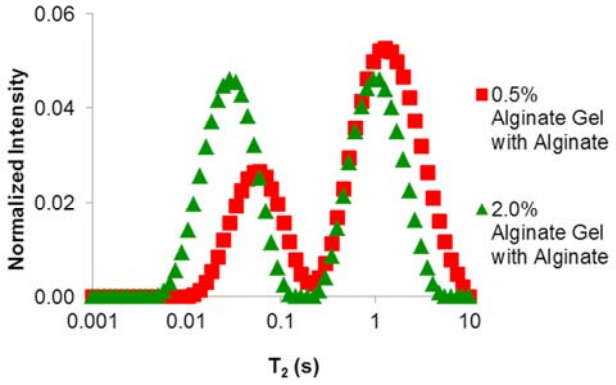

Figure 4.6. **Alginate Gel, Low Field**. T_2 relaxation time distributions of the different alginate gel concentrations. Each sample contained the gelled alginate and alginate solution. For each sample the longer T_2 resulted from the presence of the alginate solution and the shorter T_2 from the gel. The alginate solution surrounding the gel gave a peak at about 1 s, which was the same as the solution prior to the gelling.

Figure 4.7 shows the T_2 relaxation time distribution for silica sand with pure water, sand mixed with 1wt% alginate and sand with 1wt% alginate after gelation. The T_2 of the sand with pure water was similar to the T_2 of the sand mixed with alginate solution. After gelation, the T_2 shifted down to approximately 100 ms. The T_2 relaxation times in the clean silica sand and silica sand with alginate gel at low-field were similar to the findings of the same sand with and without biofouling shown above in Figure 4.3. As the alginate gelled, the alginate biopolymer molecules became less mobile and the T_2

relaxation time shortened, similar to water interaction with the biofilm EPS. The data clearly demonstrated that it was the hydrogel phase of the biofilm which generated variation in the T_2 relaxation time distribution shown in Figure 4.3.

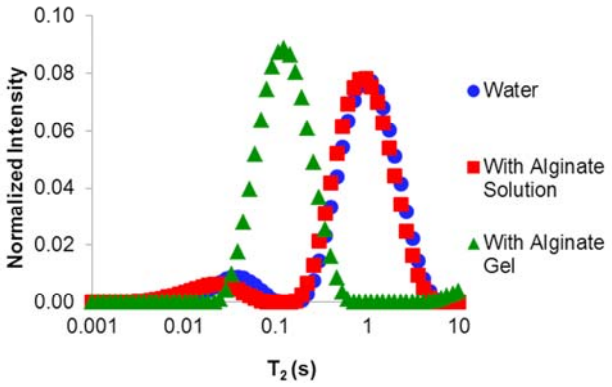

Figure 4.7. **Alginate in Silica Sand, Low Field.** T_2 relaxation time distributions of the silica sand samples using the low-field NMR system. The sand with pure water and sand with alginate solution exhibited very similar T_2 relaxation times of approximately 1 s. However, after gelation, the T_2 got shorter, 100 ms. This shorter T_2 was due to the proton-proton exchange of the water with the less mobile hydrogen of the biopolymer, and was very similar to the interaction between the water and EPS of the biofilm seen in Figure 4.3.

The T_2 relaxation time distributions of the 1wt% alginate solution and gel mixed with the Hanford sand as measured in the low-field NMR system are shown in Figure 4.8. Both the Hanford sand mixed with the alginate solution and alginate gel exhibited lower relaxation times than the clean Hanford sand, with again the shortest T_2 exhibited after gelation. The significantly lower T_2 for the clean sample of Hanford sand (T_2~100 ms) compared to the T_2 in the clean silica sand (T_2~1000 ms, Figure 4.7) was indicative of significant iron content in the natural Hanford sample. It is interesting to observe that the T_2 for the alginate solution in the Hanford sand (T_2~30 ms) was very different from the T_2 of water in the Hanford sand (T_2~100 ms). This result contrasted with that

presented in Figure 4.7 for silica sand in which the T_2 did not vary significantly between water and alginate solution in the silica sand. This difference was due to the presence of fine particulates in the Hanford sand that alter the polyelectrolyte alginate biopolymer conformations and interactions, and caused partial gelation of the alginate solution. Additional evidence of the partial gelation of the alginate solution was provided when packing the sand into the sample bottle. The partial gelation of the alginate in the Hanford sand sample as described in the methods sectrion resulted in a lower T_2 compared to the clean Hanford sand. This indicated the ability of the NMR T_2 measurements to monitor not only biological activity and biofilm growth, but also the interaction of biological activity and geochemistry.

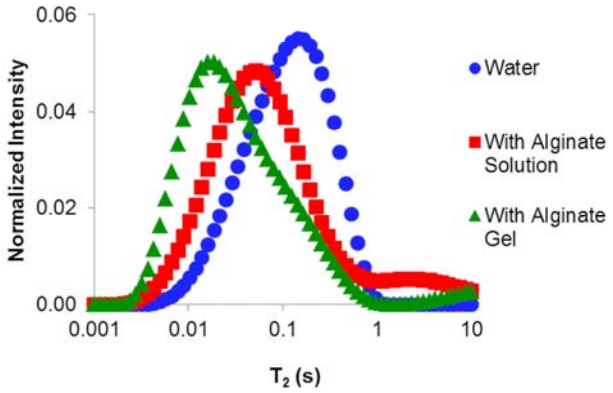

Figure 4.8. **Alginate in Hanford Sand, Low Field.** T_2 relaxation time distributions of the Hanford sand samples using the low-field NMR system. Due to the presence of iron in the Hanford sand sample, the T_2 of the sand with pure water sample was lower (T_2~100 ms) than that of the clean silica sand (T_2~1000 ms). The Hanford sand also had charged mineral species that interacted with and changed the biopolymer conformations, which was exhibited by the sand with alginate solution having a lower T_2 than the sand with pure water sample. This was in contrast to the silica sand, which has similar T_2 times for both the sand with pure water and sand with alginate solution.

The ability of NMR T_2 relaxation time distribution measurements to detect biofilm presence as a marker of biological activity in natural geological media has been demonstrated at low magnetic fields. Due to the use in down-the-borehole spectrometers and limitations of high field characterization of magnetic materials, low-field NMR is relevant to the development of *in situ* subsurface NMR sensors. In comparing measurements of alginate solutions in a model silica sand and in a naturally occurring (and highly magnetic) sand from the Hanford site, the impact of the interaction between biopolymers and geochemistry indicate that the mineral content of the geological media significantly impacts the T_2 relaxation time distributions. These results demonstrate a significant potential for NMR relaxation measurements to monitor bioactivity and further characterize bio-geochemical interactions in the subsurface. A single T_2 measurement alone will not be a direct indication of the presence of biofilm. However, an NMR sensor could be placed in the subsurface and used to monitor the growth and decay of biofouling over the duration of a bioremediation process.

CHAPTER FIVE

RHEO-NMR AND NON-NEWTONIAN FLUIDS

Introduction

The research presented in this chapter involves both rheology and nuclear magnetic resonance. An introduction to rheology will be presented as well as a description of the types of fluids studied in this research.

Rheology

Derived from the Greek word *rheos* which means "anything flowing" [116], rheology is the study of the flow and deformation of a material. Rheology is not only concerned with the mechanical properties of a fluid under flow conditions, but can also be used to determine the strength of the particle bonds when a fluid is at rest [116]. Understanding the behavior of materials subjected to mechanical deformation is important in many industries especially in the production and use of polymers [117-121], but also the seemingly unrelated food processing industry [122-125].

In the simplest form, the mechanical properties of a material will lend to the categorization of either a solid with elastic behavior, or a liquid with viscous characteristics. A solid will deform when subjected to a stress and store the energy elastically, while a liquid will flow, dissipating the energy in viscous losses [126]. However, some materials have both solid- and liquid-like behavior, thus creating a

challenge as to the simple classification as either solid or liquid [4]. These complex materials are known as viscoelastic materials.

In rheological measurements, a deformation is applied to the material in a controlled manner and the material's response is measured. The constitutive equation that relates stress to rate of strain was first introduced by Sir Isaac Newton in 1687 and is referred to as Newton's Law of Viscosity given by

$$\sigma = \mu\dot{\gamma} \qquad 5.1$$

where σ is the shear stress, μ the viscosity and $\dot{\gamma}$ the shear rate. For a Newtonian fluid, the viscosity is constant. However, complex fluids, such as polymer solutions, can exhibit a viscosity that is a function of applied shear rate. Complex fluids can be shear thinning or shear thickening and this behavior can be modeled by a power law equation

$$\sigma = \eta\dot{\gamma}^{n} \qquad 5.2$$

where σ is the shear stress, η the viscosity and $\dot{\gamma}$ the shear rate. For shear thinning materials, when $n < 1$, an applied stress will cause the viscosity to decrease, making the material flow easier. The opposite is true for a shear thickening material, where $n > 1$. With an applied shear stress, the viscosity increases. When $n = 1$, the fluid is Newtonian with a constant viscosity, and an applied shear stress results in a linear increase in the shear rate. Figure 5.1 illustrates the difference in these three types of materials.

Fluids such as polymer solutions and emulsions like toothpaste represent two common types of complex non-Newtonian fluids. Toothpaste is an example of a shear thinning material. While in the tube it does not flow and has solid-like behavior. However, squeezing the tube, and hence applying a shear force, causes the toothpaste to

flow like a liquid. The most oft used example of a shear thickening material is a mixture of cornstarch and water, an Oobleck mixture. This suspension of starch in water flows like a liquid when poured, but exhibits solid-like behavior when a force is applied.

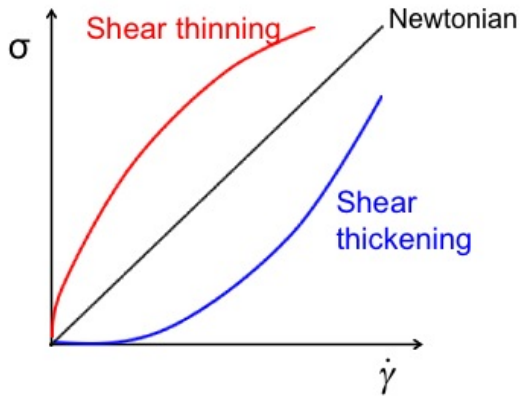

Figure 5.1. Power law fluids. Shear thinning and shear thickening fluids are complex fluids whose viscosity changes with the applied shear stress. Newtonian fluids have a constant viscosity.

Rheology measurements describe mechanical properties such as viscosity for the bulk fluid as a whole. These properties are then used to infer theories about what might be occurring at the molecular level. Rheologists often then look to other techniques such as x-ray scattering, neutron scattering and birefringence as a means of verifying the assumptions made about molecular configuration and orientation [126, 127]. Within the last two decades, however, rheo-NMR has emerged as a valid means of elucidating the link between the mechanical behavior and molecular structure [118, 126].

Rheo-NMR

Rheo-NMR combines rheology techniques with nuclear magnetic resonance, augmenting rheological data and enhancing knowledge of fluid properties under shear.

The first mention of using NMR methods to study the rheological properties of fluids was made in 1986, but was not demonstrated until approximately half a decade later in the early 1990s [126]. In contrast, rheology, the study of the deformation and flow of a fluid, has been in use since the early 1900s.

Combining the imaging and dynamic measurement techniques of NMR with the modalities of rheology allows for non-invasive study of the molecular properties of complex fluids while concurrently applying a shear. Rheo-NMR has been used to examine molecular properties of fluids under shear [119, 127], to elucidate the molecular ordering under high shear conditions [118, 120, 126-128], and to image the velocity fields of deformational flow [118, 119, 126, 128, 129].

Rheo-NMR has also recently been suggested as a method to monitor product quality control [122]. For example, in manufacturing, concentrated dispersions are often subjected to high shear processes like mixing and pumping. Rheo-NMR provides a method to non-invasively study the structure of these materials under stress and illuminate any structural changes that occur. These findings could impact the design of production plants, as well as the processes used to produce these materials [122].

In the food processing industry, as with the manufacturing industry, suspensions and emulsions like beer mashes [122] and cocoa butter [124] are processed through mixing, handling and pumping events. In the case of cocoa butter, the “fatty” substance used to make chocolate, important qualities like texture are dependent upon the shear forces applied during the manufacturing process [124]. Using rheo-NMR the quality of the cocoa butter can be correlated with the shear stress, allowing for improved

manufacturing process [122, 124]. Van As (2013) predicts an increase in the use of rheo-NMR in the food sciences, as it will become a more important tool in food processing techniques [123].

In the work presented here, the polymer polyacrylamide was chosen as a model for understanding the behavior of a non-Newtonian fluid under shear due to its wide use in many industries. The addition of nanoparticles to polymer solutions has recently become a focus of the polymer and petroleum industries. Understanding how the addition of the nanoparticles affects the properties of polyacrylamide is the direction of future work. The research presented here has laid the groundwork for that next step.

Methods and Materials

Rheology

An AR G2 rotational rheometer with a 60-mm diameter stainless steel cone-and-plate geometry was used to measure viscosity over a range of shear rates from 1 – 5000 s^{-1}.

Rheo-NMR

For each fluid analyzed the rheo-NMR equipment was assembled as described below and velocity images taken for multiple shear rates ranging from 10.7 s^{-1} to a maximum 186.9 s^{-1} for glycerol and 373.9 s^{-1} for polyacrylamide. All rates given in this thesis are average shear rates and determined by the following equation [118, 120]:

$$\dot{\gamma} = \frac{r_i \omega_i}{r_o - r_i} \qquad 5.3$$

where $\dot{\gamma}$ is the average shear rate, r_i and r_o are the inner and outer radii, respectively, and ω_i is the angular velocity of the rotating inner cylinder.

Rheo-NMR Couette Device

A concentric cylinder Couette device was used in the experiments performed in this chapter. Originally described by Maurice Couette [117], the system consists of two concentric cylinders where either one or both of the cylinders rotates and the fluid under study is contained in the annulus. For the experiments described here, only the inner cylinder could rotate. The fluids studied were glycerol and polyacrylamide. A schematic of the Rheo-NMR Couette is shown in Figure 5.2.

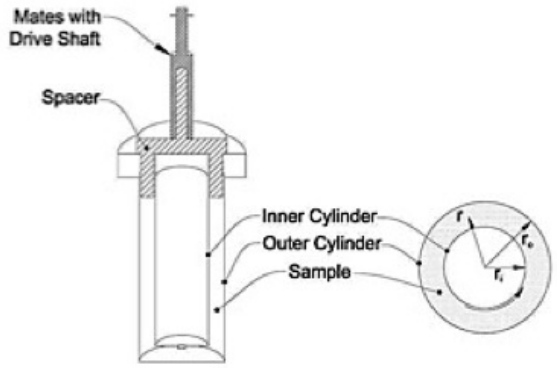

Figure 5.2. Couette system. The Couette device used in these experiments had a stationary outer cylinder and rotating inner cylinder. The fluid under study was contained in the annulus between the cylinders. On the top of the Couette device is a short coupling shaft that connects to a drive shaft (not shown), which spun the inner cylinder and was programmed by a Rheo-NMR Controller.

The inner radius of the Couette's outer cylinder was 9.5 mm, while the outer radius of the rotating inner cylinder was 8.5 mm, giving and annular dimension of 1mm. High shear rates are more readily attained for fluids confined to small gaps [126], which

is the condition in this Couette device. With only the inner cylinder rotating the shear forces applied to the fluid across the gap were at a maximum at the wall of the inner cylinder (Figure 5.3). A spacer in Figure 5.2 at the top of the cylinders was used to prevent the inner cylinder from wobbling while rotating.

The Couette device was tightly secured within a 25-mm radio frequency coil, which was fixed to the top of a Micro2.5 micro-imaging probe. The probe and Couette were positioned in the bore of a 300 MHz Bruker superconducting magnet connected to an AVANCE III spectrometer. The probe had the capacity to vary the gradients up to a maximum of 1.482 T m^{-1} in the three principle coordinate directions. Once the probe and

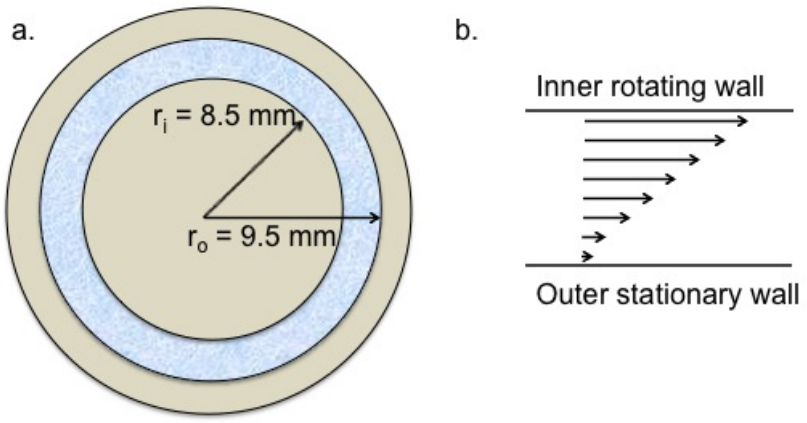

Figure 5.3. Couette device cross section and velocity profile. a.) Cross section of the Couette device with and inner radius of 8.5 mm and an outer radius of 9.5 mm. b.) Applied velocity profile across the annular space of the Couette.

Couette were secured in the magnet, a drive shaft was lowered into the magnet bore. The end of the drive shaft mated with the coupling shaft at the top of the Couette set up illustrated in Figure 5.2. Additionally, putty was inserted into the end of the drive shaft that mated with the coupler at the top of the Couette. This acted as a damping agent,

reducing vibrations transferred to the sample. After the drive shaft was lowered onto the Couette, a motor was attached to the top of the drive shaft. The motor, programmed by the Rheo-NMR Controller, spun the drive shaft, which in turn rotated the inner cylinder of the Couette device. Rotation frequencies were programmed into the Controller with a possible range of 0.1 Hz to 14 Hz.

Due to the non-Newtonian behavior of polyacrylamide at high shear, which could manifest as slip at the wall, the polymer solution was also used to fill the hollow inner cylinder of the Couette device as a marker fluid, since it is detectable with NMR. When the cylinder rotates, the fluid inside undergoes solid body rotation, allowing for extrapolation of the velocity to the surface of the inner cylinder where the fluid velocity was at a maximum. This serves as an *in situ* check of the applied rotation rate.

Sample Preparation

Three fluids were tested in these experiments. The first fluid, water, whose properties are very well understood, was chosen as a test fluid to ensure that the rheo-NMR equipment was set up properly and the experiments produced the expected results. Due to the low viscosity of water, vibrations in the rheo-NMR system were easily transmitted to the sample, resulting in unusable data. For this reason, no water data will be discussed. Glycerol was then chosen as the model Newtonian fluid due to its increased viscosity compared to that of water, and thus a reduced susceptibility to systemic vibrations. Polyacrylamide, or PAA, a well-studied fluid in rheology, is also an industrially important polymer, and was therefore selected as the non-Newtonian fluid.

Polyacrylyamide A 1 wt% polyacrylamide solution was prepared by mixing 1 gram of powdered polyacrylamide (Sigma Aldrich) with 100 mL of deionized water. The beaker was covered and allowed to mix at room temperature on a stir plate for five to seven days. After the polyacrylamide was adequately mixed, the relaxing agent Magnevist (Berlex Laboratories) was added to reduce the relaxation time of the solution.

Glycerol A 90 % by volume solution was prepared by mixing 90 mL of glycerol with 10 mL of deionized water. The solution was covered and mixed at room temperature on a stir plate for approximately 30 minutes.

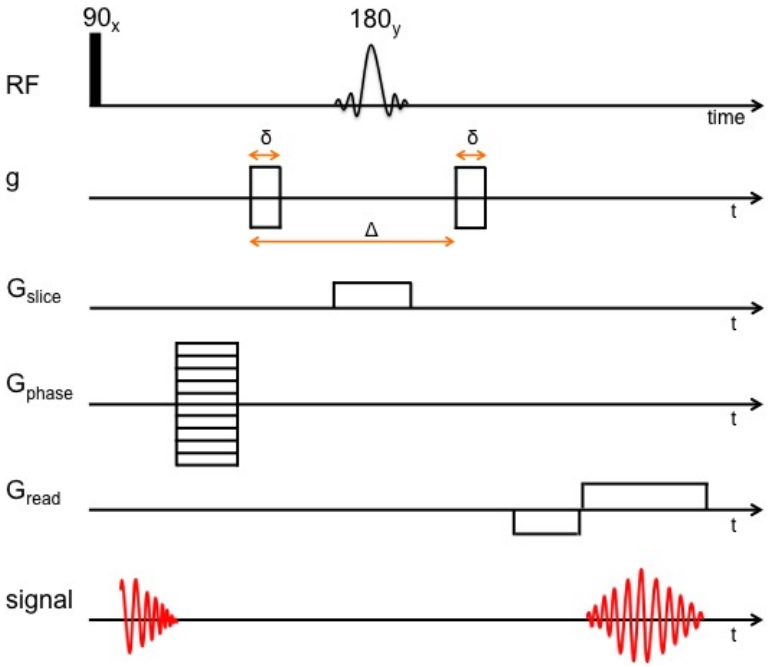

Figure 5.4. Velocity image pulse sequence. A hard 90_x pulse is used to excite all the spins in the sample before encoding for position and velocity. A soft 180_y pulse is used in conjunction with a gradient G_{slice} to selectively excite a slice of the sample for imaging. The imaging gradients (G_{phase}, and G_{read}) are applied such that k-space can be traversed while the propagator gradients (g) are applied to collect q-space velocity information. For the experiments discussed here, δ = 0.5 ms; Δ = 8 ms, g = -0.058 and 0.058 T m^{-1}.

Velocity Imaging

To obtain velocity images, velocity was encoded for using a PGSE sequence in conjunction with an imaging pulse sequence as discussed previously in Chapter 1. The resulting data was a three dimensional matrix collected in both *q*- and *k*-space. This pulse sequence was shown in Figure 1.20, but repeated here (Figure 5.4) for illustration purposes. Recall that G denotes the imaging gradients while the *q*-space gradient is given by *g* in Figure 5.4. Important parameters for these experiments are δ = 0.5 ms, Δ = 8 ms, and g = -0.058 and 0.058 T m^{-1}. The results from the experiments were Fourier transformed in both the *k* and *q* dimensions to attain a velocity image, an example of which is shown in Figure 5.5.

Results And Discussion

In Figure 5.5 a velocity image of glycerol in the Rheo-NMR Couette is shown for a shear rate of 53.4 s^{-1}. To obtain the velocity profiles for data analysis, a point was chosen in the center of the Couette, as shown by the white line in Figure 5.5a, and a velocity profile across the fluid gap extracted from the image. Maximum expected velocities from the applied rotation rates were calculated using the formula

$$v_{\max} = 2r_i\omega_i \qquad 5.4$$

where r_i is the radius of the inner cylinder and ω_i is the angular velocity of the inner cylinder.

Average shear rates of 10.7 s^{-1} to 373.9 s^{-1} were applied to the non-Newtonian 1wt% polyacrylamide solution. For comparison to a Newtonian fluid, glycerol was

studied for average shear rates of 10.7 s^{-1} up to 186.9 s^{-1}. Water was also examined, but due to vibration in the system at the shear rates discussed for glycerol and PAA, no water

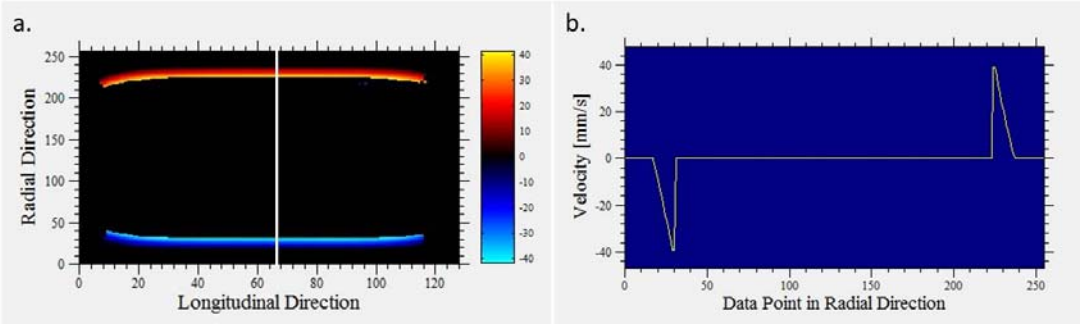

Figure 5.5. Velocity image and profile for glycerol at a shear rate of 53.4 s^{-1}. a.) Velocity image for glycerol at a shear rate of 53.4 s^{-1}. The inner cylinder is rotating such that the positive velocities (red, top of velocity image) correspond to the cylinder coming out of the page and the negative velocities (blue, bottom of velocity image) are going into the page. b.) Velocity profile take across the Couette device indicated by the white line in (a). Experiment details are as follows: T_R = 900 ms, 8 averages, field of view of 44 mm x 22 mm, 128 read points x 256 phase points, resolution of 344 μm x 86 μm $pixel^{-1}$, δ = 0.5 ms, Δ = 8 ms, g = -0.058 and 0.058 T m^{-1}.

data will be presented. Hydrodynamic instabilities, specifically Taylor vortices, were observed in the water sample at an average shear rate of 64.1 s^{-1}, but due to higher viscosities were not seen in the glycerol or polyacrylamide samples, even at average shear rates as high as 373 s^{-1} in the polyacrylamide.

The shear rates in the rheo-NMR velocity imaging experiments were chosen based on rheology data obtained for the 1wt% polyacrylamide shown in Figure 5.6, and the limits of the equipment used. PAA exhibits Newtonian plateaus as a constant viscosity at low shear rates near 1 s^{-1} and again at high shear rates greater than 1000 s^{-1}. Between these values, PAA shows shear thinning behavior. The lowest possible shear rate accessible with the rheo-NMR equipment used was 5.4 s^{-1}. However, that rotation

rate did not provide good data due to vibration. Therefore the minimum shear rate possible with reliable data was 10.7 s^{-1}. A maximum of 373 s^{-1} was applied, however this

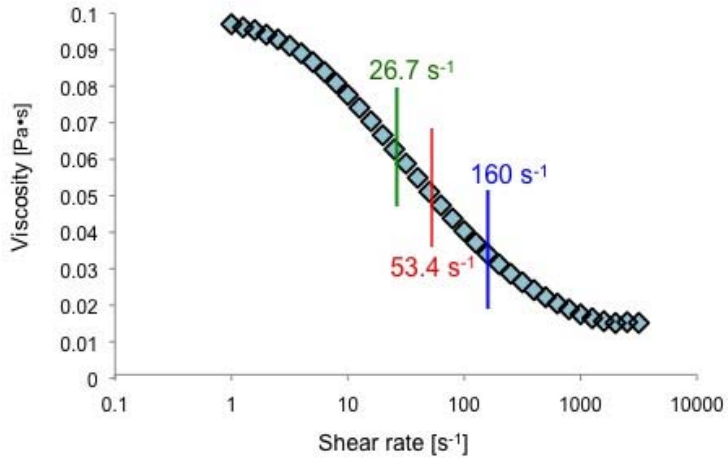

Figure 5.6. Viscosity as a function of shear rate for 1 wt% PAA in water. The colored lines on the plot indicate the shear rates examined in this work. This rheology data was collected by undergraduate Chelsie Wharton.

high rotation rate resulted in signal loss in the pixels nearest the inner rotating wall and a subsequent loss of data. The solid lines in Figure 5.6 indicate shear rates examined by Rheo-NMR and presented in this work.

Figure 5.7 shows polyacrylamide and glycerol at a shear rate of 26.7 s^{-1}, corresponding to a rotation rate of the inner cylinder of the Couette of 0.5 Hz. This shear rate is in the shear-thinning region of Figure 5.6. The velocity for both the glycerol and PAA were normalized to the maximum velocity of the glycerol, determined by extrapolation to the inner cylinder radius (8.5 mm). Glycerol showed characteristic Newtonian behavior, with a linear velocity gradient across the gap. Additionally, the maximum velocity determined by extrapolation (25.9 mm s^{-1}) matched well to the

expected maximum velocity of 26.7 mm s^{-1} calculated using equation 5.4. The PAA velocity gradient is slightly less linear, possibly due to shear thinning, but is mostly in

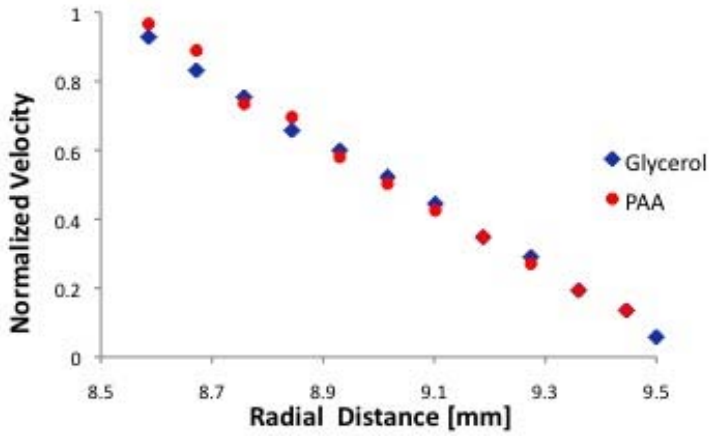

Figure 5.7. Normalized velocity profile for polyacrylamide and glycerol at a shear rate of 26.7 s^{-1}. The linear decrease in velocity for the glycerol across the gap was expected behavior as it is a Newtonian fluid. Polyacrylamide exhibited non-linear behavior near the inner rotating wall.

good agreement with glycerol. At this shear rate, there does not appear to be any slip at the wall in the PAA sample as the maximum velocity approaches the same maximum at the wall as the glycerol sample.

In Figure 5.8, polyacrylamide and glycerol are shown for a shear rate of 53.4 s^{-1} corresponding to a rotation frequency of 1 Hz. Again the glycerol shows a linearly decreasing velocity consistent with a Newtonian fluid. For the polyacrylamide velocity data, PAA was added to the inner cylinder as a marker fluid. The solid body rotation of this marker fluid allowed extrapolation of the actual velocity at the wall of the annulus. The PAA data shown in Figure 5.8 was normalized by this calculated maximum velocity. For this shear rate, polyacrylamide exhibits a non-linearly decreasing velocity profile.

With a small gap width of 1 mm, it was assumed that the shear rate across the gap was constant. However, in reality, the shear is highest at the inner rotating wall. As PAA is

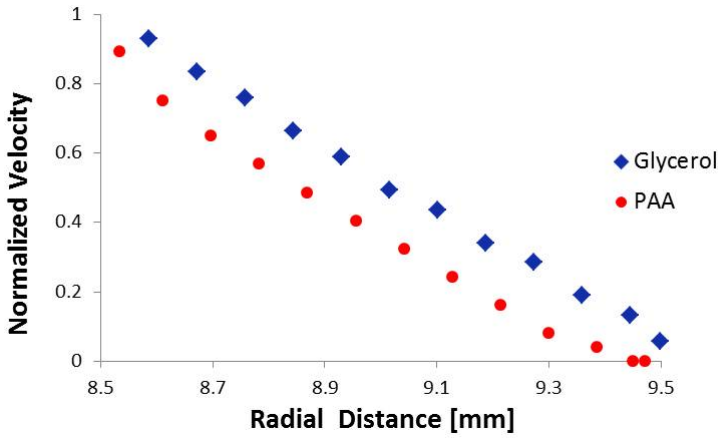

Figure 5.8. Normalized velocity profile for polyacrylamide and glycerol at a shear rate of 53.4 s^{-1}. Glycerol exhibits Newtonian behavior in the linear velocity profile across the gap. Polyacrylamide may be experiencing slip near the rotating wall as indicated by a reduced normalized velocity at that point.

shear thinning at this applied shear rate, the velocity gradient is largest near the rotating wall, giving the curved velocity profile.

Figure 5.9 shows velocity profiles for polyacrylamide at three shear rates of 26.7, 53.4 and 160 s^{-1}. At the highest shear rate of 160 s^{-1}in Figure 5.9, the velocity was normalized in the same manner described above using PAA as a marker fluid. Signal loss in the pixel nearest the wall precluded an accurate velocity measurement, so that point was omitted. This signal loss could be due to polymer alignment resulting in increased relaxation and will be explored in future work.

The normalized velocity distributions suggest that slip may be occurring at the rotating wall at the highest shear rate of Figure 5.9. Due to slip at the wall, the maximum

velocity of the polyacrylamide sample is less than the expected normalized maximum. The "no slip" boundary condition states that at a fluid-solid interface, the fluid will have zero velocity relative to the surface. The phenomenon of slip occurs when a fluid violates the "no slip" boundary condition and appears to move at a velocity that is different from that of the solid. Partial slip at the wall has been modeled for flowing polymer solutions [130] and for parallel-plate rheology experiments [131]. Other

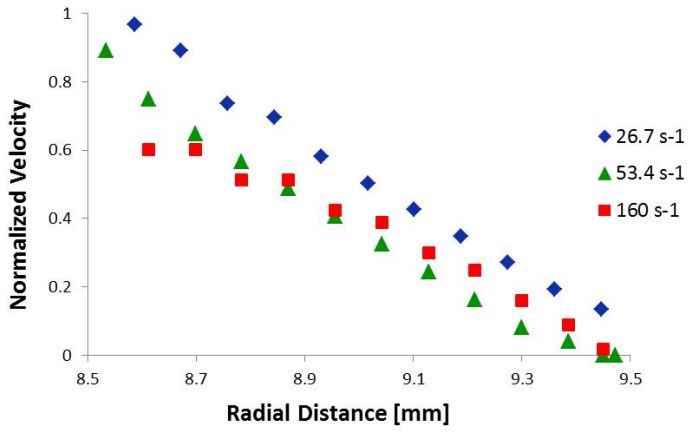

Figure 5.9. Polyacrylamide at three different shear rates 26.7, 53.4, 160 s^{-1}. Both 53.4 and 160 s^{-1} show shear thinning behavior near the wall with a steeper velocity gradient. Slip at the wall is possible at the highest shear rate.

experiments have shown that the onset of slip occurs at a certain critical shear stress at the wall [130]. Zhu [132] describes a possible scenario for slip where the rotating surface is wetted, providing a plane on which slip could occur. For the experiments here, a monolayer of fluid could have developed at the shearing wall, providing a "lubricated" surface on which the polyacrylamide could slide.

In addition, the intriguing non-linear behavior of the velocity profile at this rotation rate could be indicative of a slip-stick phenomenon, where slip at the rotating

wall is followed by reattachment of the polymer to the wall again. To verify that this is indeed what occurred, additional experiments should be performed, potentially using a Couette device with a roughened surface to prevent slip.

In the experiments presented in this chapter, Rheo-NMR successfully demonstrated that non-Newtonian behavior could be captured by velocity imaging. Newtonian behavior was exhibited by the glycerol solution, as was evident by the linear velocity profile across the annulus of the Couette device, as well as the maximum velocity at the shearing surface coinciding perfectly with the expected value. The polyacrylamide solution demonstrated non-Newtonian shear thinning behavior as well as violation of the "no slip" boundary condition at increased shear. Signal loss also occurred at the shearing surface for the higher shear rate in the polyacrylamide sample. Increasing the resolution of the data gathered in the radial direction could correct for some signal loss and better illustrate the degree of slip. If the read direction of the sample is programmed to be in the radial rather than the longitudinal direction, this greater resolution will not come at the cost of increased experiment time.

Future Work

An area of great interest in a multitude of industries is the interaction of particulates with polymers in solution. In wastewater treatment applications, this interaction could be used to produce flocculation. For enhanced oil recovery, small particulates present in the environment could interact with hydraulic fracturing fluids, such as polyacrylamide, reducing the overall efficiency of the recovery process.

Understanding how these nano-scale particles influence the structure and interactions of polymer in solution is important for many other applications as well. The pharmaceutical industry relies on polymer-particle interactions in high shear conditions for targeted drug delivery [22]. In the biomedical industry, time-released delivery of medication embedded in a polymer for a high shear application has the potential to save lives [20].

Polymers used as flocculation and stabilization agents interact with micro- and nano-scale particles through different mechanisms. In the case of flocculation (Figure 5.10a.), the radius of the particulate matter is smaller than the characteristic length of the polymer. The polymer chains adhere to the paticulate matter and begin to coalesce

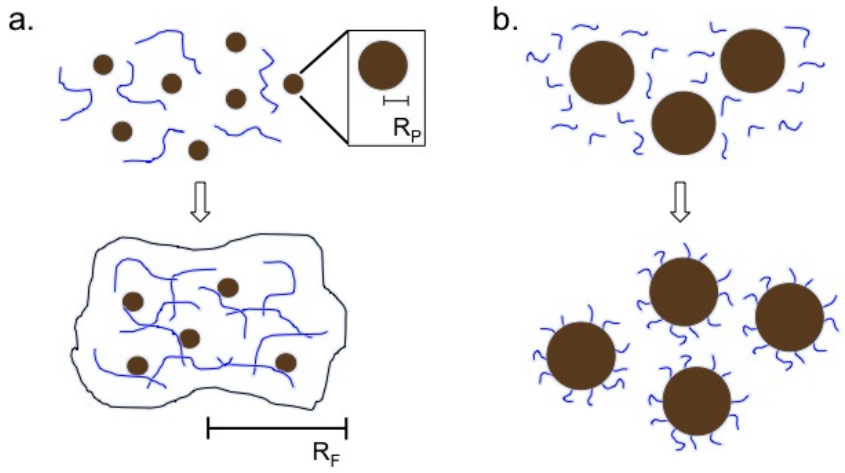

Figure 5.10. Polymer-particle interactions. a.) In flocculation, the characteristic length of the polymer is larger than the radius of the particle, R_P. The polymer adheres to the surface of the particle, forming flocs, which have a much larger radius (R_F) than the particulates. b.) For stabilization, the radius of the particle is now greater than the characteristic length of the polymer, therefore multiple polymer chains can bind to the surface of the particle. This creates a charged surface where the particles repel each other, preventing them from coalescing and thus stabilizing the suspension.

forming considerably larger particles called flocs. As a stabilizing agent (Figure 5.10b.), the polymer again adheres to the surface of the particle. However, in this instance the

characteristic length of the polymer is considerably smaller than the radius of the particulate matter. Multiple polymer chains are then able to bind to the particle surface and create a charged shell around the particle. The charged particles repel each other, preventing them from coalescing and thus stabilizing the suspension.

The introduction of nanoparticles into a polymer solution can change the behavior of the fluid under shearing conditions. For example, when silicon dioxide (SiO_2) nanoparticles (d = 10 – 20 nm) were added to a solution of 1wt% polyacrylamide, the

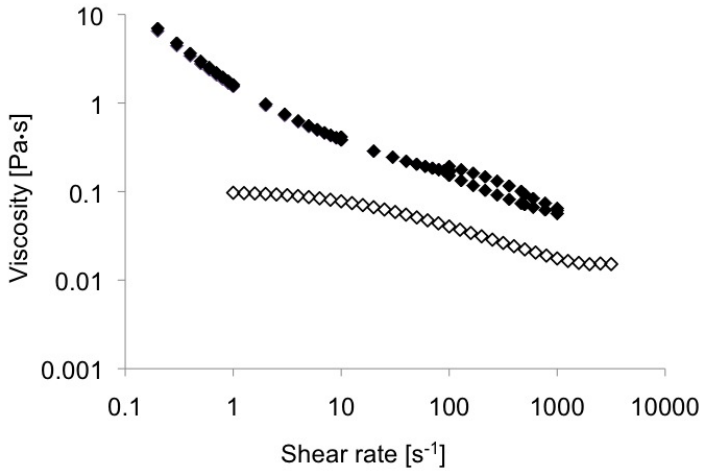

Figure 5.11. Viscosity as a function of shear rate for 1 wt% PAA in water (open diamonds) and 1 wt% PAA in water with 1 wt% SiO_2 nanoparticles (solid diamonds). The polyacrylamide responds to an applied shear stress differently with the addition of the nanoparticles. This rheology data was collected by undergraduate Chelsie Wharton

rheological behavior of the fluid changed, as shown in Figure 5.11. A shear thinning behavior is present over the entire range of shear rates, in contrast to the 1wt% PAA solution without the nanoparticles (open diamonds in Figure 5.11). Additionally, the polymer-particle dispersion (solid diamonds in Figure 5.11) shows a hysteresis effect at higher shear rates. In other words, at shear rates above approximately 100 s^{-1} the

viscosity of the polyacrylamide-nanoparticle dispersion is dependent upon the shear history of the sample.

The data presented in this chapter is preliminary work on polyacrylamide solutions, while future work will focus on elucidating the origins of the rheological behavior of the polymer-particle dispersion. Initially, additional experiments with 1wt% PAA at lower and higher shear rates should be conducted to improve upon preliminary results and further corroborate the rheological data shown in Figures 5.6 and 5.11. First, glycerol or some other viscous Newtonian fluid should always be used as a marker fluid when collecting Rheo-NMR velocity images. This would not only provide data for the maximum velocity at the rotating wall, but would also definitively indicate whether slip was occurring at the shearing surface. To attempt to prevent slip in future experiments, a Couette device with a rougher inner cylinder should be employed. More data points should also be collected across the fluid gap in all experiments. As mentioned earlier, if the read gradient is set such that the read orientation is in the radial direction also across the gap, then increasing the number of points will not subsequently increase the experiment time. As a result, the number of averages taken for each experiment could then be increased while maintaining the same experiment time. This would improve the signal to noise ratio and potentially prevent loss of signal in the pixel closest to the inner rotating wall, as was observed for PAA at 160 s^{-1} (Figure 5.9). In addition, this signal loss indicates that an understanding of the alignment of the polymer molecules under the different shear conditions should be considered. For this, the PAA solution should be mixed with deuterated water (D_2O) and experiments repeated monitoring the ^2H nucleus

spectrum as a function of position. Splitting of the ^{2}H peak is indicative of molecular ordering [126]. Once all issues have been resolved for polyacrylamide, future work will then focus on Rheo-NMR velocity imaging of the polyacrylamide-nanoparticle dispersion in order to explain the phenomenon revealed at the high shear rates in the rheology data of Figure 5.11 (solid diamonds).

Since the rheological data in Figure 5.11 exhibits shear-thinning behavior for both polyacrylamide and the polyacrylamide-nanoparticle dispersion, the velocity profiles can be fit with a power law model. For the shear force across the fluid in the annulus, the differential equation is given by [133]

$$\tau_{r,\theta} = -\eta r \frac{d}{dr}\left(\frac{v_\theta}{r}\right) \qquad 5.5$$

where $\tau_{r,\theta}$ is the shear stress in the rotating (θ) direction acting on a unit area perpendicular to the radial r direction; η is the shear-rate dependent viscosity; and v_θ is the velocity in the direction of the rotating inner cylinder. Substituting in the power law model (equation 5.2) and solving for the velocity profile gives

$$v_\Theta = v_{\max} \frac{r}{\kappa R}\left(\frac{1}{R^2}\right)^{\frac{1}{n}} \left(\frac{1-\left(\frac{R^2}{r^2}\right)^{\frac{1}{n}}}{1-\left(\frac{1}{\kappa^2}\right)^{\frac{1}{n}}} \right) \qquad 5.6$$

where the inner cylinder radius is given by κR, the outer radius by R and the power n. The parameter n can be adjusted to fit each individual velocity profile for comparison to the values obtained from fitting the same model to the rheological data.

The planned Rheo-NMR velocity imaging experiments, in combination with rheological characterization, have the potential to lend insight into polymer-particle interactions and their impact on fluid properties, important in fields ranging from enhanced oil recovery to the biomedical industry.

REFERENCES

1. Levitt, M.H., *Spin dynamics: Basics of nuclear magnetic resonance - 2nd Edition*2008, West Sussex: Wiley and Sons Ltd.

2. Callaghan, P.T., *Principles of Nuclear Magnetic Resonance Microscopy*1991, New York: Oxford University Press.

3. Serway, R.A., *Physics for Scientists and Engineers*1990, Philadelphia, PA: Saunders College Publishing.

4. Callaghan, P.T., *Translational Dynamics & Magnetic Resonance: Principles of Pulsed Gradient Spin Echo NMR*2011, New York: Oxford University Press.

5. Hayt, W.H. and J.A. Buck, *Engineering Electromagnetics*2001: McGraw-Hill Education.

6. Hahn, E.L., *Spin echoes.* Physical Review, 1950. **80**(4): p. 580-594.

7. Tanner, J.E., *Use of stimulated echo in NMR-diffusion studies.* Journal of Chemical Physics, 1970. **52**(5): p. 2523-2526.

8. Moratal, D., et al., *k-Space tutorial: an MRI educational tool for a better understanding of k-space.* Biomedical imaging and intervention journal, 2008. **4**(1): p. e15.

9. Carr, H.Y. and E.M. Purcell, *Effects of diffusion on free precession in nuclear magnetic resonance experiments.* Physical Review, 1954. **94**(3): p. 630-638.

10. Meiboom, S. and D. Gill, *Modified spin-echo method for measuring nuclear relaxtion times.* Review of Scientific Instruments, 1958. **29**(8): p. 688-691.

11. Hagmann, P., et al., *Understanding diffusion MR imaging techniques: From scalar diffusion-weighted imaging to diffusion tensor imaging and beyond.* Radiographics, 2006. **26**: p. S205-U219.

12. Stejskal, E.O. and J.E. Tanner, *Spin diffusion measurements: Spin echoes in the presence of a time-dependent field gradient.* Journal of Chemical Physics, 1965. **42**(1): p. 288-292.

13. Ragauskas, A.J., et al., *The path forward for biofuels and biomaterials.* Science, 2006. **311**(5760): p. 484-489.

14. Smidsrod, O. and G. Skjakbraek, *Alginate as immobilization matrix for cells.* Trends in Biotechnology, 1990. **8**(3): p. 71-78.

15. Turquois, T. and H. Gloria, *Determination of the absolute molecular weight averages and molecular weight distributions of alginates used as ice cream stabilizers by using multiangle laser light scattering measurements.* Journal of Agricultural and Food Chemistry, 2000. **48**(11): p. 5455-5458.

16. Regand, A. and H.D. Goff, *Structure and ice recrystallization in frozen stabilized ice cream model systems.* Food Hydrocolloids, 2003. **17**(1): p. 95-102.

17. Cha, D.S. and M.S. Chinnan, *Biopolymer-based antimicrobial packaging: A review.* Critical Reviews in Food Science and Nutrition, 2004. **44**(4): p. 223-237.

18. Odunsi, S.T., et al., *Effect of alginate on satiation, appetite, gastric function, and selected gut satiety hormones in overweight and obesity.* Obesity, 2010. **18**(8): p. 1579-1584.

19. Langer, R. and J.P. Vacanti, *Tissue engineering.* Science, 1993. **260**(5110): p. 920-926.

20. Stone, G.W., et al., *A polymer-based, paclitaxel-eluting stent in patients with coronary artery disease.* New England Journal of Medicine, 2004. **350**(3): p. 221-231.

21. Gao, X.H., et al., *In vivo cancer targeting and imaging with semiconductor quantum dots.* Nature Biotechnology, 2004. **22**(8): p. 969-976.

22. Duncan, R., *The dawning era of polymer therapeutics.* Nature Reviews Drug Discovery, 2003. **2**(5): p. 347-360.

23. Hutmacher, D.W., *Scaffolds in tissue engineering bone and cartilage.* Biomaterials, 2000. **21**(24): p. 2529-2543.

24. Davis, T.A., B. Volesky, and A. Mucci, *A review of the biochemistry of heavy metal biosorption by brown algae.* Water Research, 2003. **37**(18): p. 4311-4330.

25. Kovalenko, I., et al., *A major constituent of brown algae for use in high-capacity Li-ion batteries.* Science, 2011. **334**(6052): p. 75-79.

26. George, M. and T.E. Abraham, *Polyionic hydrocolloids for the intestinal delivery of protein drugs: Alginate and chitosan - A review.* Journal of Controlled Release, 2006. **114**(1): p. 1-14.

27. Cassidy, M.B., H. Lee, and J.T. Trevors, *Environmental applications of immobilized microbial cells: A review.* Journal of Industrial Microbiology, 1996. **16**(2): p. 79-101.

28. Donlan, R.M., *Biofilms: Microbial life on surfaces.* Emerging Infectious Diseases, 2002. **8**(9): p. 881-890.

29. Costerton, J.W., *Overview of microbial biofilms.* Journal of Industrial Microbiology, 1995. **15**(3): p. 137-140.

30. Costerton, J.W., *Introduction to biofilm.* International Journal of Antimicrobial Agents, 1999. **11**(3-4): p. 217-221.

31. Codd, S.L., et al., *NMR relaxation measurements of biofouling in model and geological porous media.* Organic Geochemistry, 2011. **42**(8): p. 965-971.

32. Halls, J.J.M., et al., *Efficient photodiodes from interpenetrating polymer networks.* Nature, 1995. **376**(6540): p. 498-500.

33. Brabec, C.J., N.S. Sariciftci, and J.C. Hummelen, *Plastic solar cells.* Advanced Functional Materials, 2001. **11**(1): p. 15-26.

34. Arico, A.S., et al., *Nanostructured materials for advanced energy conversion and storage devices.* Nature Materials, 2005. **4**(5): p. 366-377.

35. Brunsveld, L., et al., *Supramolecular polymers.* Chemical Reviews, 2001. **101**(12): p. 4071-4097.

36. De Greef, T.F.A., et al., *Supramolecular polymerization.* Chemical Reviews, 2009. **109**(11): p. 5687-5754.

37. Reddy, C.S.K., et al., *Polyhydroxyalkanoates: An overview.* Bioresource Technology, 2003. **87**(2): p. 137-146.

38. Reddy, M.V. and S.V. Mohan, *Effect of substrate load and nutrients concentration on the polyhydroxyalkanoates (PHA) production using mixed consortia through wastewater treatment.* Bioresource Technology, 2012. **114**: p. 573-582.

39. Kulkarni, R.K., et al., *Polylactic acid for surgical implants.* Archives of Surgery, 1966. **93**(5): p. 839-843.

40. Cutright, D.E. and E.E. Hunsuck, *Tissue reaction to biodegradable polylactic acid suture.* Oral Surgery Oral Medicine Oral Pathology Oral Radiology and Endodontics, 1971. **31**(1): p. 134-139.

41. Bajpai, P.K., I. Singh, and J. Madaan, *Comparative studies of mechanical and morphological properties of polylactic acid and polypropylene based natural fiber composites.* Journal of Reinforced Plastics and Composites, 2012. **31**(24): p. 1712-1724.

42. Chen, B.K., et al., *Ductile polylactic acid prepared with ionic liquids.* Chemical Engineering Journal, 2013. **215**: p. 886-893.

43. Higgins, L., et al., *Split-thickness skin graft donor site management: A randomized controlled trial comparing polyurethane with calcium alginate dressings.* International Wound Journal, 2012. **9**(2): p. 126-131.

44. Kaiser, D., et al., *Alginate dressing and polyurethane film versus paraffin gauze in the treatment of split-thickness skin graft donor sites: A randomized controlled pilot study.* Advances in Skin & Wound Care, 2013. **26**(2): p. 67-73.

45. Bolto, B. and J. Gregory, *Organic polyelectrolytes in water treatment.* Water Research, 2007. **41**(11): p. 2301-2324.

46. Siyam, T., *Development of acrylamide polymers for the treatment of waste water.* Designed Monomers and Polymers, 2001. **4**(2): p. 107-168.

47. Gregory, J. and S. Barany, *Adsorption and flocculation by polymers and polymer mixtures.* Advances in Colloid and Interface Science, 2011. **169**(1): p. 1-12.

48. A., C. and D. Rodbard, *Polyacrylamide gel electrophoresis.* Science, 1971. **172**(3982): p. 440-451.

49. Vos, P., et al., *AFLP - a new technique for DNA-fingerprinting.* Nucleic Acids Research, 1995. **23**(21): p. 4407-4414.

50. Ofarrell, P.H., *High-resolution 2-dimensional electrophoresis of proteins.* Journal of Biological Chemistry, 1975. **250**(10): p. 4007-4021.

51. Schagger, H. and G. Vonjagow, *Tricine sodium dodecyl-sulfate polyacrylamide-gel electrophoresis for the separation of proteins in the range from 1-kDa to 100-kDa.* Analytical Biochemistry, 1987. **166**(2): p. 368-379.

52. Sauer, K., et al., *Pseudomonas aeruginosa displays multiple phenotypes during development as a biofilm.* Journal of Bacteriology, 2002. **184**(4): p. 1140-1154.

53. Liber, K., L. Weber, and C. Levesque, *Sublethal toxicity of two wastewater treatment polymers to lake trout fry (Salvelinus namaycush).* Chemosphere, 2005. **61**(8): p. 1123-1133.

54. Wong, S.S., et al., *Treatment of pulp and paper mill wastewater by polyacrylamide (PAM) in polymer induced flocculation.* Journal of Hazardous Materials, 2006. **135**(1-3): p. 378-388.

55. Moody, G., *The use of polyacrylamides in mineral processing.* Minerals Engineering, 1992. **5**(3-5): p. 479-492.

56. Taylor, K.C. and H.A. Nasreldin, *Acrylamide copolymers - A review of methods for the determination of concentration and degree of hydrolysis.* Journal of Petroleum Science and Engineering, 1994. **12**(1): p. 9-23.

57. Audibert, A. and J. Lecourtier, *Stability of water-soluble polymers in the presence of corrodible materials.* Polymer Degradation and Stability, 1993. **40**(2): p. 151-165.

58. Audibert-Hayet, A. and C. Dalmazzone, *Surfactant system for water-based well fluids.* Colloids and Surfaces a-Physicochemical and Engineering Aspects, 2006. **288**(1-3): p. 113-120.

59. Philippova, O.E. and A.R. Khokhlov, *Smart polymers for oil production.* Petroleum Chemistry, 2010. **50**(4): p. 266-270.

60. Wever, D.A.Z., F. Picchioni, and A.A. Broekhuis, *Polymers for enhanced oil recovery: A paradigm for structure-property relationship in aqueous solution.* Progress in Polymer Science, 2011. **36**(11): p. 1558-1628.

61. Lentz, R.D., et al., *Polyacrylamide for surface irrigation to increase nutrient-use efficiency and protect water quality.* Communications in Soil Science and Plant Analysis, 2001. **32**(7-8): p. 1203-1220.

62. Figueira, M.M., et al., *Biosorption of metals in brown seaweed biomass.* Water Research, 2000. **34**(1): p. 196-204.

63. Rathore, S., et al., *Microencapsulation of microbial cells.* Journal of Food Engineering, 2013. **116**(2): p. 369-381.

64. Bashan, Y., *Inoculants of plant growth-promoting bacteria for use in agriculture.* Biotechnology Advances, 1998. **16**(4): p. 729-770.

65. Kuo, C.K. and P.X. Ma, *Ionically crosslinked alginate hydrogels as scaffolds for tissue engineering: Part 1. Structure, gelation rate and mechanical properties.* Biomaterials, 2001. **22**(6): p. 511-521.

66. Drury, J.L. and D.J. Mooney, *Hydrogels for tissue engineering: Scaffold design variables and applications.* Biomaterials, 2003. **24**(24): p. 4337-4351.

67. Leor, J., et al., *Bioengineered cardiac grafts - A new approach to repair the infarcted myocardium?* Circulation, 2000. **102**(19): p. 56-61.

68. Sutherland, I.W., *Biofilm exopolysaccharides: A strong and sticky framework.* Microbiology-Uk, 2001. **147**: p. 3-9.

69. Donlan, R.M. and J.W. Costerton, *Biofilms: Survival mechanisms of clinically relevant microorganisms.* Clinical Microbiology Reviews, 2002. **15**(2): p. 167-193.

70. Fux, C.A., et al., *The Functional Resistance of Bacterial Biofilms*. Antimicrobial Drug Resistance, Vol 1: Mechanisms of Drug Resistance, ed. D.L. Mayers2009: Humana Press Inc, 999 Riverview Dr, Ste 208, Totowa, Nj 07512-1165 USA. 121-131.

71. Fux, C.A., et al., *Survival strategies of infectious biofilms.* Trends in Microbiology, 2005. **13**(1): p. 34-40.

72. Watnick, P. and R. Kolter, *Biofilm, city of microbes.* Journal of Bacteriology, 2000. **182**(10): p. 2675-2679.

73. O'Toole, G., H.B. Kaplan, and R. Kolter, *Biofilm formation as microbial development.* Annual Review of Microbiology, 2000. **54**: p. 49-79.

74. Costerton, J.W., et al., *Bacterial biofilms: A diagnostic and therapeutic challenge.* Expert Review of Anti-infective Therapy, 2003. **1**(4): p. 667-683.

75. Stoodley, P., et al., *Evolving perspectives of biofilm structure.* Biofouling, 1999. **14**(1): p. 75-90.

76. Debeer, D., P. Stoodley, and Z. Lewandowski, *Liquid flow in heterogeneous biofilms.* Biotechnology and Bioengineering, 1994. **44**(5): p. 636-641.

77. Klapper, I. and J. Dockery, *Mathematical description of microbial biofilms.* Siam Review, 2010. **52**(2): p. 221-265.

78. Williams, P., et al., *Look who's talking: communication and quorum sensing in the bacterial world.* Philosophical Transactions of the Royal Society B-Biological Sciences, 2007. **362**(1483): p. 1119-1134.

79. Klapper, I., et al., *Viscoelastic fluid description of bacterial biofilm material properties.* Biotechnology and Bioengineering, 2002. **80**(3): p. 289-296.

80. Pintelon, T.R.R., et al., *The effect of biofilm permeability on bio-clogging of porous media.* Biotechnology and Bioengineering, 2012. **109**(4): p. 1031-1042.

81. Hornemann, J.A., et al., *Biopolymer and water dynamics in microbial biofilm extracellular polymeric substance.* Biomacromolecules, 2008. **9**(9): p. 2322-2328.

82. Manz, B., et al., *Measuring local flow velocities and biofilm structure in biofilm systems with magnetic resonance imaging (MRI).* Biotechnology and Bioengineering, 2003. **84**(4): p. 424-432.

83. Seymour, J.D., et al., *Magnetic resonance microscopy of biofilm structure and impact on transport in a capillary bioreactor.* Journal of Magnetic Resonance, 2004. **167**(2): p. 322-327.

84. Seymour, J.D., et al., *Anomalous fluid transport in porous media induced by biofilm growth.* Physical Review Letters, 2004. **93**(19): p. 198103.

85. Fridjonsson, E.O., et al., *NMR measurement of hydrodynamic dispersion in porous media subject to biofilm mediated precipitation reactions.* Journal of Contaminant Hydrology, 2011. **120-21**: p. 79-88.

86. Gjersing, E.L., et al., *Magnetic resonance microscopy analysis of advective transport in a biofilm reactor.* Biotechnology and Bioengineering, 2005. **89**(7): p. 822-834.

87. Hornemann, J.A., et al., *Secondary flow mixing due to biofilm growth in capillaries of varying dimensions.* Biotechnology and Bioengineering, 2009. **103**(2): p. 353-360.

88. Carver, J.P. and R.E. Richards, *General 2-site solution for chemical exchange produced dependence of T2 upon Carr-Purcell pulse separation.* Journal of Magnetic Resonance, 1972. **6**(1): p. 89-105.

89. Mitchell, A.C., et al., *Resilience of planktonic and biofilm cultures to supercritical CO2.* Journal of Supercritical Fluids, 2008. **47**(2): p. 318-325.

90. Stewart, P.S., *Mini-review: Convection around biofilms.* Biofouling, 2012. **28**(2): p. 187-198.

91. Beveridge, T.J., et al., *Interactions between biofilms and the environment.* Fems Microbiology Reviews, 1997. **20**(3-4): p. 291-303.

92. Bouwer, E.J., et al., *Biofilms in Porous Media*, in *Biofilms II: Process Analysis and Applications*, J.D. Bryers, Editor 2000, Wiley-Liss, Inc. p. 123-158.

93. Cunningham, A.B., et al., *Subsurface biofilm barriers for the containment and remediation of contaminated groundwater.* Bioremediat J, 2003. **7**(3): p. 151-164.

94. Fang, Y.L., et al., *Multicomponent reactive transport modeling of uranium bioremediation field experiments.* Geochimica Et Cosmochimica Acta, 2009. **73**(20): p. 6029-6051.

95. Lomesh, D., et al., *In situ biofilm barriers: Case study of a nitrate groundwater plume, Albuquerque, New Mexico.* Remediat J, 2005. **15**(4): p. 101-111.

96. Stoodley, P., D. Debeer, and Z. Lewandowski, *Liquid flow in biofilm systems.* Applied and Environmental Microbiology, 1994. **60**(8): p. 2711-2716.

97. Sharp, R.R., et al., *Visualization and characterization of dynamic patterns of flow, growth and activity of biofilms growing in porous media.* Water Science and Technology, 2005. **52**(7): p. 85-90.

98. Atekwana, E.A., *Geophysical signatures of microbial activity at hydrocarbon contaminated sites: A review.* Surveys in Geophysics, 2010. **31**(2): p. 247-283.

99. Lewandowski, Z., P. Stoodley, and S. Altobelli, *Experimental and conceptual studies on mass-transport in biofilms.* Water Science and Technology, 1995. **31**(1): p. 153-162.

100. Hoskins, B.C., et al., *Selective imaging of biofilms in porous media by NMR relaxation.* Journal of Magnetic Resonance, 1999. **139**: p. 67-73.

101. Beauregard, D.A., et al., *Using non-invasive magnetic resonance imaging (MRI) to assess the reduction of Cr(VI) using a biofilm-palladium catalyst.* Biotechnology and Bioengineering, 2010. **107**(1): p. 11-20.

102. Paterson-Beedle, M., et al., *Study of biofilm within a packed-bed reactor by three-dimensional magnetic resonance imaging*, in *Methods in Ezymology*2001. p. 285-305.

103. von der Schulenburg, D.A.G., et al., *Non-invasive mass transfer measurements in complex biofilm-coated structures.* Biotechnology and Bioengineering, 2008. **101**(3): p. 602-608.

104. Keating, K. and R. Knight, *A laboratory study to determine the effect of iron oxides on proton NMR measurements.* Geophysics, 2007. **72**(1): p. E27-E32.

105. Nivens, D.E., et al., *Role of alginate and its O acetylation in formation of Pseudomonas aeruginosa microcolonies and biofilms.* Journal of Bacteriology, 2001. **183**(3): p. 1047-1057.

106. Characklis, W.G. and I.B. James D Bryers, *Bioengineering report. Fouling biofilm development: A process analysis. Biotechnol Bioeng., Vol. XXIII, Pp. 1923-60 (1981).* Biotechnology and Bioengineering, 2009. **102**(2): p. 309, 310-47.

107. Lovley, D.R., et al., *Microbial reduction of uranium.* Nature, 1991. **350**(6317): p. 413-416.

108. Banat, I.M., *Biosurfactants production and possible uses in microbial enhanced oil recovery and oil pollution remediation: A review.* Bioresource Technology, 1995. **51**(1): p. 1-12.

109. Venkataramanan, L., Y.Q. Song, and M.D. Hurlimann, *Solving Fredholm integrals of the first kind with tensor product structure in 2 and 2.5 dimensions.* Ieee Transactions on Signal Processing, 2002. **50**(5): p. 1017-1026.

110. Hills, B.P., K.M. Wright, and P.S. Belton, *Proton NMR-studies of chemical and diffusive exchange in carbohydrate systems.* Molecular Physics, 1989. **67**(6): p. 1309-1326.

111. Walsh, D.O., et al. *Javelin: a slimhole and microhole NMR logging tool*. FastTimes, 2010. **15**, 67-72.

112. Franklin, M.J., et al., *Biosynthesis of the Pseudomonas aeruginosa extracellular polysaccarides, alginate, Pel, and Psl.* Frontiers in Microbiology, 2011. **2**(167): p. 167-1-16.

113. Grant, G.T., et al., *Biological Interactions between polysaccharides and divalent cations - Egg-box model.* Febs Letters, 1973. **32**(1): p. 195-198.

114. Borchard, W., et al., *Phase diagram of the system sodium alginate/water: A model for biofilms.* International Journal of Biological Macromolecules, 2005. **35**(5): p. 247-256.

115. Hills, B.P., C. Cano, and P.S. Belton, *Proton NMR relaxation studies of aqueous polysaccharide systems.* Macromolecules, 1991. **24**(10): p. 2944-2950.

116. Motyka, A.L., *An introduction to rheology with an emphasis on application to dispersions.* Journal of Chemical Education, 1996. **73**(4): p. 374-380.

117. Broadbent, A.L., et al., *Pulsed gradient spin echo nuclear magnetic resonance measurement and simulation of two-fluid Taylor vortex flow in a vertically oriented Taylor-Couette device.* Applied Magnetic Resonance, 2012. **42**(1): p. 137-152.

118. Douglass, B.S., et al., *Rheo-NMR of wormlike micelles formed from nonionic pluronic surfactants.* Macromolecules, 2008. **41**(3): p. 804-814.

119. Callaghan, P.T. and A.M. Gil, *Rheo-NMR of semidilute polyacrylamide in water.* Macromolecules, 2000. **33**(11): p. 4116-4124.

120. Medronho, B., et al., *Planar lamellae and onions: a spatially resolved rheo-NMR approach to the shear-induced structural transformations in a surfactant model system.* Soft Matter, 2011. **7**(10): p. 4938-4947.

121. Fardin, M.A., et al., *Shear-banding in surfactant wormlike micelles: Elastic instabilities and wall slip.* Soft Matter, 2012. **8**(8): p. 2535-2553.

122. Götz, J. and K. Zick, *Rheo-NMR: Applications to Food*, in *Modern Magnetic Resonance*, G. Webb, Editor 2006, Springer Netherlands. p. 1819-1824.

123. Van As, H. and J. van Duynhoven, *MRI of plants and foods.* Journal of Magnetic Resonance, 2013. **229**: p. 25-34.

124. Mudge, E.M. and G. Mazzanti, *Rheo-NMR measurements of cocoa butter crystallized under shear flow.* Crystal Growth & Design, 2009. **9**(7): p. 3111-3118.

125. Marangoni, A.G., et al., *Structure and functionality of edible fats.* Soft Matter, 2012. **8**(5): p. 1275-1300.

126. Callaghan, P.T., *Rheo-NMR: nuclear magnetic resonance and the rheology of complex fluids.* Reports on Progress in Physics, 1999. **62**(4): p. 599-670.

127. Badiger, M.V., et al., *In situ rheo-NMR investigations of shear-dependent H-1 spin relaxation in polymer solutions.* Macromolecules, 2002. **35**(1): p. 126-134.

128. Callaghan, P.T., *Rheo NMR and shear banding.* Rheologica Acta, 2008. **47**(3): p. 243-255.

129. Callaghan, P.T., *Rheo-NMR and velocity imaging.* Current Opinion in Colloid & Interface Science, 2006. **11**(1): p. 13-18.

130. Tanner, R.I., *Parital wall slip in polymer flow.* Industrial & Engineering Chemistry Research, 1994. **33**(10): p. 2434-2436.

131. Laun, H.M., M. Rady, and O. Hassager, *Analytical solutions for squeeze flow with partial wall slip.* Journal of Non-Newtonian Fluid Mechanics, 1999. **81**(1–2): p. 1-15.

132. Zhu, Y.X. and S. Granick, *No-slip boundary condition switches to partial slip when fluid contains surfactant.* Langmuir, 2002. **18**(26): p. 10058-10063.

133. Bird, R.B., W.E. Stewart, and E.N. Lightfoot, *Transport Phenomena*2002, New York: Wiley.